High frequency magneto-acoustics in diluted magnetic semiconductors

Dissertation

Presented to the Faculty of Physics of the Technische Universität Dortmund, Germany, in partial fulfillment of the requirements for the degree of

Doktor rer. nat.

by

Michael Bombeck

technische universität dortmund

Dortmund, December 2014

Accepted by the Faculty of Physics of the TU Dortmund University, Germany.

Day of oral exam: 12th December 2014

Examination board:

Prof. Dr. Manfred Bayer

Prof. Dr. Metin Tolan

Prof. Dr. Jan Kierfeld

Dr. Michael Paulus

Table of contents

Table of contents i

1. Motivation 1

2. Introduction 5

2.1. From sound to hypersound 5
2.2. The diluted magnetic semiconductor (Ga,Mn)As 19

3. Experimental techniques and setup 29

3.1. Experimental setup 29
3.2. Optical detection of strain 32
3.3. Magneto-optical effects 34

4. Coherent magnetization precession in ferromagnetic (Ga,Mn)As 39

4.1. Sample characterization 40
4.2. The concept of strain induced magnetization precession 43
4.3. First demonstration of strain induced magnetization precession 44
4.4. A posterior theoretical framework 52
4.5. Conclusion 56

5. Selective spin wave excitation in (Ga,Mn)As by ultrafast acoustics 57

5.1. A priori theoretical motivation 57
5.2. Magnetization precession in the magnon picture 60
5.3. Magnetization precession without external magnetic field 61
5.4. Conclusion and perspectives 73

6. High-amplitude magnetization precession induced by shear strain pulses ... 75

6.1. Generation and detection of longitudinal and shear strain pulses 75
6.2. Efficient induction of magnetization precession 80
6.3. Conclusion 91

7. Summary & Outlook 93

8. Acknowledgement 95

9. Bibliography..... 97

10. Publication list..... 107

1. Motivation

„We may not be able to change the wind, but we may set sail better“

Aristoteles

Modern information technology, as fast and efficient as it may have become till the present day, is still searching for even faster and more efficient data processing than ever. The problem arises due to the fact that it is getting ever harder to increase device performance by means of established techniques. These techniques are reaching for the edges of classical physics already and start to deal with nanoscale objects. This is especially true for magnetic storage devices as the magnetic layer film thickness becomes as small as 15 nm with a magnetic grain size of about 10 nm[1]. This raises the problem of nanoscale control of magnetic excitations.

The problem of increasing magnetic data recording performance is especially significant for data writing rates that improve much slower than the data storage density (increase of 4 orders of magnitude in data writing rate compared to 7 orders of magnitude in storage density in the last 50 years[2]) leading to the realization of new concepts like non-magnetic solid state discs based on semiconductor technology already. This illustrates that there is a need for the investigation of high frequency magnetic excitations to realize higher data transfer rates in magnetic devices. The re-writing mechanism in modern hard disk drives (HDDs) relies on the application of a magnetic field oriented antiparallel to the current direction of magnetization. The switching time for a single magnetic domain is determined by the magnetic field pulse on the one hand and the time it takes the magnetization to orient parallel to the applied field. The switching rate is therefore determined by the damping time of precessional orientation of the magnetization from an anti-parallel to an alignment along the applied field. This relaxation rate is determined by the energy transfer of the magnetization to the crystal lattice via the spin-lattice relaxation[3]. Furthermore, for very fast switching procedures induced by magnetic field pulses and for very small grain sizes the magnetic storage material as well as the write heads start to have a very different magnetic response than for slower times and larger grain sizes[4].

A new approach to manipulate magnetic excitations needs to be energy efficient especially for nanoscale magnetic materials, where heat is a problem of great importance as the temperature is a crucial criterion for magnetic order.

This problems lead to the search for different physical concepts that will allow the ultrafast manipulation of magnetic excitations. An interesting tool to investigate the field of magnetization dynamics that is distinctively different from established techniques is the method of picosecond acoustics[5]. This technique allows for the generation of picosecond acoustic pulses with very large strain amplitudes exceeding the limits of linear elasticity[6]. With this technique the interaction of the magnetic sub-system with the crystal lattice can be explored up to very high frequencies up to the THz range[7]. The high acoustic frequencies accessible allow for a correspondingly high temporal resolution experiments as well as experiments with down to nanometer spatial resolution.

The demand of new techniques for magnetization manipulation goes hand in hand with the search for classes of materials that can be tailored to have specific physical properties, which can be exploited to facilitate the realization of new types of devices. One direction of research is inspired by the tremendous success of modern semiconductor technology. Semiconductors can be grown in extremely good crystalline quality and tailored almost arbitrarily considering their electronic and optical properties by methods of molecular beam epitaxy and nano-structuring techniques[8,9]. It is beneficial to reach for this kind of control also for the semiconductors magnetic properties considering all-in-one-chip solutions that are compatible with existing semiconductor based information technology[10]. This topic is covered by the research interest in ferromagnetic semiconductors among other concepts. The ferromagnetic response of the semiconductor is achieved by the incorporation of magnetic atoms and ions in small amounts that are stochastically distributed. The incorporation of these magnetic ions leads also to an intrinsic doping and the existence of these free carriers gives rise to carrier mediated ferromagnetism in so called diluted magnetic semiconductors[11]. These materials show a very high magneto-crystalline anisotropy[12] (MCA) that correlates the orientation of the spontaneous magnetization with the crystal lattice structure.

Although the very first historic experiments with horseshoe magnets show that the magnetization of a magnetic material can be destroyed by either heating the material or by a strong mechanical disturbance the situation is pretty much different if one deviates from the bulk limit or investigates to ultra-fast phenomena*. This thesis presents the approach

* It can be further shown that heat can be a beneficial and necessary condition for so called heat assisted magnetic switching with conventional Oersted switching[13] or that even heat pulses on their own can induce magnetization precession and switching[14].

to use the technique of picosecond acoustics, which is an extremely strong and very well spatially localized mechanical disturbance to excite the precession of magnetization under various conditions and geometries to search for a new, fast and efficient way to control the magnetization state of a ferromagnetic semiconductor. Furthermore, the technique of picosecond acoustics is minimal invasive leading to a very small aftermath of the acoustic pulse on the magnetic system avoiding strong photo carrier generation in the material. There are some key points that need to be addressed to judge, if the use of picosecond acoustic techniques is indeed fruitful for magnetization manipulation: The first question rises about the coupling strength of an ultra-short acoustic pulse to the magnetic system. Furthermore, it has to be investigated if high magnetic fields are needed and possibly avoided to avoid strong, big and costly magnets. As the lack in performance of modern magnetic storage devices lays in the data processing the question rises, if the application of acoustic pulses can achieve high precession frequencies while maintaining the sensitivity to the acoustic pulse applied. And finally the most important point is, wheatear the approach allows for high magnetization precession amplitudes to realize magnetic switching.

The introductory chapter of this thesis covers the principles of picosecond acoustics starting from a brief review of the theory of elasticity to appropriately define the physical parameters. This section is followed by the optical generation process of longitudinal picosecond strain pulses. And the propagation of these strain pulses inside a solid is described. The second part of the introduction is dedicated to the ferromagnetic semiconductor (Ga,Mn)As describing the growth and properties of (Ga,Mn)As and to the introduction of magneto-crystalline anisotropy.

The third chapter focuses on the experimental setup. The optical detection of a propagating strain pulse and the detection of the magnetization state of a material by means of magneto-optical effects are described.

The fourth chapter starts with the experimental details of the structures investigated and the idea of the experiment to induce magnetization precession via the application of picosecond strain pulses to a material with strong MCA is presented. Experimental results are shown that confirm the first realization of coherent magnetization precession induced by a longitudinal picosecond strain pulse and thus answers the question, if a picosecond strain pulse can induce a coherent magnetic excitation. These experimental results are accompanied by a theoretical framework that describes the strain induced magnetization precession for the geometry, when the magnetic field is applied parallel to a hard axis of magnetization.

Based on these preliminary results and the successful demonstration of the principle of sound waves interacting with the magnetization of a ferromagnetic semiconductor, the fifth chapter deals with a magnetic field applied along an easy axis of magnetization. This geometry allows for the excitation of coherent spin waves even without the need for an external magnetic field. The structure is magnetized along an easy axis of magnetization in this case and can be manipulated by the strain pulse even without an applied external field. The advantage of this geometry is the realization of higher precession frequencies and the simultaneous excitation of spin waves of different order can be shown. Furthermore spin waves can selectively be excited, which is a promising property with respect to concepts of spin current control[15].

Longitudinal strain pulses only induce the magnetization precessions with limited amplitudes. The theoretical prediction of a stronger influence of shear acoustic waves on ferromagnetic materials[16] leads to the necessity to develop a possibility to generate shear acoustic waves and to apply them to a ferromagnetic film. This technique is addressed in chapter six and the application to a (Ga,Mn)As film grown on a crystalline substrate oriented along a high index crystallographic direction is demonstrated. With this approach, magnetization precession amplitudes as large as 10% of the saturation magnetization can be reached. The concept is only limited by the available laser power and can in general be used to realize precession amplitudes that allow for magnetization switching.

2. Introduction

„Beliefs are more dangerous enemies of the truth than lies“

Friedrich Nietzsche

The first part of this introductory chapter is dedicated to the technique of picosecond acoustics. The starting point is a short overview of acoustic frequencies ranges and their applications to impart a connection to the picosecond strain pulses utilized in this thesis. This is followed by the principles of elastic theory, as the language of elasticity is used to describe the technique of picosecond acoustics. This technique is adressed in the following by the explanation of a theoretical model to impart the generation of picosecond acoustic pulses by laser exciting a metal transducer. Furthermore, the key considerations of dealing with real rather than model strain pulses are discussed. This is followed by the description of the strain pulse propagation under linear as well as non-linear conditions.

The second part of the introduction deals with the material system (Ga,Mn)As and aims on giving insight in the formation of ferromagnetism by the interaction of localized manganese spins with a resident hole distribution. The result of this interaction is a ferromagnetic material with a strong MCA.

2.1. From sound to hypersound

Sound is one of the elemental physical phenomena that plays an important role in the life of humans and other vivid matter since the very beginning of life itself. The range of acoustic frequencies and physical examples is depicted in Figure 2.1-1. Humans refer to ‘sound’ as acoustic frequencies in the frequency range from 20 Hz – 20 kHz. This the original range of acoustic frequencies that can be sensed by the human ear[17]. Animals have a broader spectrum of sensible acoustic frequencies ranging from infrasound of crocodiles and elephants to ultrasound in the navigational system of bats and dolphins. These augmented abilities of animals inspired scientists and engineers to utilize a broader spectrum of acoustic frequencies for mankind as well[18]. The results are modern devices that use ultrasound for medical imaging, distance measurements in cars and the navigation of submarines. Extending the frequencies to the MHz range leads to common electrical and electro-optical devices like acousto-optic modulators in optics or piezo-acoustic transducers for non-destructive testing or movement with nm precision[19].

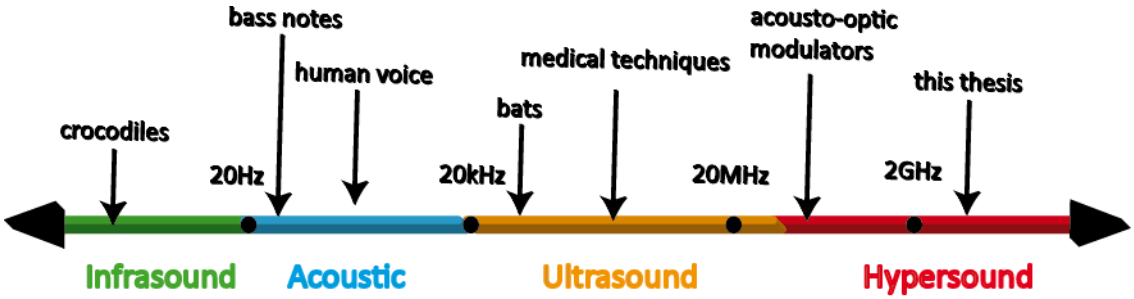

Figure 2.1-1: Acoustic frequency ranges and their physical interpretation

However, these techniques are limited to the frequency range of a few GHz. The technique of picosecond acoustics converts optical energy to acoustic energy and allows for the excitation of strain pulses with acoustic frequencies up to the THz regime and very high strain amplitudes that reach corresponding static pressures in the GPa range[7]. Moreover, the strain is spatially very well localized. This feature allows for laboratory scale seismological experiments. The propagation of these high frequency acoustic wave packets is not diffusive, but ballistic[20,21]. The propagation over macroscopic distances is strongly temperature and material dependent. A low temperatures environment may be necessary for certain materials due to strong damping of high frequency acoustic waves at elevated temperatures[22]. The high frequencies achievable and the high strain amplitudes are the main advantages of the technique of picosecond acoustics compared to frequency limited conventional techniques using piezoelectric transducers[19]. The high frequency acoustic wave packets have correspondingly low wavelength in the range of a few nanometers that allows for the non-destructive probing of nano-objects[23] that could only be spatially investigated by x-ray analysis so far[24]. Furthermore, elastic parameters of these nano-objects can be determined that may significantly differ from known values for bulk materials[25,26].

2.1.1. Basic principles of elasticity

The generation of picosecond acoustic pulses is a concept based on the idea of elasticity. Elasticity is the theory of the mechanics of a (solid, homogeneous) body. It answers the question, how a body deforms under the action of (external) forces. It is a macroscopic theory and therefore does not deal with atomic and molecular forces and only works on length scales large compared to interatomic distances. The theory is based on reversibility and therefore no overlapping of the material nor the formation of holes and fractures are included[27].

The position of each infinitesimal part of the body is described by a vector $\vec{x}$ (with elements x_i) in an arbitrary coordinate frame. If external forces are applied to the body, it

will react by the rearrangement of the positions of the infinitesimal parts described by new vectors $\vec{x}'$. The change $\vec{u}$ of each point

(2.1.1) $$\vec{u} = \vec{x}' - \vec{x}$$

is called the *displacement*[28] and gives the overall change of the configuration of points of a body. This definition is not practical, if only the actual forces acting on the body shall be considered: simple translations as well as rotations give displacements. In other words the displacement is not independent on the choice of the origin of the coordinate system. It is therefore handy to consider the infinitesimal length *dl* separating two neighboring points in the undeformed and *dl'* in the deformed body separated by a connecting vector $d\vec{x}$ and $d\vec{x}' = d\vec{x} + d\vec{u}$ before and after deformation, respectively. The length in the deformed body is

(2.1.2) $$dl'^2 = \left(dx_i + du_i\right)^2 = dl^2 + 2du_i dx_i + du_i^2$$

using Einstein's summation convention. Substituting $du_i = \frac{\partial u_i}{\partial x_k} dx_k$ and rearranging indices gives[29]

(2.1.3) $$dl'^2 = dl^2 + 2\eta_{ik} dx_i dx_k .$$

With the definition of the symmetrical tensor

(2.1.4) $$\eta_{ik} = \frac{1}{2}\left(\frac{\partial u_i}{\partial x_k} + \frac{\partial u_k}{\partial x_i} + \frac{\partial u_l}{\partial x_k}\frac{\partial u_l}{\partial x_i}\right)$$

called the *strain tensor*. The strain tensor is a symmetric tensor and gives the relative changes of the infinitesimal length when a body is deformed[27]. In general, deformations that occur for a solid body cause only small strains*. So the second order term for the strain can be omitted with good accuracy. This leads to the more familiar representation of the strain tensor found in literature[29]

* This assumption may be violated for example in the case of thin rods or thin plates under huge loads used in engineering applications.

$$(2.1.5)\ \eta_{ik} = \begin{bmatrix} \eta_{11} & \eta_{12} & \eta_{13} \\ \eta_{21} & \eta_{22} & \eta_{23} \\ \eta_{31} & \eta_{32} & \eta_{33} \end{bmatrix} = \begin{bmatrix} \frac{\partial u_1}{\partial x_1} & \frac{1}{2}\left(\frac{\partial u_1}{\partial x_2} + \frac{\partial u_2}{\partial x_1}\right) & \frac{1}{2}\left(\frac{\partial u_1}{\partial x_3} + \frac{\partial u_3}{\partial x_1}\right) \\ \frac{1}{2}\left(\frac{\partial u_2}{\partial x_1} + \frac{\partial u_1}{\partial x_2}\right) & \frac{\partial u_2}{\partial x_2} & \frac{1}{2}\left(\frac{\partial u_2}{\partial x_3} + \frac{\partial u_3}{\partial x_2}\right) \\ \frac{1}{2}\left(\frac{\partial u_3}{\partial x_1} + \frac{\partial u_1}{\partial x_3}\right) & \frac{1}{2}\left(\frac{\partial u_3}{\partial x_2} + \frac{\partial u_2}{\partial x_3}\right) & \frac{\partial u_3}{\partial x_3} \end{bmatrix}.$$

The diagonal elements cover volume changes associated with compressions and tensions, while the off-diagonal elements represent shear strains. To illustrate the geometry of the shear components it is worth to point out that for example $\frac{\partial u_1}{\partial x_2}$ is the rotation around $\vec{e}_3$ towards $\vec{e}_1$ of a line element parallel to $\vec{e}_2$, if the $\vec{e}_i$ are unit vectors of a Cartesian coordinate system. The rotation for the other elements $\frac{\partial u_i}{\partial x_k}$ works in the same manner[29].

The strain is not a property of a crystal itself, but it describes the reaction of the crystal to forces acting on it. Therefore the strain does not need to conform with the crystal symmetry unless the acting forces do so[29].

If a body is considered to consist of small volume elements, these can only interact with other volume elements by their surfaces within the limits of the theory of elasticity*. Therefore the quantity

$$(2.1.6)\qquad \sigma = \frac{F}{dA}$$

is defined as the force F acting on the surface element dA. This quantity is called *stress*[27]. It has the dimension of a pressure. If a body is in a state of equilibrium (but not free of stress), Newton's 3rd law states that the forces inside the body compensate each other and the body only interacts with its surrounding by the forces applied to its surface. To account for the different geometries of applied forces the stress is a (symmetric)† tensor

* The situation changes when macroscopic electric or magnetic fields are present due to piezoelectric or magnetostrictive effects. Also other volume forces like gravity are ignored.

† The tensor is only symmetric, if there are no torques acting on the body[27].

(2.1.7) $$\sigma_{ij} = \begin{bmatrix} \sigma_{11} & \sigma_{21} & \sigma_{31} \\ \sigma_{12} & \sigma_{22} & \sigma_{32} \\ \sigma_{13} & \sigma_{23} & \sigma_{33} \end{bmatrix}.$$

Analogous to the case of the strain tensor the diagonal elements σ_{ii} represent compressive (negative valued) and tensile (positive valued) stresses. The off-diagonal elements describe shear stresses. In the equilibrium state of matter as stated above the forces causing the internal stresses have to vanish for every volume element giving the conditions of equilibrium of a deformed body to[27]

(2.1.8) $$\sum_k \frac{\partial \sigma_{ik}}{\partial x_k} = 0.$$

In the linear branch of the theory of elasticity a linear connection between the stress and strain

(2.1.9) $$\sigma_{ij} = C_{ijkl}\eta_{kl}$$

called *Hook's Law* with the 4th rank tensor C_{ijkl} named the *stiffness*[*] of a crystal is assumed[29]. This 4th rank tensor has 21 independent entries in the low symmetry case for a real crystal. For crystals with a high symmetry, the number of independent entries is reduced and can be as small as 3 for the case of a cubic crystal[30]. For an actual material the tensor components are usually expressed in the historically grown formulation with parameters like the Bulk Modulus and Poisson's Ratio. In general Hook's Law only works for small strains and stresses, respectively. For larger strains, non-linear relations have to be taken into account and finally the physics of plasticity has to be considered, when the strain is no longer reversible, but formation of cracks and dislocations start to play a major role. The strains realized in the experiments presented are too small to realize plastic deformations of the crystal, but non-linear responses of the crystal have to be considered the highest strains generated by the method of picosecond acoustics.

[*]By incorporating complex values for the stiffness the effect of damping of strain waves can be included.

2.1.2. Generation of picosecond strain pulses

This section describes a technique to generate a picosecond strain pulse. This is the standard experimental method of picosecond acoustics.

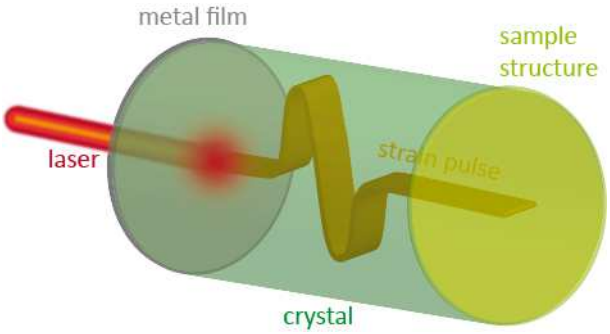

Figure 2.1-2: Basic scheme of the excitation of picosecond strain pulses by the technique of picosecond acoustics. An ultra-short laser pulse heats a thin metal film. The rapid thermal expansion induces a strain pulse into the crystalline material. On the opposite side of the crystal a sample structure is deposited that interacts with the strain pulse.

The general process is depicted in Figure 2.1-2. It works as follows: An opaque material with a few nanometer penetration depth for the exciting laser pulse is needed. This is typically realized by a metal film that is evaporated onto the crystalline material and is used as an opto-elastic transducer[*]. A high intense laser pulse with sub-picosecond duration illuminates the film and is absorbed. The absorption of the light pulse causes a picosecond heating of the film that induces a thermal stress due to rapid thermal expansion. This is the reason for the buildup of a picosecond strain pulse inside the metal film. The strain pulse is traveling away from the thin region where it is generated and is transferred through the film/crystal interface. The pulse is travelling away from the metal film and can finally be utilized in many different ways to manipulate structures located at the opposite side of the crystalline material or to investigate material parameters.

The details of the excitation process are described in the following. To investigate this general scheme quantitatively some assumptions have to be made that are evaluated to apply for the experimental conditions used in later chapters. The model geometry is shown in Figure 2.1-3. A metal film of thickness d is illuminated by a sub-picosecond light pulse penetrating into the free surface of the metal exponentially with a penetration depth ζ much smaller than the film thickness. The diameter of the area A illuminated by the laser has to be much greater than d and ζ. In this case the total deposited energy per unit volume W along the penetration direction z can be described by[33]

$$W(z,t) = (1-R)\frac{Q}{A\zeta} e^{-z/\zeta} \Theta(t), \tag{2.1.10}$$

[*] The use of a metal film is not a necessary condition, as excitation in nanostructured materials[31] offers aslo other excitation mechanisms than heating. For example, direct illumination of a bulk material is possible, if the optical penetration depth is sufficiently small or if the material is photostrictive[32].

if an initial energy *Q* of the light pulse and a reflectivity *R* of the film is assumed. The Heaviside function is depicted as $\Theta(t)$. Furthermore, the initially absorbed energy of the electrons of the metal has to be transferred to the lattice instantly (much faster than the electron diffusion that spreads the energy into the metal film). The absorbed energy gives rise to a temperature rise ΔT that is only z-dependent and of the form $\Delta T = \frac{W}{C}$ with the specific heat per unit volume *C*. The deposited energy for this case is shown in Figure 2.1-3.

The thermal stress is isotropic by nature in an isotropic material[33]

(2.1.11) $$\sigma_{thermal} = -3\alpha B \Delta T$$

with the isotropic linear expansion coefficient α and the bulk modulus B.

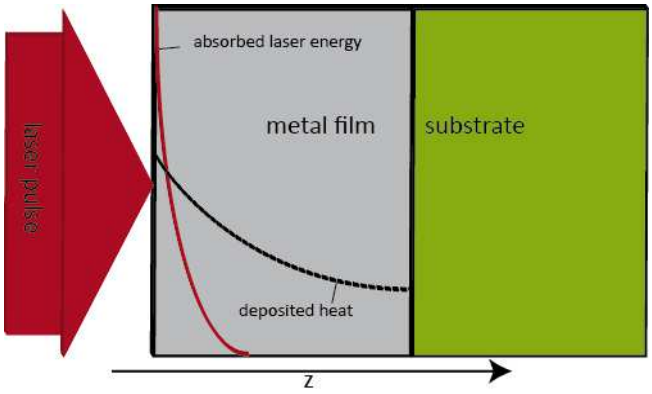

Figure 2.1-3: Model geometry for the quantitative analysis of the excitation of picosecond strain pulses. An ultra-short laser pulse illuminates a metal film and the laser energy is absorbed in a thin region (red line) near the surface. The deposited heat (black dashed line) is not restricted to the near surface region and spreads further into the metal film.

As the stress is isotropic only tensile and compressive strains appear. Due to these facts the equations of motion[27]

(2.1.12) $$\rho \frac{\partial^2 u_i}{\partial t^2} = \frac{\partial \sigma_{ij}}{\partial x_j}$$

have to be solved with the stress tensor[33]

(2.1.13) $$\sigma_{ik} = \left((B - 2\mu) \frac{\partial u_i}{\partial x_k} - 3\alpha B \Delta T \right) \delta_{ik} .$$

The quantity μ is called the shear modulus. The initial condition is zero strain at every coordinate and the boundary condition is zero stress (longitudinal as well as shear stress[34]) at the free surface

(2.1.14)
$$\begin{aligned} u_i(x_i, t=0) &= 0 \\ \sigma_{zz}(z=0, t) &= 0 \end{aligned}.$$

Solving the differential equation with the appropriate boundary conditions gives the solution of a propagating strain pulse in the z-direction with longitudinal polarization only[33]:

(2.1.15)
$$\eta_{zz}(z,t) = (1-R)\frac{Q\alpha}{A\zeta C}\frac{1+\upsilon}{1-\upsilon}\left[\underbrace{e^{-z/\zeta}}_{static} \underbrace{-\frac{1}{2}e^{-z-vt/\zeta} - \frac{1}{2}e^{-|z-vt|/\zeta}\,\mathrm{sgn}(z-vt)}_{propagating}\right].$$

The *sgn*-function giving the sign of the argument, Poisson's ratio υ and the longitudinal sound velocity v is given by

(2.1.16)
$$v^2 = 3\frac{1-\upsilon}{1+\upsilon}\frac{B}{\rho}.$$

The actual driving source of the moving strain pulse is the gradient in the heat extension along the z-direction and not the heat extension itself. It is assumed that the heat extension has no gradient in x- and y-direction as the heated area is considered large compared to penetration depth so only z-components are generated. As long as the strain pulse propagation distance *D* through the material is small compared to the ratio of the excitation area *A* and the characteristic wavelength *λ* of the strain pulse $D << A/\lambda$, the strain can be considered as a superposition of plane waves[21]. This is called the acoustic near field regime. This assumption is fulfilled in the experiments as for a characteristic wavelength of the strain pulse of 50 nm the propagation distance has to be as large as a few millimeter to leave the near field regime, but the structures investigated are not thicker than 100 µm. The result of the instant heating of a metal film with a short laser pulse is therefore a heated surface region that exhibits "static", located thermal expansion and a bipolar strain pulse traveling in z- direction as shown in Figure 2.1-4.

It should be noted at this point that the picture given above is simplified in many aspects. It describes the general shape of the strain pulse, but fails to predict the real duration of the pulse for example. Some shortcomings of the simplified picture shall be noticed in the following. The energy transfer of the absorbed light goes dominantly to the electronic system. Electrons will spread into the metal by diffusion or ballistic transport[35]. The electron specific heat is typically much smaller than the lattice specific heat. Therefore electron temperatures around 1000 K[36] are realized with moderate laser excitation

densities. The energy transfer between the electron and lattice system is described by the electron-phonon coupling constant. The energy is thus much wider distributed in the metal film than by considerations of optical absorption depth alone[35]. Furthermore, the actual diffusion of heat in the material itself needs to be taken into account for metals and leads to a smoothening of the strain pulse profile shown in Figure 2.1-4. These effects are usually considered in the so called Two-Temperature models[35] as is shown schematically in Figure 2.1-5.

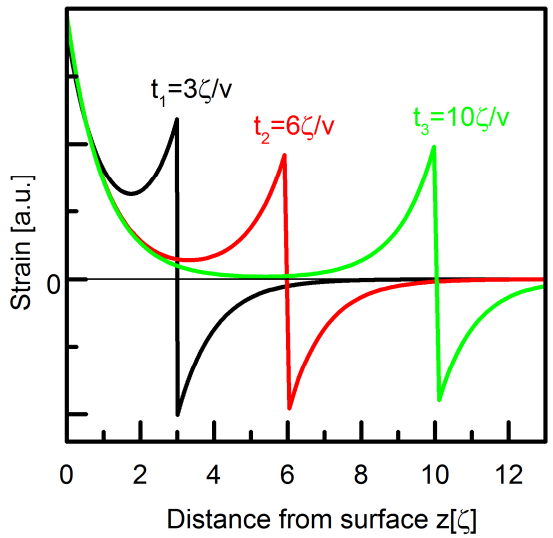

Figure 2.1-4: The strain evolution for the static surface strain and moving strain pulse according to equation (2.1.15) at 3 representative times. t_1 corresponds to a time shortly after the laser excitation, when the static and moving contributions to the strain clearly overlap. The separation continues for t_2 and for t_3 the separation of the moving, bipolar strain pulse from the static heat extension at the surface becomes evident.

On the other hand, it is hardly possible to define an appropriate temperature for the initial electron distribution after optical excitation as it is intrinsically a non-thermal distribution[35]. It therefore takes some time, typically less than one picosecond, until the electrons thermalize. The differences in energy deposition for the Two-Temperature model and a more sophisticated one taking a non-thermal electron distribution[37] show a significant difference in energy deposition within the first picosecond of excitation leading to a broadening of the strain pulse.

In general the shape of a picosecond strain pulse generated in a metal film by the method described above and transmitted into a substrate can be described very well by the derivative of a Gaussian pulse[38]

$$\eta(t)=\frac{2G\varsigma}{v\tau^2}(1-R)\sum_{j=0}^{\infty}R^j\left(t-\frac{(2j+1)d}{v}\right)\exp\left[-\frac{1}{\tau^2}\left(t-\frac{(2j+1)d}{v}\right)^2\right], \tag{2.1.16}$$

where d is the film thickness, R is the reflection coefficient for a longitudinal strain pulse at the interface (see equation(2.1.17)) of the metal film and the substrate material, G

is a dimensionless parameter that depends on the pump density and transducer parameters[35]. The summation accounts for the fact that the strain pulse is only partly transmitted into the substrate and a part is reflected back into the metal film. The index j counts the number of cycles of the strain pulse inside the metal film. The value of the parameter τ is initially defined as the time the strain pulse needs to travel through the penetration depth $\tau = \varsigma / v$. But it may be adjusted to account for a broader strain pulse due to diffusion broadening by different processes as mentioned above.

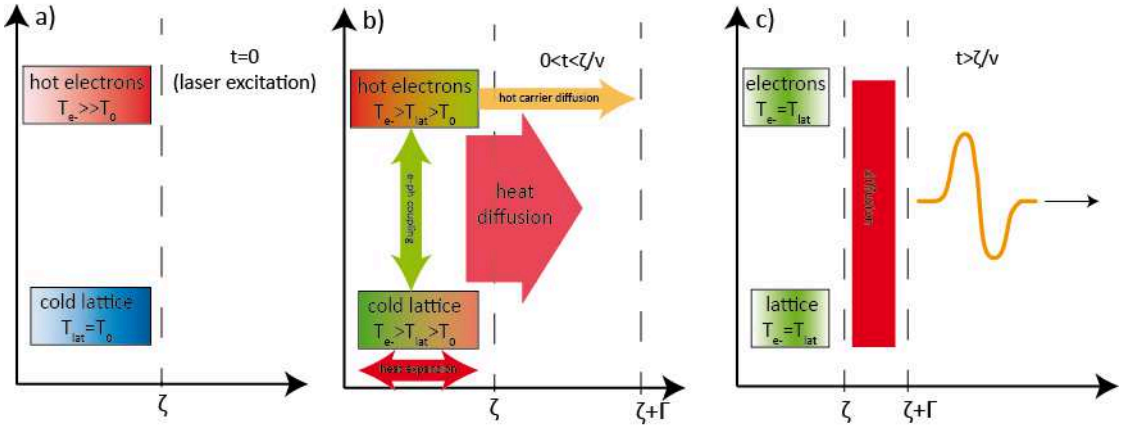

Figure 2.1-5: Schematic mechanics of the Two-Temperature model: a) Hot electrons are generated in the region of the penetration depth ζ by the laser excitation ($t = 0$) while the lattice stays at the initial temperature T_0, b) in the time interval $0 < t < \zeta/v$ the hot electrons and the cold lattice begin to reach thermal equilibrium again. The heat expansion starts to produce thermal strain accompanied by heat and hot carrier diffusion that lead to an additional broadening of the heated area described by the diffusion length Γ responsible for the strain pulse generation. c) for times $t > \zeta/v$ the electrons and the lattice have reached thermal equilibrium and a bipolar strain pulse is launched.

As depicted in Figure 2.1-3, not a free standing membrane is excited, but a film attached to a substrate material. This has not been accounted for yet. One important feature is the acoustic matching of the film and substrate material that can be described with the reflection coefficient R of an acoustic wave that travels from medium 1 into medium 2 described by [21]

(2.1.17) $$R = \frac{Z_2 - Z_1}{Z_1 + Z_2}$$

with Z_1 and Z_2 being the acoustic impedances of the materials one and two. These quantities may show strong frequency dependences and therefore the reflectivity is a frequency dependent quantity in the general case. For a perfect matching of the 2 materials there is no reflection of the acoustic wave at the interfaces. If there is an impedance mismatch the reflected wave might undergo a phase shift of π depending on the ratio of the acoustic impedances[21].

All this assumes a perfect mechanical contact of the film and the substrate and flat interfaces. If the mechanical coupling of the film and the substrate is poor, it may result in a ringing phenomenon similar to a free standing membrane[39]. If on the other hand a significant amount of roughness is present at the interface, this leads to strong phonon scattering especially at high frequencies[22]. This can be understood, if one asks for the wavelength of an acoustic wave with a frequency of 100GHz in a typical solid state material. It is on the order of a few 10 nm. For much longer wavelengths the roughness will be "averaged", but if the roughness is on the order of the wavelength the influence on the strain pulse can be tremendous especially for high frequencies [22].

2.1.3. Linear and non-linear strain pulse propagation

The previous section covered the generation of a picosecond strain pulse using a metallic opto-elastic transducer illuminated by a laser pulse. This section deals with the problem of a strain pulse that propagates through an elastic medium.

In the experiments considered in this thesis the strain pulse is propagating in the acoustic near field regime (as described in the previous section). This means the strain pulse travels ballistically, it is not subjected to diffraction and can be treated as a superposition of plane waves[21]. If a strain pulse travels through a solid material the attenuation can be particularly strong for high frequency components at elevated temperatures[40]. The attenuation is caused dominantly by the anharmonic interaction with thermal phonons[21]. At cryogenic temperatures propagation distances of more than several millimeters are possible without a significant change in the shape of the strain pulse for a lot of materials[21] (see Figure 2.1-7a).

The situation changes, if strain pulses with high amplitudes are considered rendering the validity of linear elasticity inappropriately. The reason for the deviation from the linear elasticity model is the anharmonicity of the interatomic potentials that becomes important for larger deviations of the atoms from their equilibrium positions[41,42]. And not only high strain amplitudes are a limitation for linear elasticity, but acoustic frequencies up to the THz regime have corresponding wavelength so short that the finite spacing of the atomic lattice starts to have an effect[6]. Or in other words: the acoustic wave vector becomes so large that it reaches the edges of the Brillioun zone. This effect can be incorporated by an additional dispersive term in the standard equation of motion (2.1.12). Dispersion plays a significant role for acoustic wavelengths shorter than about 20 times the lattice spacing[30]. The deviation from linear elasticity is considered by addition of the

lowest order term of non-linearity, which is cubic.* This leads to the following wave equation† in the displacement[44]

(2.1.18) $$\underbrace{\frac{\partial^2 u}{\partial t^2} = v^2 \frac{\partial^2 u}{\partial z^2}}_{equation\ of\ motion} + \underbrace{\left(\frac{C_{111}}{\rho} + 3v^2 \right) \frac{\partial u}{\partial z} \frac{\partial^2 u}{\partial z^2}}_{non-linearity} + \underbrace{2v\gamma \frac{\partial^4 u}{\partial z^4}}_{dispersion}$$

with the stiffness tensor component C_{111}, the equilibrium density ρ and the dispersion parameter γ for a longitudinal wave propagating in the z-direction. The coefficient γdescribes the strength of the dispersion following the dispersion relation[22]

(2.1.19) $$\omega(k) = vk - \gamma k^3$$

with the wave frequency ω. To be independent from the reference this equation has to be formulated in the strain rather than in the displacement. For the longitudinal propagation in z-direction, the definition of strain (2.1.4) simplifies to $\eta = \frac{\partial u}{\partial z}$. By differentiating (2.1.18) with respect to z it reads as follows[21]:

(2.1.20) $$\frac{\partial^2 \eta}{\partial t^2} = v^2 \frac{\partial^2 \eta}{\partial z^2} + \left(\frac{C_{111}}{\rho} + 3v^2 \right) \frac{\partial}{\partial z} \left(\eta \frac{\partial \eta}{\partial z} \right) + 2v\gamma \frac{\partial^4 \eta}{\partial z^4}.$$

Solutions of this extended wave equation are not trivial, but it can be related to the well know Korteweg-De-Vries (KdV) equation

(2.1.21) $$\frac{\partial \eta}{\partial t} = -v \frac{\partial \eta}{\partial z} - \left(\frac{C_{111}}{2\rho v} + \frac{3}{2} v \right) \eta \frac{\partial \eta}{\partial z} - \gamma \frac{\partial^3 \eta}{\partial z^3}$$

and the solutions of (2.1.21) are also solutions of (2.1.20), but not vice versa[21]. The implications of dispersion and non-linearity are illustrated in Figure 2.1-6.

* A deduction of these terms based on either microscopic models or energy considerations[43] can be found in details in the literature.

† Although, the basic wave equation describes many basic model systems, it describes only a small fraction of wave phenomena in real physical systems. So here a standard technique is used, where phenomenological terms are added to the basic wave equation to describe a physical system more realistically.

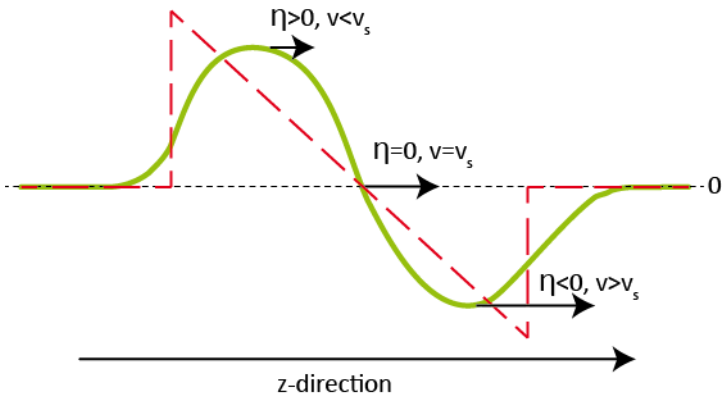

Figure 2.1-6: Evolution of a bipolar strain pulse traveling in z-direction. Large positive strains travel sub-sonically while negative strains travel supersonically. This leads to the formation of a N-shaped shock wave.

Taking into account pulse broadening and smearing effects as discussed in the end of section 2.1.2, a very good approximation for the real strain pulse injected into the substrate is a bipolar pulse described by the derivative of a Gaussian distribution (see equation (2.1.16)). The dispersion tends to flatten the pulse as it tends to transfer energy from Fourier components at high frequencies to low ones. The non-linearity tends to steepen the bipolar pulse by affecting the velocity of individual parts of the strain pulse[45]. Compressive parts of the strain pulse tend to travel faster than the normal sound velocity and tensional strains travel slower[21].

Finally, the influence of non-linearity and dispersion turns the pulse into an N-shaped shock wave, if the initial strain amplitude is big enough for the non-linearity and dispersion to be relevant[45]. Strain pulses of small strain may travel for distances up to millimeters without strong distortion of the pulse. The distortion of the pulse naturally changes the frequency distribution of the strain pulse. The result for a model bipolar strain pulse with initial amplitude of $1 \cdot 10^{-3}$ travelling through (100)-GaAs is shown in Figure 2.1-7.

During the propagation the described steepening of a initially smooth, bipolar pulse (Figure 2.1-7 a) to a N-shaped shock wave is observed (Figure 2.1-7 c) and the frequency contend extends well up to the sub-THz regime. A peculiarity of the KdV solution is observable in panel e): short and high amplitude unipolar peaks appear well seperated in the front of the strain pulse. There are two general classes of solutions for the KdV-equation[21]: Standing waves (cnoidal) and a propagating unipolar solution called a soliton*. Based on (2.1.21) they have the form

* Soliton solutions are found in many wave equations for example also in the non-linear Schrödinger equation[46]. Solitons are a very robust wave phenomenon with remarkable properties and are observed as Tsunamis in water waves[47] or can be used in optical fiber communications by light solitons[48].

$$\eta(z,t)=\eta_0\,\mathrm{sech}^2\left(\left(\frac{\left(C_{111}+3\rho v^2\right)\eta_0}{24\rho v\gamma}\right)^{1/2}(z-Ut)\right) \tag{2.1.21}$$

with the peak strain amplitude η_0 and the soliton velocity

$$U=v+\underbrace{\frac{\left(C_{111}+3\rho v^2\right)}{6\rho v}}_{Q}\eta_0 \tag{2.1.22}$$

where the factor Q is usually negative. It follows from (2.1.22) that solitons are always supersonically as (2.1.21) has only real solutions for compressional strains[21]. This implies that solitons are always compressions.

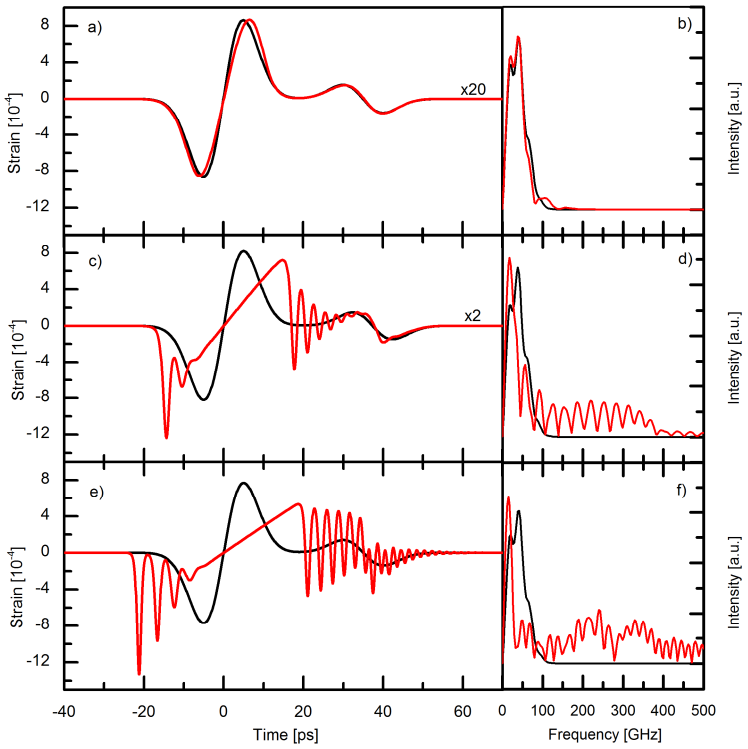

Figure 2.1-7: panels a),c) and e) show the evolution of a model strain pulse directly after excitation (black line) and after propagation through 110 µm of GaAs substrate taking into account an evolution according to the KdV equation for an initial strain pulse amplitude of $4\cdot10^{-5}$, $4\cdot10^{-4}$ and $8\cdot10^{-4}$, respectively. The right hand side (b), d), e)) shows the corresponding acoustic frequency spectra obtained by Fast Fourier Transform for the strain pulse directly after excitation (black line) and after the travelling through 110 µm GaAs.*

Any given strain pulse distribution (with compressive parts) will finally cause solitons to appear†, if the propagation distance is long enough for the soliton to form. As

* The calculations of this strain pulses have been performed by Peter van Capel from the Universiteit Utrecht, Netherlands.

† The amazing procedure to proof this statement works as follows[21]: The initial strain pulse distribution is simply put into the Schrödinger equation as a potential with a simple factor and then the number of bound states are investigated by standard techniques of quantum mechanics. For a compressive strain, this will lead to at least one bound state in any case.

can be seen in Figure 2.1-7 d) the frequency distribution is further extended to higher frequencies by the soliton formation. Solitons can have very high peak amplitudes and a width as small as a few nm and therefore extends the abilities of picosecond acoustics to e.g. probing nanostructures nondestructively or investigating THz phenomena[49].

Up to now no attenuation term has been introduced. Depending on the investigated frequency and temperature range there are many different mechanisms that make a dissipative contribution to the traveling strain pulse. But the experiments that are described in this thesis are all performed at low temperatures and relatively short pulse propagation distances. Due to this fact attenuation effects are expected to be negligible[21,50] and therefore omitted in the theoretical treatment and phenomenological discussions.

2.2. The diluted magnetic semiconductor (Ga,Mn)As

"Der Restwiderstand ist ein Dreckeffekt und im Dreck soll man nicht wühlen."

Wolfgang Pauli

The research in semiconductors and the engineering of their electrical properties and structure lead to the development of the era of information technology. The main challenge was the growth of high purity and crystalline semiconductors that has been mastered for the most common materials in applications, like Si, Ge or GaAs[51].

From the technological point of view it is an interesting option to utilize ferromagnetism in semiconductors*. It may allow all-in-one-chip solutions exploiting the electron charge and spin at the same time[57]. But typical materials used in applications are not ferromagnetic and semiconductors showing ferromagnetic behavior are not compatible with technological solutions in mass production[57]. At this point the "Dreck" becomes an opportunity. In the same manner as electric doping changes the conductivity, it is possible to create a ferromagnetic response of the system by the spurious incorporation of magnetic ions in a non-magnetic III-V semiconductor host lattice. Due to the low concentrations of magnetic ions and the random distribution inside the material, these semiconductors are called Diluted Magnetic Semiconductors (DMS). A model system under study in this field is the DMS (Ga,Mn)As[58]. The next section will introduce the material system as a material grown far from equilibrium conditions. This is followed by the

* Novel aspects of ferromagnetic semiconductors are for example the electric field control of magnetic anisotropy[52] and ferromagnetism itself[53] or the realization of spin-injection-structures by technological relevant semiconductors as a starting point of the realization of spin logic[54] and spin based information processing[55] or functional spin-polarized light emitting diodes[56].

explanation of the origin of ferromagnetism in (Ga,Mn)As. Finally the concept of magnetic anisotropy will be introduced for the example of (Ga,Mn)As.

2.2.1. Structure and growth of (Ga,Mn)As films

It took almost a decade after the demonstration of the first DMS (In,Mn)As[59] in 1989 until (Ga,Mn)As[60] was grown successfully for the first time by Ohno et al. in 1996. The host lattice is GaAs that grows naturally in the Zink-blende structure. The thermo-dynamical solubility limit of Mn in GaAs is as low as 0.1 % and not sufficient to realize magnetic order. For this reason new technologies had to be developed that ensure a growth of (Ga,Mn)As far from thermo-dynamic equilibrium conditions to achieve a much higher doping concentration of Mn. Low Temperature Molecular Beam Epitaxy (LT-MBE) allows for this non-equilibrium growth with Mn concentrations exceeding 10 %. LT-MBE growth is characterized by a substrate temperature during growth of typically less than 300 °C[60]. The GaAs host lattice with the two most common incorporations of Mn is shown in Figure 2.2-1. Mn can replace As on the one hand. It is the electronically less favored interstitial position and acts as a double donator in this configuration. Further this configuration is disturbing the formation of ferromagnetism. This defect is thermodynamically unstable and can be reduced by low temperature annealing*.

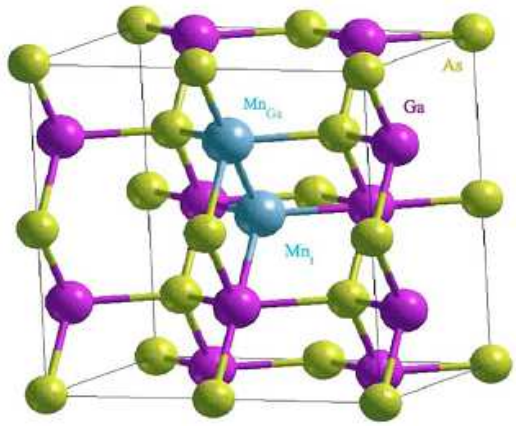

Figure 2.2-1: The fcc host lattice GaAs with Mn incorporations is shown. The manganese is either replacing the Ga or the As in the Zink-Blende structure[11] leading to different carrier doping behaviors.

The desired incorporation of Mn into the GaAs host lattice is at the cation site replacing Ga^{3+} with Mn^{2+}. This is the electronically most favorable and therefore statistically more likely incorporation of Mn. The Mn^{2+}-ion has no angular momentum (L = 0) and a Spin S = 5/2[58] resulting from 5 electrons each occupying one of the 5 orbitals in the half filled d-shell and a g-factor g = +2. Due to its electronic configuration, it acts as an acceptor in the band structure of GaAs giving rise to an intrinsic p-doping. It is in the

* The low temperature annealing is typically very close to the growth temperature. For higher annealing temperatures the formation of MnAs clusters occur[60].

nature of a diluted alloy like (Ga,Mn)As that the incorporation of Mn in the host lattice is random and therefore leads to a certain amount of disorder present in the system that has to be addressed in the microscopic picture. As (Ga,Mn)As is a material grown far from thermo-dynamic equilibrium, the actual properties of a (Ga,Mn)As film are strongly dependent on the growth parameters as illustrated in Figure 2.2-2 as well as post growth treatment[61].

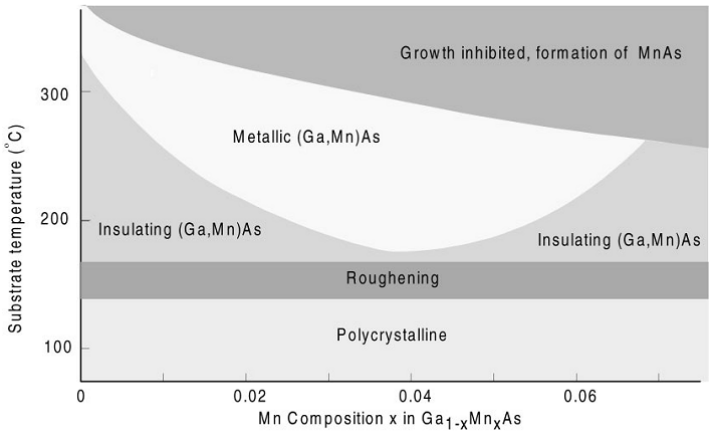

Figure 2.2-2: Parameter space of LT-MBE growth of thin film (Ga,Mn)As. Only above a substrate temperature of about 175°C monocrystalline (Ga,Mn)As films can be grown. The electric properties of the film depends on the amount *x* of incorporated Mn and the substrate growth temperature[62]

It is possible to grow monocrystalline insulating and metallic (Ga,Mn)As films for different research interests. Lower substrate temperatures lead to polycrystalline growth and higher substrate temperatures to the formation of metallic MnAs clusters and crystallites[62]. Increasing the Mn concentration well above 10 % does not improve the magnetic properties* any further.

As (Ga,Mn)As is grown by LT-MBE on substrates like GaAs, it adapts to the substrates lattice structure due to lattice matched growth. (Ga,Mn)As has a larger lattice constant than GaAs and therefore exhibits growth induced uniaxial strain† that can be estimated by the differences in the lattice constants a_{GaAs} and a_{GaMnAs} [64]

$$\eta = \frac{\left(a_{GaMnAs} - a_{GaAs}\right)}{a_{GaMnAs}}. \qquad (2.2.1)$$

The lattice constant of (Ga,Mn)As can be estimated using the concentration *x* of Mn in $Ga_{1-x}Mn_xAs$ and (the hypothetical Zink-Blende) lattice constant of MnAs using

* This topic is still under debate. One of the reasons is the direct interaction of Mn on neighboring sites being responsible[63].

† The assumption of uniform strain is valid and relaxation may not occur for films as thick as a few micrometer[62].

Vegard's law[62] that assumes a linear change of the lattice constant with increasing Mn concentration and is a very good approximation for (Ga,Mn)As as is shown in Figure 2.2-3.

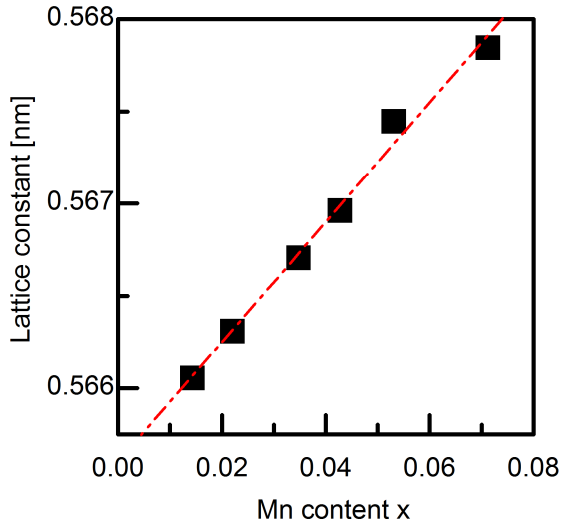

Figure 2.2-3: Change in (Ga,Mn)As lattice constant caused by the increase of the Mn content *x* following the linear dependence predicted by *Vegard*'s law[62]

The lattice matched growth leads to the useful possibility to tune the strain conditions by choosing an appropriate substrate layer material[65]. Strains achieved in real films are typically below 0.5 %[65]. The structure of (Ga,Mn)As described here is the key to the understanding of the origin of ferromagnetism in this material that is described in the next section.

2.2.2. Magnetism in (Ga,Mn)As

A possible description of the origin of ferromagnetic order in (Ga,Mn)As is based on the so called carrier-induced ferromagnetism. As (Ga,Mn)As is a *diluted* magnetic semiconductor, the Mn ions are randomly distributed and therefore typically separated by a few lattice constants. So the direct interaction between the localized Mn-spins is negligibly week, as it is depicted in Figure 2.2-4 a. Moreover, the direct interaction of Mn^{2+} ions is antiferromagnetic as it is known for the II-VI compounds[57] as well as compensated (Ga,Mn)As[62]. If a non-localized hole is present, it interacts with one localized Mn ion* and tends to be aligned opposite† to the Mn spin of that one ion due to the double-exchange interaction[67]. But due to the spatially extended nature of the hole, it interacts with more than one Mn ion at a time and this gives rise to the ferromagnetic alignment of the

* A strong hybridization of spin-polarized holes with Mn d levels is assumed to be the origin of a strong kinetic exchange coupling between the hole spins and Mn spins[66].

† The antiferromagnetic exchange coupling of Mn spin and valence band holes is widely accepted. Nevertheless it shall be noted that there are indications that a ferromagnetic interaction is possible [66]

localized Mn spins mediated by the free hole* as depicted in Figure 2.2-4 b. Due to the elevated hole density, because of the p-doping introduced by the Mn itself, the hole wave functions also overlap and mediate the exchange coupling even between distant Mn ions. This forms a stable ferromagnetic phase†. The magnetism is therefore originating from a complex of hole and Mn spins bound by exchange interaction. Speaking of energy bands, the long range order of the Mn spins mediated by the holes leads to spin-polarized energy bands[66].

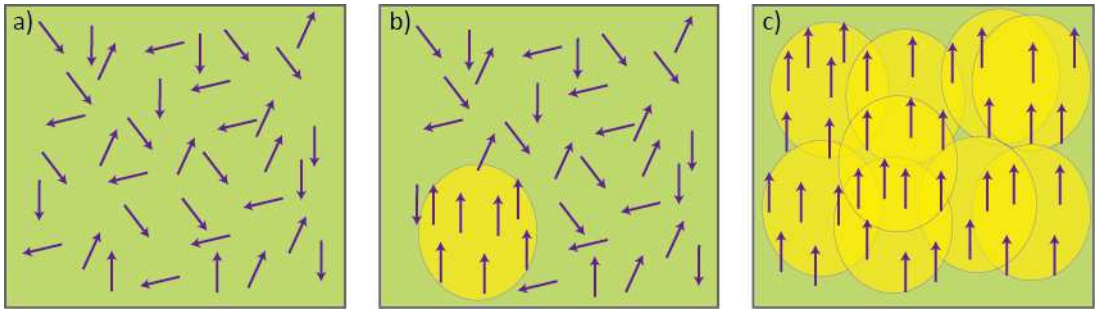

Figure 2.2-4: Illustration of the concept of carrier-mediated ferromagnetism: a) a random distribution of spins and no free carrier density, b) a free hole mediates a double-exchange coupling between neighboring spins that are within the radius of the spatially distributed free carrier, c) formation of a ferromagnetic phase is caused by overlap of holes and spins that lead to long range order[11]

Typical hole densities are about 10^{20} cm^{-3}, but differ of course depending on the Mn concentration and post growth treatment[65]. Also the number of Mn ions contributing to the ferromagnetic phase cannot be directly related to the Mn doping, because of the possible undesired interstitial positioning of Mn ions in the host lattice.

The carrier-mediated ferromagnetism is a very robust phenomenon in (Ga,Mn)As and Curie temperatures (T_Cs) up to 190 K[68] have been achieved so far‡. The magnetization of (Ga,Mn)As is rather weak and typical values of the magnetization are below $\mu_0 M$ = 100 mT[12].

As mentioned above the hole spins align opposite to the Mn spins. Therefore a part of the magnetic moments building the net magnetization is compensated by the opposite aligned hole spins. The magnetic system of (Ga,Mn)As is, strictly speaking, ferrimagnetic. The reduction of the overall magnetization is on the order of 10 %. This is only a microscopic detail. It does not change the macroscopic magnetic behavior of the system.

* This situation of low carrier concentrations may be realized by co-doping of (Ga,Mn)As to compensated the hole density (introduced by the acceptor Mn) to observe the formation of magnetic polarons[62].

† By appropriate co-doping spin glasses or frustrated phases may also be realized[62].

‡ Curie temperatures of 1000 K have been achieved for the related compound (Ga,Mn)N[69], although the origin of the ferromagnetism being carrier-mediated is not unambiguously proven yet. Curie temperatures of about 300 K have been realized for the ferromagnetic semiconductor (In,Mn)Sb[70].

Keeping the mediation of the long range order in mind, the problem of vanishing ferromagnetic order for Mn concentrations below 1 %[66] can be addressed: For very low Mn concentrations the distance between individual Mn ions gets larger, while the carrier concentration reduces due to the intrinsic p-doping of Mn and no ferromagnetic phase can be formed due to the vanishing overlap of the wave functions.

Theoretical details apart from this illustrative picture are not consistent and even often contradictory[58]. Significant parameters like overlap integrals and coupling constants differ in magnitude and also in sign, giving rise to the statement that the theoretical understanding of magnetism in DMS is far from complete, although great progress has been made by the critical analysis of theoretical frame works[63]. A mean-field model by Dietl et al.[71] based on the idea of hole mediated ferromagnetism and the incorporation of kp-band structure calculations gives a good agreement to experimental data and is widely accepted*.

2.2.3. Magnetic anisotropy

It is an experiment fact that a ferromagnet can be easier magnetized in one direction than the other. If the magnetic properties of a material are direction dependent, this fact is called magnetic anisotropy. If this anisotropy is caused by the crystal lattice it is called magneto-crystalline anisotropy (MCA)[3]. Although the magnetic anisotropy contributes only with the little amount of a few μev/atom to the energy of the material system compared to the eV/atom energies of atomic binding or the 100 meV/atom of stress[73], it has very big influence. There are only two microscopical origins for magnetic anisotropy[73]: On the one hand it is the long range dipol-dipol interaction sensing the outer shape of the structure and is therefore called the shape anisotropy[73]. On the other hand the spin-orbit coupling is of importance that couples the spin to the atomic orbitals forming the bonds of the crystal. Both interactions couple the spin of particles to the lattice. Due to their spherically symmetric wave functions, the Mn^{2+} ions itself do not contribute to the anisotropy[74]. The hole contribution to the magnetic system dominates the contributions to the magnetic anisotropy[58]. The effect of magnetic anisotropy is described in a phenomenological approach by noting the free energy of the system *F* as a function of the orientation of the magnetization vector $\vec{M}$ in space[75]. Depending on the actual symmetry, this leads to energetically favorable and unfavorable orientations of $\vec{M}$ called the easy axis

* Altough the magnetic properties of thin films of (Ga,Mn)As are very reproducible, when growth parameters are well defined, they are very sensible to these parameters on the other hand. (Ga,Mn)As as well as all DMSs in general show very rich physics as has been summarized in different reviews[11,57,62,72]. Due to the rich physics and sensitivity to growth parameters, care has to be taken by comparing experimental results with literature values. For this thesis, the details of the origin of ferromagnetism in (Ga,Mn)As are not nearly as important as the role of magnetic anisotropy.

and hard axis of magnetization, respectively. The easy and hard axes represent extremes of the free energy. The phenomenon of anisotropy is a big field and therefore the explanation will be restricted to a strained, single crystalline film of (Ga,Mn)As as it is investigated in the experiments presented in this thesis. The geometry considered is shown Figure 2.2-5.

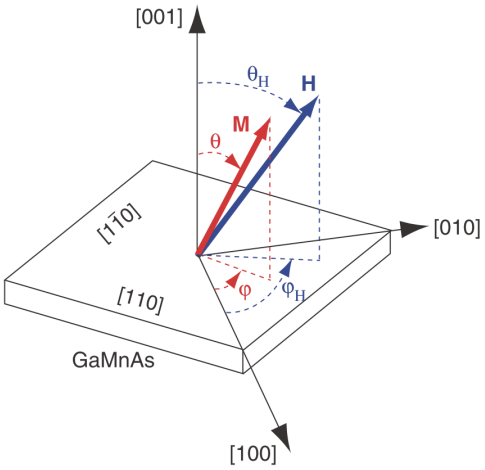

Figure 2.2-5: A model geometry for a thin layer of (Ga,Mn)As grown along the [100]-direction. The rotation in the (100)-plane is denoted with the polar angle φ and the rotation in the 100-direction with the azimuthal angle θ. These angles have to be separately noted for the external field $\vec{H}$ and the magnetization vector $\vec{M}$.[58]

The different effects that contribute to magnetic anisotropy are illustrated in Figure 2.2-6. The value of the free energy in this scheme is the length of the connection vector between the center of the body shown and the surface of the object.

If the material is a sphere made of a homogenous material without internal structure, there is no anisotropy as shown in Figure 2.2-6 a as the free energy in spherical form. However (Ga,Mn)As films are grown as single crystalline films and therefore have an intrinsic internal structure: the lattice structure. This gives rise to the magneto crystalline anisotropy of a cubic lattice as illustrated in Figure 2.2-6 b. The MCA leads to a favorable orientation of the magnetization along certain crystallographic directions. For a cubic crystal, these are the six equivalent high symmetry directions[58] oriented along the x-, y- and z-directions or the diagonal orientations depending on the MCA.

As (Ga,Mn)As is usually grown on a host lattice with different lattice constant, it exhibits uniaxial strain due to the lattice matched growth during LT-MBE[60]. This differentiates between the in-plane and out-of-plane high symmetry directions and distorts the system tetragonally (Figure 2.2-6 c)[65]. Depending on the sign of the strain either the four in-plane directions or the two out-of-plane directions are preferable leading to the orientation of spontaneous magnetization inside the layer plane or perpendicular to it. The strain changes the atomic orbitals and therefore redistributes the holes changing the MCA due to spin-orbit coupling[76].

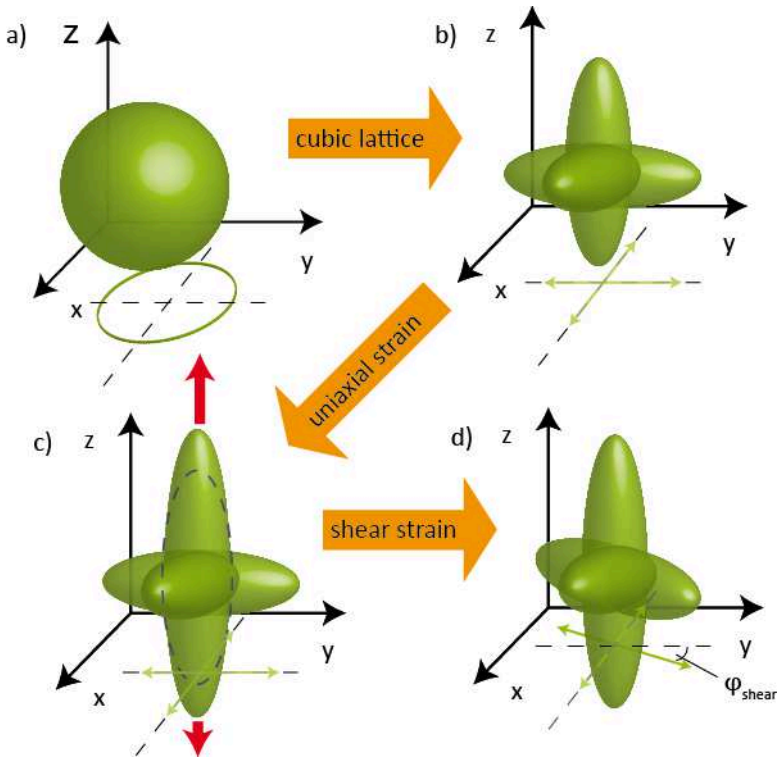

Figure 2.2-6: Illustration of the influence of different effects on the overall anisotropy of the free energy: a) The isotropic case of a sphere shaped free energy landscape, b) the cubic lattice incorporates extremes of the free energy along the main crystallographic directions and the diagonals, c) the effect of uniaxial strain due to the lattice matched growth breaks the 6-fold symmetry down to a 4-fold symmetry by changing the energy perpendicular to the magnetic layer and d) the phenomenological shear strain tilts the extremes of the free energy away from the crystallographically high-symmetry directions.

Further, it is an experimental fact, that the remaining four in-plane high-symmtery axes are not equal. A distortion of the MCA in form of an in-plane uniaxial anisotropy that can be modelled by a small built-in shear strain[74] tilts the energetically favorable directions away from the orthogonal geometry (Figure 2.2-6 d). The origin of this distortion of the MCA is not the Zink-blende symmetry itself and the origin of the distortion is subject of current research. Some surface reconstructions of the GaAs substrate seems to be incorporated[65] and has been observed for other materials with similar growth processes. Using the notation of the geometrical situation shown in Figure 2.2-5, the free energy F can be expressed* by[58]

* This formulation of the free energy is valid in the Stoner-Wolfrath model, where the magnetic layer is assumed to behave like a single, homogenous magnetic domain. However the validity of this model for the samples considered in the experiments is based on experimental findings[77].

$$F = \underbrace{-MH\left[\cos\theta\cos\theta_H + \sin\theta\sin\theta_H\cos\left(\varphi-\varphi_H\right)\right]}_{\text{Zeeman Energy}}$$

$$\underbrace{+2\pi M^2\cos^2\theta}_{\text{Shape}} \underbrace{-\frac{1}{2}MH_{2\perp}\cos^2\theta}_{\text{uniaxial perpendicular}} \underbrace{-\frac{1}{4}MH_{4\perp}\cos^4\theta}_{\text{cubic perpendicular}} -$$

$$\underbrace{\frac{1}{16}MH_{4\parallel}\left(3+\cos 4\varphi\right)\sin^4\theta}_{\text{planar cubic}} \underbrace{-\frac{1}{2}MH_{2\parallel}\sin^2\theta\sin^2\left(\varphi-\frac{\pi}{4}\right)}_{\text{planar uniaxial}} \qquad (2.2.2)$$

with the magnetization M and the external magnetic field H with corresponding polar angles φ and φ_H and azimuthal angles θ and θ_H. The first term gives the Zeeman contribution to the anisotropy. It describes the potential energy of a dipole in an external magnetic field. The second term of equation (2.2.2) describes the shape anisotropy of a thin film. The parameters $H_{2\parallel}$ and $H_{4\parallel}$ represent the planar uniaxial and planar cubic anisotropy fields, respectively. The parameters $H_{2\perp}$ and $H_{4\perp}$ represent the perpendicular uniaxial and perpendicular cubic anisotropy fields. Due to the magnetic anisotropy fields, the magnetization is not necessarily parallel to the external magnetic field. The effect of the "internal" anisotropy fields and the externally applied magnetic field can be combined in an effective field B_{eff}[75]. The effective field is related to the free energy by the gradient with respect to the magnetization direction

$$\vec{B}_{eff} = -\frac{\partial F}{\partial \vec{M}}. \qquad (2.2.3)$$

Changing the sphere to a thin film, shape anisotropy becomes important. The shape anisotropy describes the fact that the outer geometry can determine magnetic order. For example, it is experimentally well known that a steel rod is much easier to be magnetized along its cylindrical axis than perpendicular. However, for (Ga,Mn)As the shape anisotropy is not of great importance as the overall magnetization is rather weak[12].

Further, the anisotropy can be effectively manipulated by a change in the hole concentration, which is easy to understand as the holes mediate the magnetic order[52]. Also the temperature is of significant importance as experimentally changes of the easy axis have been observed at around $T_C/2$[64].

(Ga,Mn)As is a material with a very pronounced MCA. Typical values are in the range of a few hundred mT, but can be reduced by post-growth annealing significantly[58] and vary with the sample temperature. Therefore, saturation fields of a few hundred mT are sufficient to magnetize the medium completely.

Considering the planar und perpendicular uniaxial anisotropy, it shall be pointed out that these two are originating from the in-built strain during growth only. For a broad range of growth parameters the in-built strain is the key and therefore dominating parameter to determine the easy magnetization axis[65]. Further it is observed that by the mechanical application of uniaxial strain, T_c can be increased by roughly 25%. A static strain of 1 % can change the MCA energy landscape completely[78]. These are demonstrations that in the static case the anisotropy of (Ga,Mn)As and even the magnetic order itself is strongly influenced by the strain conditions. The effect of the strain on the magnetic anisotropy can be included in equation (2.2.2) by a linear dependence of the anisotropy fields on the strain amplitude[79].

3. Experimental techniques and setup

„The beginning of sciences is the astonishment that all things are the way they are“

Aristoteles

In order to study the desired interaction of picosecond strain pulses and a thin layer of a ferromagnetic material an experiment has to be designed to realize this interaction. This is described in this chapter. It starts with a sketch of the experimental setup that provides the laser pulses needed for excitation and a detection scheme. The optical detection of the strain and the magnetization state of the sample is described in the following two sections.

3.1. Experimental setup

The experimental setup to realize the strain induced precession of magnetization and the monitoring of the magnetization dynamics is sketched in Figure 3.1-1. The setup is based on three main building blocks.

The first key element is the laser system. To realize the excitation of picosecond strain pulses as described in chapter 2.1.2, laser pulses with pulse energies of about 1 µJ and sub-picosecond durations are needed. This pulses are realized by utilizing a continuous wave Nd:YVO_4 pump laser [Coherent Verdi V12] that emits light at 532 nm with an optical power of 12 W. This optical pump provides the energy that is used by a regenerative amplifier [Coherent Rega9000] to amplify the pulses of the seed laser [Coherent Vitesse]. The seed laser emits laser pulses with a wavelength of 800 nm and pulse duration of 200 fs at a repetition rate of 80 MHz. Each pulse of the seed laser has an energy on the order of 1 nJ. Passing the regenerative amplifier, the pulse is amplified to have an energy of a few µJ. This is realized by passing of a Ti:Sapphire crystal inside the regenerative amplifier that is pumped by the continuous wave laser. The output beam has a repetition rate of 100 kHz. The optical pulses have a Gaussian temporal profile and the radial intensity distribution of the laser beam is Gaussian as well. The main part of the laser beam passes a beam splitter (BS) and is used for the excitation of the strain pulse (pump beam). The laser amplitude for

the initial strain pulse generation can be adjusted by a gradient filter (GF). The weaker part of the laser is reflected by the beam splitter and is used for the optical probing (probe beam).

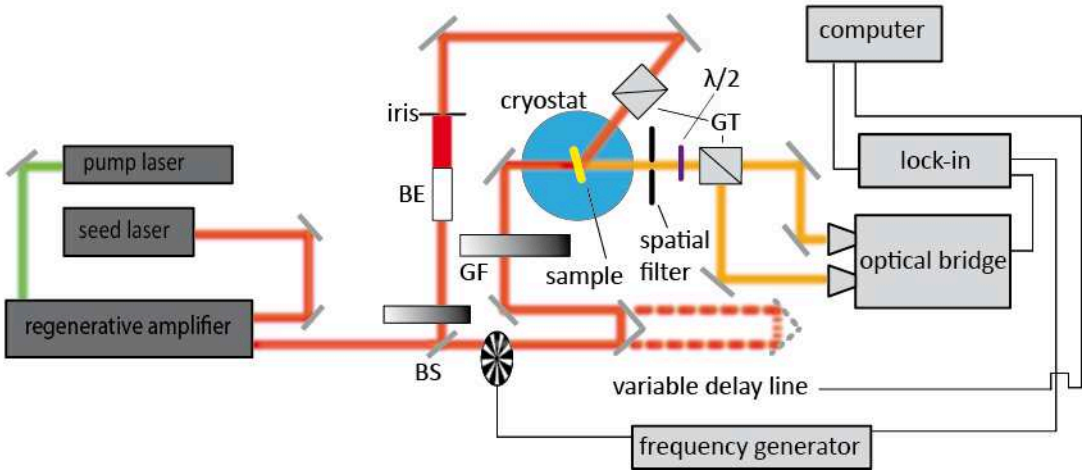

Figure 3.1-1: Scetch of the experimental setup to optical excite picosecond strain pulses and to monitor the induced dynamics of the magnetization of a thin ferromagnetic film optically.

The second building block is a cryostat [Oxford Spectromag 10 T] that allows for cooling the sample down to 1.2 K by liquid helium and the application of dc magnetic fields up to 10 T by a superconducting magnet. Working at high pump densities leads to bubbling of the liquid helium. Therefore the experiments are performed in vapour helium at 6 K for high excitation densities. . It is possible to estimate the initial strain pulse amplitude η_0 by

$$\eta_0 = kW \tag{3.1.1}$$

with the laser density W and the conversion coefficient $k \approx 10^{-4}$ cm^2/mJ[80]. Typical excitation density destruction threshold limits for 100 nm aluminum films grown on GaAs are on the order of 10 – 15 mJ/cm^2. The inside of the cryostat is optical accessible by optical windows on each side of the cryostat. In the variable temperature inset (VTI) of the cryostat the sample is strain* free mounted on a sample holder that allows for rotation around the optical axis as well as adjusting the plane of the sample. As the strain pulse travels with sound velocity through the GaAs substrate, the probe pulse has to be optically delayed for the traveling time of the strain pulse through the layer to achieve temporal overlap. This ensures that the dynamics inside the layer induced by the strain pulse are detected by the probe. The probe pulse is directed onto the sample by a small lens to ensure a nearly zero incidence angle. Before hitting the sample the linear polarization plane can be defined and adjusted by the use of a Glan-Thompson prism (GT) that works as

* A strain free mount is necessary to avoid additional, unpredictable straining of the sample during cool down from room temperature by the different expansion coefficients of the sample mount and the sample itself.

a polarizer for the incident laser beam. After reflection from the sample the probe is collected by an imaging lens that images the sample onto a cross slit, which acts as a spatial filter to cut stray light.

The third building block of the setup is the optical detection and data acquisition. The probe beam leaving the spatial filter is incident on an optical bridge detection system. First another retarder plate is implemented to rotate the polarization plane of the probe beam to use the following GT to split the probe beam in equal parts. The splitting of linear polarized light with initial intensity I_0 by a polarizer is described by *Malus' Law*[81] for the transmitted part

(3.1.2) $$I_T = I_0 \cos^2 \beta$$

and reflected part

(3.1.3) $$I_R = I_0 \sin^2 \beta .$$

The angle β is spanned between the incident polarization plane of the light and the axis of the polarizer.

The two beams leaving the GT are adjusted to a pair of photodiodes that produce an output proportional to the difference between the intensities of the two beams [New Focus, Nirvana2007]. In static conditions without perturbation, the optical bridge is balanced by the retarder plate setting the recorded signal for a given polarization to zero. If a perturbation changes the plane of polarization of the probe light, the intensities of the beams split by the GT are not equal anymore. This gives rise to a voltage proportional to the difference of the intensities of the beams from the balanced photo receiver. A mechanical chopper [Stanford Research Instruments, Model SR540 Chopper] modulates the pump beam and the difference in the angle of polarization rotation $\Delta\Phi(t) = \Phi(t) - \Phi_0$ is measured by the bridge photo detection (Φ_0 is the polarization rotation angle without strain pulse).

If the whole intensity of the probe beam is forwared to one silicon diode and the other diode is blocked, the modulation of intensity of the probe light can be monitored. To increase the signal-to-noise ratio a lock-in amplifier [Signal Recovery, Model 7225] is used. This device gives an output proportional to the voltage of the balance photo receiver at a certain frequency. The pump beam is modulated by the mechanical chopper and the lock-in amplifier is locked to this frequency. This configuration ensures that signal components at other frequencies than the chopper frequency are strongly suppressed. The temporal

resolution of this setup is on the order of 0.5 ps. This resolution is achieved by the pump-probe detection scheme described above that is mainly limited by the laser pulse duration and the accuracy of the control of the temporal delay between the pump and probe pulses. The temporal resolution in this setup is realized with a computer controlled mechanical delay line [Aerotech, ATS-125] that allows for a detection time window* of roughly 4 ns and a reproducible step size of 0.5 ps. The data acquisition is done by computer that controls the optical delay line and reads the data from the lock-in amplifier.

3.2. Optical detection of acoustic pulses

To be able to detect strain by optical means, an interaction between light and strain in a solid medium has to exist. This coupling is called the acousto-optic effect. It describes the fact that strain changes the optical constants of the material[33] for the real

(3.3.1) $$\Delta n = \frac{\partial n}{\partial \eta}\eta$$

and the imaginary part

(3.3.2) $$\Delta \kappa = \frac{\partial \kappa}{\partial \eta}\eta .$$

The change Δn of the real part n of the complex index of refraction and the imaginary part κ and its change $\Delta\kappa$ are related to the dielectric constant ε of a material by

(3.3.3) $$\varepsilon = \left(n + i\kappa\right)^2 .$$

In other words, the strain modulates the dielectric constant of the material†. The interaction of strain with the probe light is measured in reflection geometry and therefore the change of reflectivity of the sample induced by the strain has to be described. This is done by solving Maxwell's equation inside the film with spatial variation $\Delta\varepsilon$ induced by the strain [33]

(3.3.4) $$\frac{\partial^2 E}{\partial z^2} = -\frac{\omega^2}{c^2}\left[\varepsilon + \Delta\varepsilon\left(z,t\right)\right]E$$

* The time window is determined by the length of the computer controlled delay line and the time resolution by the reproducibility limits of the control electronics.

† For simplicity a homogenous, isotropic medium is considered as the dielectric constant is a tensor in the general case.

with the light frequency ω and the speed of light c. This equation is valid for a plane wave light field E incident in z-direction with zero incidence angle in accordance with the experimental geometry. And if the excitation involves a longitudinal acoustic pulse (see equation (2.1.15)), the strain has only zz-components. The situation for a δ-function strain is depicted in Figure 3.2-1.

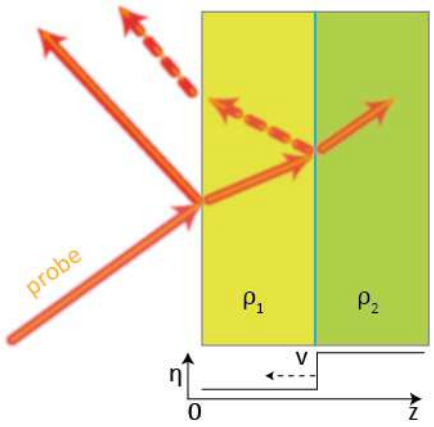

Figure 3.2-1: Illustration of the reflection of a probe light wave from the interface of the substrate material and from an interface in the substrate induced by the step-function-like discontinuity of the strain moving with the sound velocity v[82]. The strain leads to two different densities ρ_1 and ρ_2 that lead to different optical properties.

A part of the wave is reflected at the interface of the medium due to difference in the refractive index of the surrounding atmosphere and the medium and another part is reflected at the disturbance introduced by the strain. These two contributions are able to interfere. This interference changes as the strain pulse moves through the medium and therefore alters the path difference between the two reflections. This leads to a change of the reflectivity ΔR measured in the pump-probe experiments of the form[33]

$$\Delta R \sim \cos\left(\frac{4\pi n v t}{\lambda} - \delta\right) e^{-z/\xi} \tag{3.3.5}$$

with the probe wavelength λ, the probe penetration depth ξ and a phase shift δ. Therefore the frequency of oscillations f, called the Brillouin* frequency, is determined by

$$f = \frac{2nv}{\lambda}. \tag{3.3.6}$$

The exponential damping of the detected change in the reflectivity is related to the finite penetration depth of the probe light into the medium. The result (3.3.5) only holds, if the acoustic attenuation is not significant in the probe penetration depth. But this

* This is the well-known frequency of conventional Brillouin scattering experiments. But unlike conventional Brillouin scattering, which describes interaction of light with incoherent, thermal phonons, this type of Brillouin scattering describes scattering with coherent phonons and allows for measurements of the sound velocity and attenuation at a single frequency[83].

assumption is valid as the traveling distance of 100 µm through the GaAs substrate in the experiment is typically much bigger than the light penetration depth of a few hundreds of nm for the probe light. Otherwise no strain could be detected, as it would not be able to pass the substrate. The situation in the experiment is not a δ-functional change of the strain, but a more complicated waveform for the strain. Nevertheless the formulas still describe the experimental data very well.

3.3. Magneto-optical effects

The main goal of this work is to investigate the effect of a picosecond strain pulse on a thin ferromagnetic layer and to determine the evolution of the magnetization dynamics all-optically. The effect that describes the interaction of light reflected from a magnetized surface is called the magneto-optical Kerr effect. It describes the observed rotation of the polarization plane of linearly polarized light reflected by a magnetized surface.

In general the description of the effects acting on the polarization state of light in crystalline matter is cumbersome for an arbitrary geometry[*]. One has to start from Maxwell's equations in matter with appropriate boundary conditions to come to the Fresnel equation (3.4.1) to determine the eigenmodes of the light allowed in the crystal[85]:

$$\left(n^2 - \frac{\widetilde{\mu_r}\widetilde{\varepsilon_r}}{\mu_0\varepsilon_0}\right)\vec{E} - \vec{n}\left(\vec{n}\cdot\vec{E}\right) = 0\,. \tag{3.4.1}$$

The electric field is denoted by *E*, the refractive index/vector by *n*, the vacuum and matter permittivity tensor μ_0 and $\widetilde{\mu_r}$ and the vacuum and matter permeability of the medium ε_0 and $\widetilde{\varepsilon_r}$. The dielectric tensor $\tilde{\varepsilon}$ depends on the external fields in general. In the limit of $\mu_r \rightarrow 1$ it is possible to describe the effects to lowest order in the applied fields as following[86]

$$\varepsilon\left(\vec{k},\omega,\vec{B},\vec{E}\right) \approx \varepsilon_0 + \underbrace{O\left(\vec{k}\right)}_{NAO} + \underbrace{O\left(\vec{B}\right)}_{odd\ MO} + \underbrace{O\left(\vec{E}\right)}_{EO} + \underbrace{O\left(\vec{E}\vec{B}\right)}_{MEO} + \underbrace{O\left(\vec{B}\vec{B}\right)}_{even\ MO} + \ldots \tag{3.4.2}$$

with the natural optical activity (NAO), the odd and even magneto-optical effects (MO) and the electro-optical (EO) and magneto-electric effects (MEO), respectively. These effects depend on the orientation of the externally applied magnetic and electric fields and the symmetry of the crystal. Therefore, only certain eigenmodes exist for different

[*] This is the reason why Jones[84] invented his famous matrix formalism.

geometries. As an example for a relevant geometry in the experiments, a cubic crystal with a magnetic field applied along the z-direction is considered. This leads to the following dielectric tensor[85]

$$\tilde{\varepsilon} = \begin{pmatrix} \varepsilon_x & \varepsilon_{xy} & 0 \\ -\varepsilon_{xy} & \varepsilon_x & 0 \\ 0 & 0 & \varepsilon_z \end{pmatrix} = \begin{pmatrix} \varepsilon_x & -ig & 0 \\ ig & \varepsilon_x & 0 \\ 0 & 0 & \varepsilon_z \end{pmatrix} \tag{3.4.3}$$

with the off-diagonal elements ε_{xy} arising from the magneto-optical interaction or the alternative formulation with the gyration vector g. Only the asymmetric parts of the tensor are responsible for the optical effects. All parameters in (3.4.3) are complex numbers in general to incorporate information about absorption effects. The microscopic origin of the diagonal elements in the case of magneto-optical effects is the spin-orbit coupling.

The eigenmodes of the system described in (3.4.3) for a polar geometry with a light field propagating in z-direction are circularly polarized electro-magnetic waves that have different refractive indices for right- and left-hand polarized waves

$$n_{\pm} = n_{0\pm} + i n_{1\pm} \tag{3.4.4}$$

with different real n_0 and imaginary n_1 parts for right- and left-hand polarized waves. If linearly polarized light traverses the magnetized medium the difference in the real parts lead to magnetic-field-induced circular birefringence (MCB) and the differences in the imaginary parts lead to magnetic-field-induced circular dichroism (MCD) also known as the Faraday Effect. These two effects are odd in magnetization.

When the light traverses a transversely magnetized medium (magnetization or applied field along x- or y-direction and light propagation along z-direction) the allowed eigenmodes are linearly polarized waves:

$$n_{\perp/\parallel} = n_{0\perp/\parallel} + i n_{1\perp/\parallel}\,. \tag{3.4.5}$$

The corresponding real and imaginary parts of the refractive indices are denoted as $n_{\parallel}$ for parallel and $n_{\perp}$ for perpendicular polarization with respect to the magnetic field direction. The differences in the real part of the refractive index for different polarization directions is the reason for the magnetic field induced linear birefringence (MLB) and the difference in the imaginary part lead to magnetic field induced linear dichroism (MLD). Both effects are even in magnetization. For an arbitrary direction of the magnetization and

the light propagation all of these effects are mixed and lead to elliptically polarized electromagnetic waves in general.

The magneto-optical Kerr effect does not describe the transmission of light through a magnetized medium, but the reflection of light from its surface. Three geometries are considered in this case, as depicted in Figure 3.3-1.

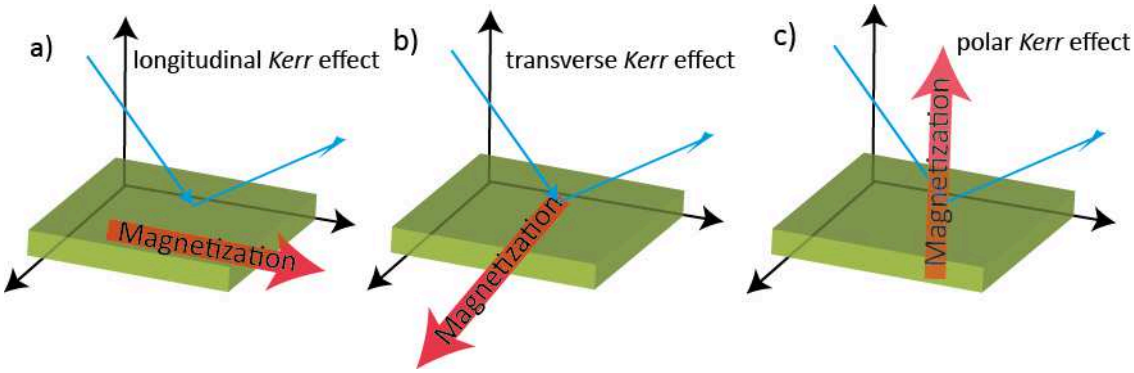

Figure 3.3-1: Different geometries for the magneto-optical *Kerr* effect. When the magnetization is in the plane spanned by the incident and reflected optical beam and perpendicular to the surface the effect (a) is called the longitudinal *Kerr* effect. b) If the magnetization is perpendicular to the optical plane and perpendicular to the surface normal the effect is the transverse *Kerr* effect. c) If the magnetization is inside the optical plane, but parallel to the sample surface it is the polar *Kerr* effect.

If linearly polarized light is reflected from the surface of a material and the magnetization is parallel to the surface normal, this is called the polar *Kerr* effect. If the magnetization is perpendicular to surface normal, but lies in the layer plane of the reflected light, the effect is called the longitudinal *Kerr* effect. The longitudinal and polar *Kerr* effects form the group of longitudinal optical effects. Both lead to a rotation of the polarization plane as well as an ellipticity of the light. It is called the transverse *Kerr* effect, if the magnetization lies perpendicular to the surface normal and perpendicular to the plane of light reflection[*]. All *Kerr* effects are odd functions of the magnetization, and therefore a sign change in the external applied field leads to a sign change in the experimentally measured signals.

For typical ferromagnetic materials like Ni or iron, polar Kerr angles of less than 1° are observed. The transverse effect is on the order of 0.01° or less. Thus, it is typically a small effect. (Ga,Mn)As however shows a giant Kerr effect of a few degrees.

[*] It is only present in absorbing media and only present for p-polarized incident waves in the limit $\mu_r \rightarrow 1$. The approximation of $\mu_r \rightarrow 1$ can therefore be tested with s-polarized light, because for the effect on s-polarized light the material permittivity is responsible[85].

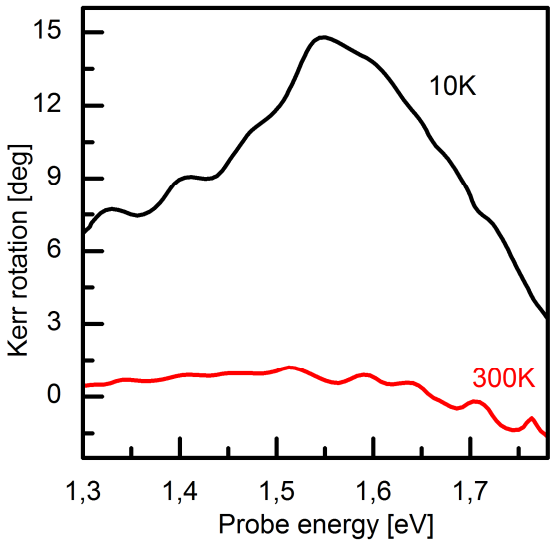

Figure 3.3-2: Model optical *Kerr* spectrum of a 2 µm thick (Ga,Mn)As layer with a Mn content of 4.3 % measured at an applied field of 6 T and a temperature of 10 K (ferromagnetic) showing a giant Kerr effect. The same structure at 300 K (paramagnetic) shows a significant less *Kerr* rotation[62].

The giant Kerr effect makes it a great tool investigate the magnetization state of (Ga,Mn)As. The use of the Kerr effect is not limited to the investigation of the static magnetization, but can be used to monitor magnetization dynamics as well. For the reflection of light from a magnetized medium with zero incidence angle the polar Kerr effect rotates the polarization of light proportional to the magnetization component perpendicular to the magnetic layer, whereas the longitudinal Kerr effect is negligible in this geometry[85].

4. Coherent magnetization precession in ferromagnetic (Ga,Mn)As induced by picosecond strain pulses

„In Wahrheit heißt etwas wollen, ein Experiment machen, um zu erfahren, was wir können.“

Friedrich Nietzsche

As pointed out in section 2.2.3, the appropriate choice of the substrate material controls the growth induced strain that in turn determines the orientation of the direction of the spontaneous magnetization. The idea of applying picosecond strain pulses to a layer of (Ga,Mn)As and the resulting change in the strain conditions leads to the possibility of dynamic control of the magnetization orientation by the strain pulse. This chapter describes the first successful experimental realization of the induction of magnetization dynamics via ultrafast acoustics.

There are techniques established to induce magnetization dynamics or realize magnetic switching by electric fields, magnetic field pulses or optical excitation[76]. Nevertheless, these techniques have significant side effects like direct heating of the magnetic material and the generation of high concentrations of non-equilibrium carriers or they are limited to relatively low frequency bandwidths. The utilizing of strain pulses to induce magnetization dynamics avoids many of these side effects and may therefore push the development of functional DMS devices further. No carriers are generated by strain pulses. Virtually no acoustic energy remains inside the magnetic layer after the pulse has left*. And the pulse itself can travel over millimeter distances, allowing for the spatial separation of strain pulse excitation and the magnetic material. In this case no thermal energy is transferred to the magnet that may heat it above the Curie temperature, which would finally lead to the destruction of the magnetic order. Furthermore, acoustic

* Although the strain has no long lasting impact, a heat pulse generated by the use of the technique of picosecond acoustics can last for a much longer time.

frequencies are easily generated in the hundreds of GHz reaching up to THz frequencies allowing for ultrafast manipulations*.

4.1. Sample characterization

A strain pulse has to be generated and delivered to the magnetic layer. The corresponding scheme is depicted in Figure 4.1-1. The sample with the identification number *50532A* is emerged in superfluid helium at a temperature of T = 1.6 K, while the magnetic field is applied along the z-direction, parallel to the hard axis of magnetization and perpendicular to the sample surface. The GaAs substrate was polished down to 100 µm and a 100 nm thick aluminum transducer was evaporated on the substrate. The energy density of the pump incident on the aluminum film per pulse is 2 mJ/cm^2 (300 µm spot diameter estimated by the full-width at half maximum of the Gaussian beam profile)† that leads to a longitudinal strain amplitude of about $\eta_{zz} = 10^{-4}$. The strain pulse travels through the 100 µm GaAs substrate at a longitudinal sound velocity of v = 4730 m/s[88]. This takes 21.1 ns until the strain pulse reaches the (Ga,Mn)As layer. The (Ga,Mn)As layer was deposited by LT-MBE by the group of J. Furdyna from the university of Notre Dame in the USA. The strain and the magnetization component $M_z = M \cdot \cos(\theta)$ parallel to the external field can be sensed by the probe beam split from the same laser with an energy density per pulse of 10 µJ/cm^2 reflected under near zero reflection angle from the sample. The probe spot diameter is 150 µm to ensure probing a homogenously excited area of the sample.

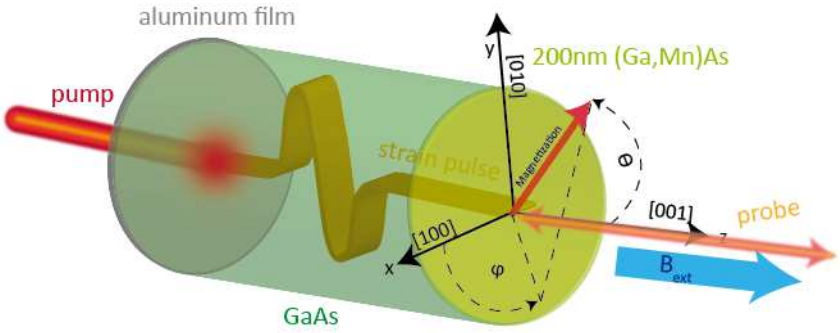

Figure 4.1-1: Scheme of the sample structure and experimental geometry. The magnetization direction is defined by the polar angle θ and the azimuthal angle φ with regard to the [001]- and [100]-direction, respectively.

* Although magnetic switching in Co-bars have been demonstrated by surface acoustic waves, these techniques are limited to a few GHz due to the use of piezo-transducers for the surface acoustic wave generation[87].

† It is hardly possible to increase the energy density further due to the formation of a He bubble at the other side of the sample that is formed at the sample surface and leads to strong scattering of the probe beam.

The sample consists of a *d* = 200nm (Ga,Mn)As film grown by low temperature molecular beam epitaxy on a semi-insulating (100)-GaAs substrate*. The manganese concentration is 5 % and due to the intrinsic p-doping a more metallic-like character of the layer can be expected[71]. Originating from the lattice matched growth conditions, the (Ga,Mn)As film is under compressive strain and X-ray diffraction measurements reveal an in-plane compressive strain of $-2\cdot10^{-3}$ and an out-of-plane tensile† strain of $1.9\cdot10^{-3}$. The compressive strain leads to the orientation of the easy magnetization axis in the layer plane. The [001]-direction is the hard magnetization axis. Superconducting quantum interference device (SQUID) magnetometry reveals a saturation magnetization of $\mu_0\cdot M_s$ = 25 mT and a Curie temperature‡ of T_C = 60 K.

The magnetic field dependence of the stationary Kerr angle is shown in Figure 4.1-2. The observed curve is typical for (Ga,Mn)As layers with an external magnetic field applied along the hard axis of magnetization[89]. The dips observed around ±120 mT are artifacts not related to the sample magnetization, but can be attributed to optical interference effects[89].

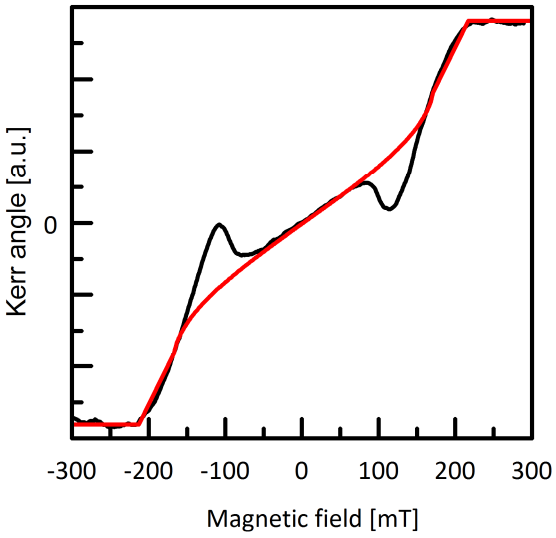

Figure 4.1-2: The magnetic field dependence of the stationary Kerr angle at a temperature of 1.6 K and a probe wavelength of 800 nm. The measured curve (black) is fitted (red) with a single domain model according to ref[90].

Aside these interference effects, the curve can be analyzed with an approach of minimizing the free energy of the system with respect to θ as in Figure 2.2-5 according to the procedure described in Ref. [90]. By applying the geometrical restrictions to equation (2.2.2), it can be simplified to

* The sample was grown by the group of Jacek K. Furdyna and Xinyu Liu from the Physics department of the Notre Dame University in the USA.

† Compared to the elastic moduli these strain values correspond to externally applied static pressures in the GPa-region

‡ Both characterizations were done by the group of Furdyna and Liu.

(4.2.1)

$$F = \tfrac{1}{2} M \left[-2B\cos\theta + \left(\underbrace{4\pi M - H_{2\perp}}_{4\pi M_{eff}} + \tfrac{1}{2} H_{2\|} \right) \cos^2\theta - \tfrac{1}{2}\left(H_{4\perp}\cos^4\theta + H_{4\|}\sin^4\theta \right) \right].$$

Utilizing the standard conditions for a minimum of the free energy $\frac{dF}{d\theta} = 0$ and $\frac{d^2F}{d\theta^2} > 0$, it is possible to determine the local and global minima for each applied field H. One minimum occurs at θ = 90° corresponding to the easy axis magnetization that is the global minimum for low fields. The other minimum corresponds to the parallel orientation of the magnetization with the external field (θ = 0°) that is the global minimum for high fields. For small fields, M_z increases monotonically with increasing field with the rate

(4.2.2)
$$\frac{dM_z}{dH} = \frac{M}{4\pi M_{eff} + \frac{1}{2}H_{2\|} + H_{4\|}}.$$

For increasing fields, the magnetization shifts towards θ = 0 and at the field B_{N2} the two minima interchange their character of being the global minimum so that the magnetization snaps to coincide with the external field and shows the saturation value:

(4.2.3)
$$B_{N2} = \frac{2\sqrt{3}}{9}\left(H_{4\perp} + H_{4\|} \right) \left(\frac{4\pi M_{eff} + \frac{1}{2}H_{2\|} + H_{4\|}}{H_{4\perp} + H_{4\|}} \right)^{3/2}.$$

Together with the fitting of the energy minima, this allows the anisotropy constants to be determined[91] to $\left(4\pi M_{eff} + H_{2\perp}\right)\mu_0 = 182mT$, $\mu_0 H_{4\perp} = 66mT$, $\mu_0 H_{2\|} = 0mT$ and $\mu_0 H_{4\|} = 197mT$ *. The values agree well with literature values for similar structures[90].

* The model used has some typical shortcomings of theoretical models like not including domain wall energies, T = 0 K etc. This leads to further unambiguity in the values obtained from the measured data, which is further confirmed by the not perfect, but still rather good fit of the model to the data.

4.2. The concept of strain induced magnetization precession

As mentioned earlier the growth induced strain of the (Ga,Mn)As layer determines the orientation of the direction of magnetization[62,65]. This sensitivity of the direction of magnetization to the static strain conditions* motivates the attempt to induce magnetization dynamics by the application of time varying strains utilizing the methods of picosecond acoustics as discussed in chapter 2.1.

The basic physical picture is drawn in Figure 4.2-1. The external field along the hard axis of magnetization and the contributions of the effect of magnetic anisotropy sum up to an effective field B_{eff}. The magnetization is oriented parallel to this effective field under static conditions. The orientation of the magnetization of the sample is thus determined by the balance of the external applied magnetic field and the effects of anisotropy.

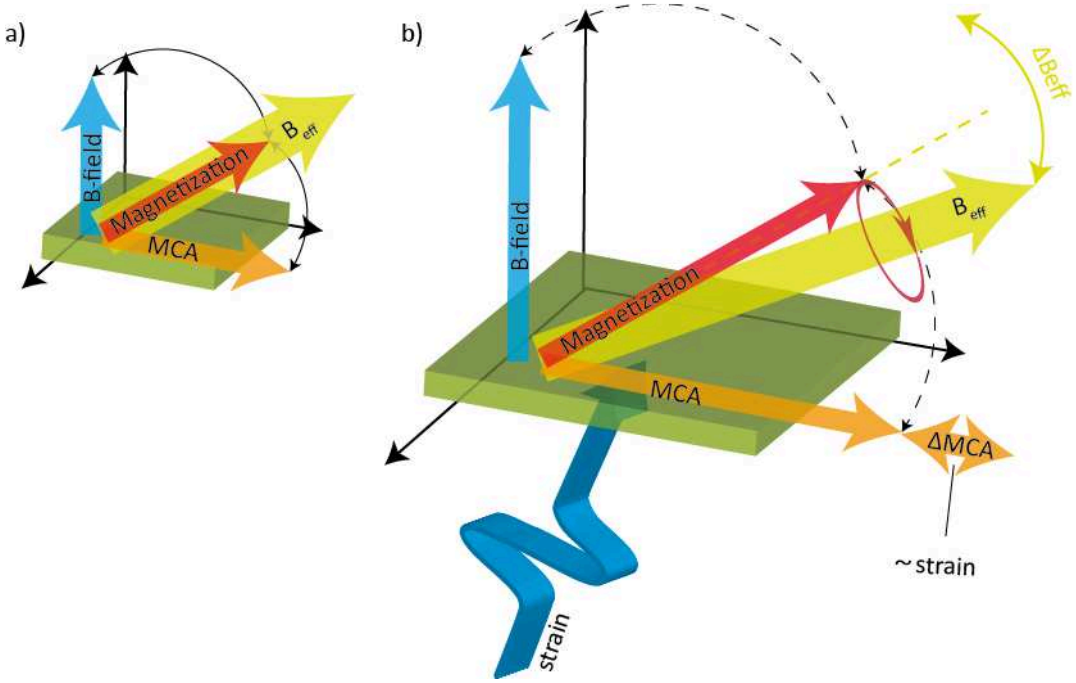

Figure 4.2-1: Schematic illustration of the experimental concept: a) By application of an external field of medium strength perpendicular to the magnetic layer plane the orientation of the magnetization is determined by the balancing between the external magnetic field and the anisotropy field. b) When the strain pulse hits the magnetic layer the MCA is changed proportional to the strain. This changes the balancing of the MCA and the external field leading to a tilt of the effective field B_{eff}.

The external field is kept constant in the following and a picosecond strain pulse is launched into the magnetic film. For simplicity, the strain pulse shall be a step function. This strain pulse changes the magnetic anisotropy of the film, when it hits the film and thus modulates the effective field. If the effective field changes, the magnetization does not

* By the application of static strains by piezo-electric transducers switching behavior is already been observed in the static case[92]

immediately follow this change. The magnetization will start to precess around the new direction of the effective field and finally reaches this new position by a damped oscillation. This damped oscillation of the magnetization is described by the Landau-Lifshitz-Gilbert equation[73]

$$\frac{\partial \vec{M}}{\partial t} = -\gamma\left(\vec{M} \times \vec{B_{eff}}\right) + \frac{G}{\gamma M^2}\left(\vec{M} \times \frac{\partial \vec{M}}{\partial t}\right) \qquad (4.2.4)$$

with the Gilbert damping coefficient G and the gyromagnetic ratio $\gamma = g\mu_B/\hbar$ composed of the Bohr magneton μ_B, the g-factor g for the Mn-spin in (Ga,Mn)As and the reduced Planck constant $\hbar$. This is the '*equation of motion*' of magnetism. It is assumed that the precession angles are small and that the overall magnetization amplitude is not changed by the strain.

The demonstration of the basic principle by imagining a step function is intuitive to understand, but it has some shortcomings: In the case of a step-function-like strain pulse, the final state will be different from the initial one, because the strain pulse lasts forever. A real strain pulse has a finite duration and will leave the film with no aftermath. The strain will therefore change the direction of the effective field continuously and finally the effective field will be in the initial configuration again. The magnetization is precessing around a changing magnetic field direction, which makes the trajectory more complicated. Another consequence of the finite strain pulse is the spatial non-uniform excitation of the magnetization that may lead to a spatial dependence of the magnetization dynamics.

4.3. First demonstration of strain induced magnetization precession

The influence of the strain pulse on the rotation of the polarization is monitored in reflection geometry sensing the magnetization component perpendicular to the magnetic layer M_z. A representative curve is shown in Figure 4.3-1 for an external magnetic field of 80 mT.

The arrival time of the strain pulse at the magnetic layer corresponds to $t = 0$ ps. The oscillations at $t < 0$ ps (section I in Figure 4.3-1) correspond to Brillouin oscillations (see chapter 3.2) at a frequency of 44 GHz that correspond well to the theoretical prediction for GaAs with a longitudinal speed of sound of 4730 m/s[88] and a probe wavelength of 800 nm at nearly zero incidence angle. Although Brillouin oscillations are usually visible as an intensity modulation, the magnetic fields make them visible as polarization changes due to the circular dichroism of the paramagnetic GaAs substrate[50]. Therefore they cannot be detected without the externally applied field (see Figure 4.3-4). They are also clearly visible

in a wider time interval of t > 125 ps for magnetic fields higher than 100 mT. In this time interval the Brillouin oscillations originate from the strain pulse that does not travel towards the magnetic layer, but away from the layer back into the substrate.

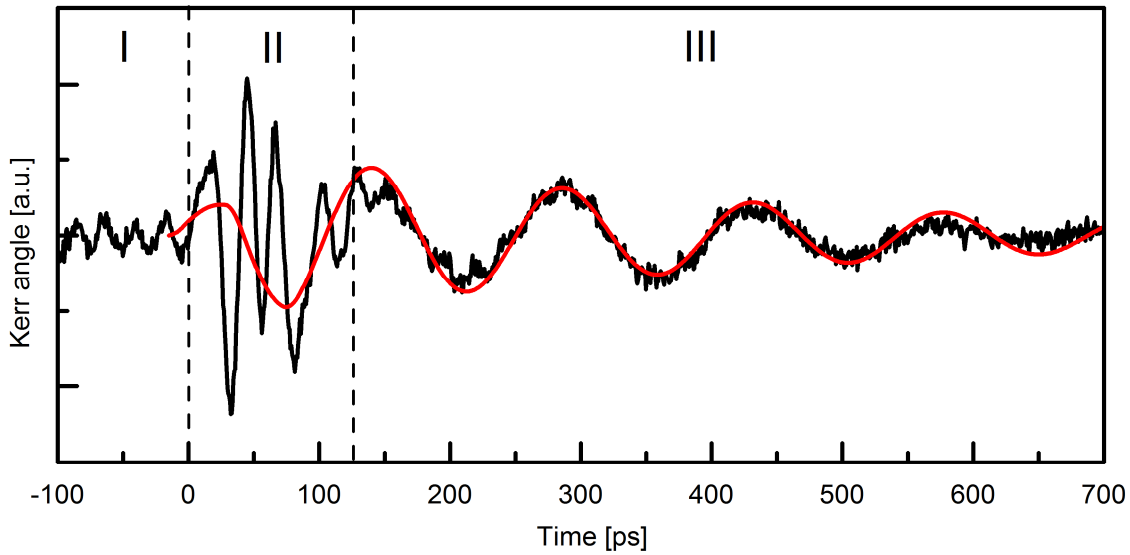

Figure 4.3-1: Pump-probe measurement of the time-resolved changes in the Kerr angle at a magnetic field of 80 mT. The time t = 0 ps corresponds to the arrival of the strain pulse at the (Ga,Mn)As layer. The red curve is a model fit to the strain induced precession derived with the transfer matrix method based on equation(4.3.2). Section II indicates the time, when the strain pulse is inside the magnetic layer. In section I and III, it is in the GaAs substrate.

The strain pulse is inside the magnetic layer in the time interval 0 ps < t < 125 ps (section II in Figure 4.3-1), which can be estimated by the speed of sound, the layer thickness (including the reflection of the strain pulse at the free surface with phase inversion) and the duration of the pulse itself (about 35 ps). The calculated shape of the strain pulse is shown in Figure 4.3-2 b). The strain pulse modulates the (Ga,Mn)As layer thickness and the temporal evolution of the relative layer thickness can be expressed as

$$\bar{\eta}(t) = \frac{\Delta d(t)}{d} = \frac{1}{d}\int_0^d \eta_{zz}(t,z)dz\,. \tag{4.3.1}$$

The coordinate $z = 0$ corresponds to the GaAs/(Ga,Mn)As interface and $\Delta d(t)$ corresponds to the time evolution of the layer thickness change. This gives the following time evolution of $\bar{\eta}(t)$ shown in Figure 4.3-2 a). The compression and dilatation of the layer in z-direction interrupted by time intervals without a change in the layer thickness is illustrated. This occurs when the bipolar strain pulse is completely inside the layer.

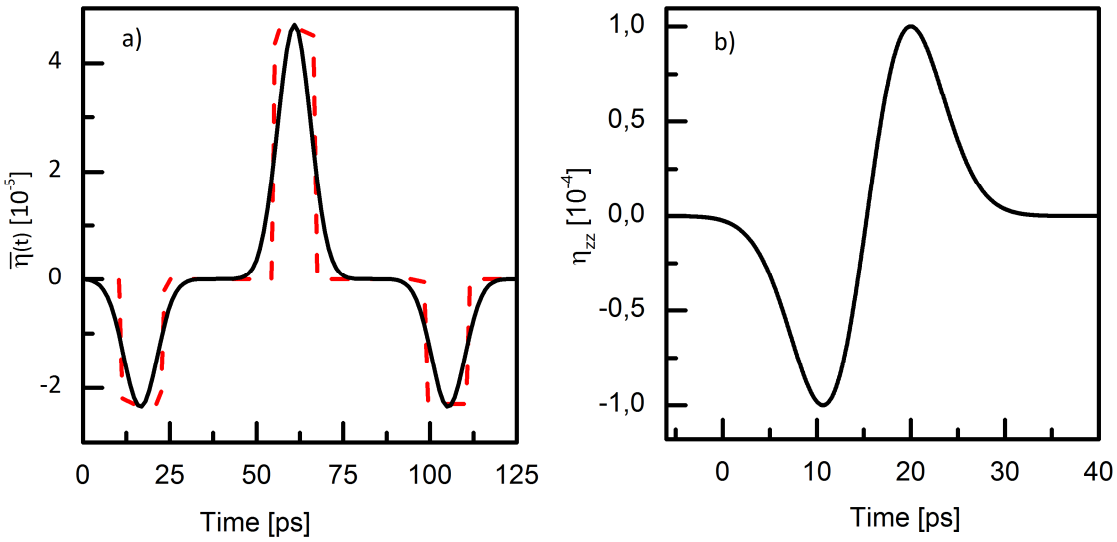

Figure 4.3-2: a) Time evolution of the relative (Ga,Mn)As layer thickness (black line) according to formula (4.3.1). The time evolution can be approximated by square pulses (dashed red line). b) Strain pulse profile injected into the GaAs substrate.

Pronounced fast oscillations are observed, when the strain pulse is travelling inside the magnetic layer. The origin of these oscillations is not clear in detail. There are multiple effects that may contribute to the signal. The change of the reflectivity induced by the strain pulse seems to be an important factor[50]. The magnetic field dependence of both the Brillouin oscillations and the oscillations during the transit of the strain pulse through the layer are shown in Figure 4.3-3. The fact that the fast oscillations occur also without an externally applied field suggests that there is a non-magnetic contribution to the signal originating from e.g. elasto-optic effects or a layer thickness variation[50]. No Brillouin oscillations are visible without applied field. For increasing magnetic field strength the amplitude of the fast oscillations increase rapidly and saturation starting at around 250 mT is observed. On the other hand, the amplitude of the Brillouin oscillations is only weakly increasing with the external magnetic field. The rapid increase in the amplitude of the oscillations in the time interval II and the saturation behavior suggest a ferromagnetic contribution[50]. This conclusion cannot be made for the Brillouin signal.

However the focus of the experiments presented here lies not in the details of the interaction of the strain pulse with the magnetic layer, but the remarkable experimental observation is located in the time region t > 125 ps (see Figure 4.3-1), when the strain pulse has already left the layer. Pronounced oscillations are observed in this interval with a frequency up to 7 GHz. This frequency corresponds well to magnetization precession frequencies of similar structures, obtained in ferromagnetic resonance experiments[93]. The oscillations are only observed in the magnetic field range 0mT < B < 200 mT as shown in a waterfall plot of the time evolution of the Kerr signal at different fields in Figure 4.3-4.

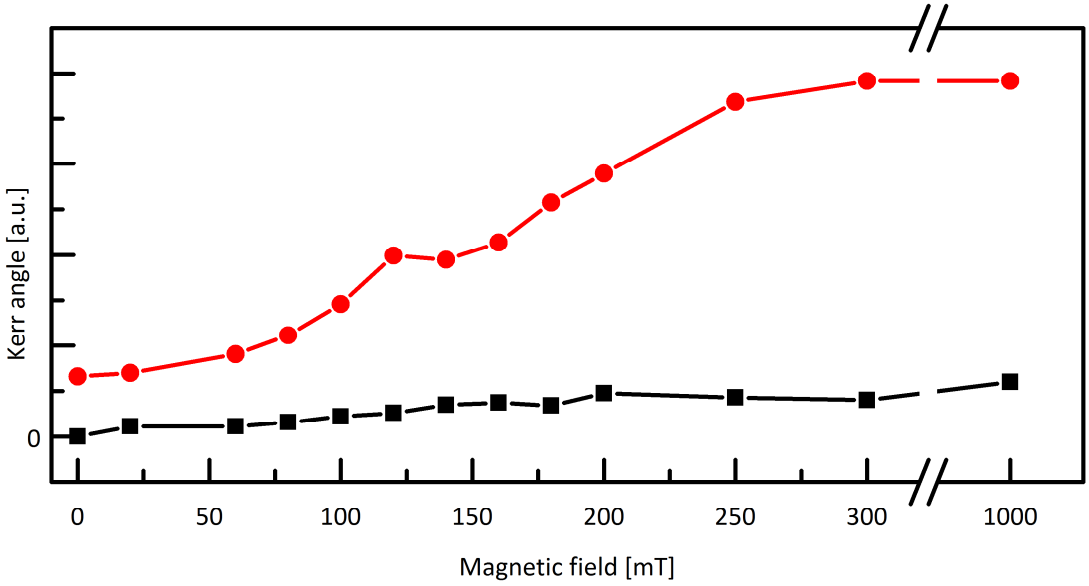

Figure 4.3-3: Magnetic field dependence of the peak amplitude in the Kerr signal for the Brillouin oscillations (black squares) and the fast oscillations (red dots) that occur during the transition of the strain pulse through the magnetic layer.

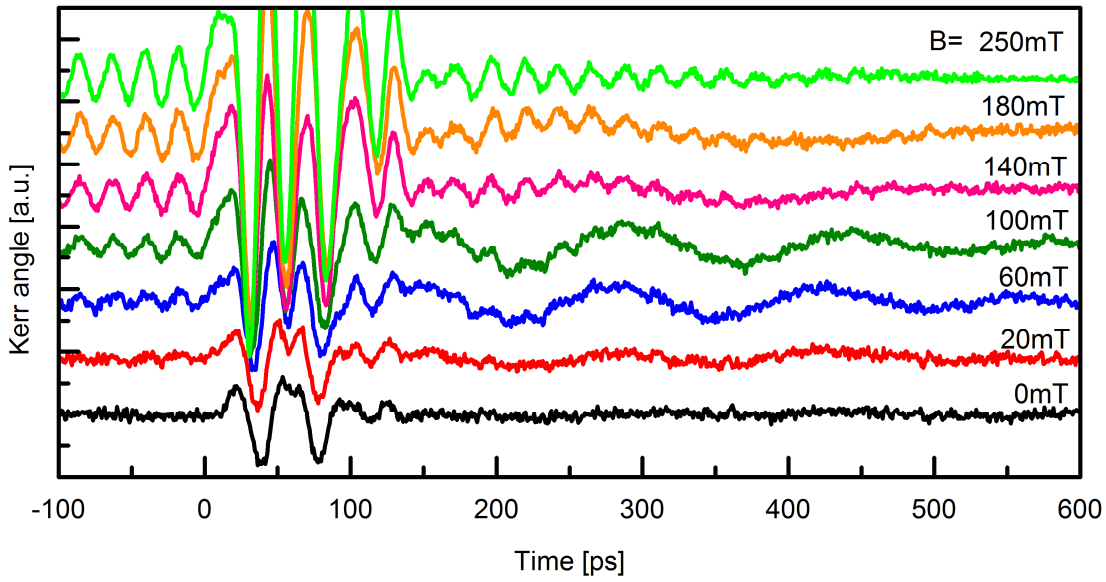

Figure 4.3-4: Waterfall plot of the time evolution of the Kerr signal at different applied magnetic fields at a temperature of 1.6 K.

The amplitude of the oscillations increases up to 80 mT, where they reach a maximum (Figure 4.3-1). For higher fields the amplitude decreases and vanishes above 200 mT (see Figure 4.3-5). The decay time of the oscillations is on the order of 500 ps*. The maximum amplitude of the oscillations is about 1 ‰ of the saturation magnetization.

* The damping is attributed to the p-d-exchange interaction between the free holes and the localized Mn^{2+} ions[78].

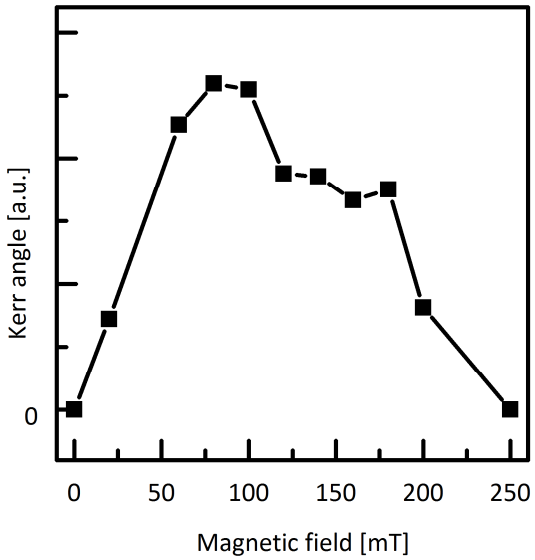

Figure 4.3-5: Maximum amplitude of the slow oscillations after the strain pulse has left the magnetic layer for different magnetic fields

It is known that the generation of the picosecond strain pulse is accompanied by the generation of a heat pulse[24] that can reach sub-ns duration. In a high crystalline substrate and at low temperatures the propagation of this heat pulse is ballistic and the speed is close to the speed of the strain pulse (estimated time delay of about 100 ps). Furthermore, fast magnetization switching by heat pulses has been proved experimentally[14]. To exclude the possibility that a non-coherent heat pulse is responsible for the observed magnetization dynamics, the different nature of the propagation of a heat and a picosecond strain pulse are considered. The situation is depicted in the left panel of Figure 4.3-6.

While the angular distribution of the heat pulse is almost isotropic, the strain pulse propagates strictly perpendicular to the plane of generation. The lateral spatial overlap of the pump and the probe pulse can therefore be varied to scan the angular distribution of the excitation, and these results can be compared with a simple model. The model describes the angular distribution of the heat pulse isotropically* and the strain pulse is described by a Gaussian profile.

The experimental traces are shown in the right panel of Figure 4.3-6 for slightly smaller pump (100 µm) and probe (50 µm) spot sizes, at 6 K and an applied field of 100 mT. The predicted reduction of the signal amplitude for the strain and heat pulse based on the model and the measured reduction based on the right panel of Figure 4.3-6 are collected in Table 4.3-1.

* The effect of phonon focusing, which is a well-known phenomenon for the propagation of incoherent phonons in a crystal, is ignored in this simple model. But anyway it is expected that phonons are deflected from the [100]-direction, and therefore the difference between the heat pulse and the strain pulse is expected to be even larger[20,94][95].

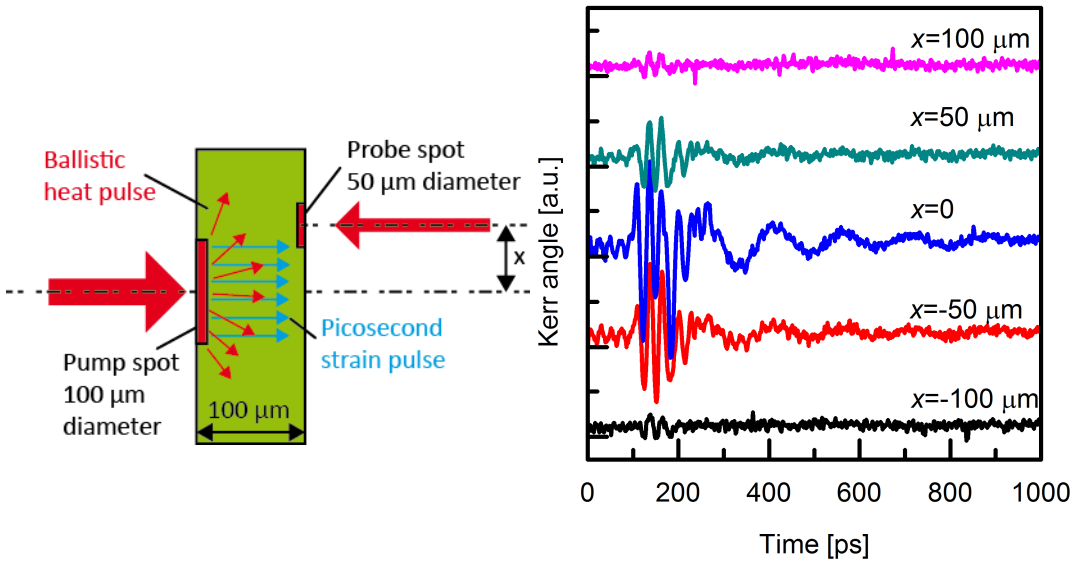

Figure 4.3-6: The differences in propagation characteristics of the picosecond strain pulse and the ballistic heat pulse are illustrated (left panel). By displacing the probe and the pump pulse by a distance *x*, the amplitudes of the heat pulse and the picosecond strain pulse evolve differently according to their angular dependences. The time evolution of the Kerr signal at different lateral displacements is shown in the right panel for slightly smaller pump (100 µm) and probe (50 µm) spot sizes at a magnetic field of 100 mT and temperature of 6 K.

It can be clearly seen, especially for a detuning of 100 µm, that the angular dependence of the excitation is resembled pretty well by the strain pulse model and the deviation from a possible heat like behavior is significant. This indicates that the effect of the heat pulse is not responsible for the induction of the magnetization dynamics. Furthermore, these heat pulses are not shorter than 200 ps and could not induce the fast dynamics that are observed in the time interval $0 < t < 125$ ps or magnetization precession with a period shorter than the duration of the heat pulse, as it is observed in the experiment.

Table 4.3-1: The relative amplitudes for the strain pulse and heat pulse model are shown for the experimentally measured detunings x, together with the experimentally determined amplitude changes based on the right panel of Figure 4.3-6

X (µm)	Strain pulse model	Heat pulse model	Experiment
0	1	1	1
50	0.5	0.78	0.67
-50	0.5	0.78	0.37
100	0	0.43	<0.1
-100	0	0.43	0.1

The following passage will focus on the low-frequency oscillations that are seen in the time interval $t > 125$ ps (section III of Figure 4.3-1), when the strain pulse has already left the layer. A simple model explanation is discussed that interprets the oscillations as

magnetization precession induced by the strain pulse by assuming a linear dependence of the anisotropy parameter $H_{2\perp}$ on the strain as mentioned in section 2.2.3.

The oscillations in the Kerr angle observed in the time interval t > 125 ps are considered to be due to tilt of the magnetization vector $\vec{M}$ by the strain pulse and the subsequent precession of the magnetization around its initial equilibrium position. In this case, once the strain pulse has left the magnetic layer, the signal is expected to vanish at B = 0 T, if only a change of the anisotropy parameter $H_{2\perp}$ is assumend* as there is no initial z-component of the magnetization[79]. $\vec{M}$ is practically parallel to the external magnetic field for B > 200 mT. In this case the modulation of M_z also becomes negligibly small. Both behaviors are seen in the experiments. Therefore, the magnetic field range 0 mT < B < 200mT is of great interest because in this range the direction of the magnetization is determined by the balancing between the externally applied field and the MCA of the magnetic layer. To investigate this field range, it is necessary to describe the magnetization kinetics triggered by the propagation of the strain pulse through the magnetic layer. A 200 nm thick (Ga,Mn)As film grown on GaAs is known to possess a single value of M_z for a perpendicular applied field[77]. It behaves in this respect like a single magnetic domain. This allows for describing the magnetic anisotropy of the layer by the relative changes of the layer thickness $\bar{\eta}(t)$ according to formula(4.3.1). The modification of the built-in strain by $\bar{\eta}(t)$ leads to a modification of the effective magnetic field direction by an angle $\Delta\theta_\eta(t)$ relative to the unperturbed case. Due to the fact that the in-build strain is about three orders of magnitude higher than $\bar{\eta}(t)$, a linear relation between $\bar{\eta}(t)$ and the tilt angle $\Delta\theta_\eta(t)$ is assumed. This leads to:

$$\Delta\theta_\eta(t) = \frac{d\theta}{d\eta_{zz}}\bar{\eta}(t) = \frac{d\theta}{dH_{2\perp}}\frac{dH_{2\perp}}{d\eta_{zz}}\bar{\eta}(t). \qquad (4.3.2)$$

The assumption that the change in the relative thickness of the magnetic layer $\bar{\eta}(t)$ affects only the uniaxial perpendicular anisotropy constant $H_{2\perp}$, leads to the second part of equation (4.3.2). Furthermore, it is assumed that the magnetization is only tilted in the θ degree of freedom.

To be able to fit the experimental data with the model, it is useful to approximate the temporal evolution of the layer thickness $\bar{\eta}(t)$ by a sequence of square pulses as shown in Figure 4.3-2. This leads to a temporal evolution of $\bar{\eta}(t)$ in the form of jumps between

* There should be an effect on the cubic anisotropy parameters, but they are much smaller than the uniaxial anisotropy and therefore the influence of the strain pulse on the magnetization is negligible.

constant values of $\bar{\eta}(t)$. At a constant value of $\bar{\eta}(t)$, $\vec{M}(t)$ precesses circularly around the direction defined by θ and $\Delta\theta_{\eta}(t)$. When $\bar{\eta}(t)$ changes to another value, $\vec{M}(t)$ precesses around this new direction* determined by $\bar{\eta}(t)$. This description allows to determine the precession frequency and $\frac{d\theta}{d\eta_{zz}}$, which can be interpreted as the tilt efficiency. This is done by fitting the observed temporal evolution of the Kerr rotation and therefore the evolution of ΔM_z by means of a transfer matrix method. The layers of the transfer matrix are the time intervals with different strain conditions for the magnetic layer in this case. The fitting is demonstrated in the time domain in Figure 4.3-1 for an external field of 80 mT. Based on this fitting procedure the magnetic field dependence of the precession frequency and $\frac{d\theta}{d\eta_{zz}}$ are obtained from the experimental data and are shown in Figure 4.3-7.

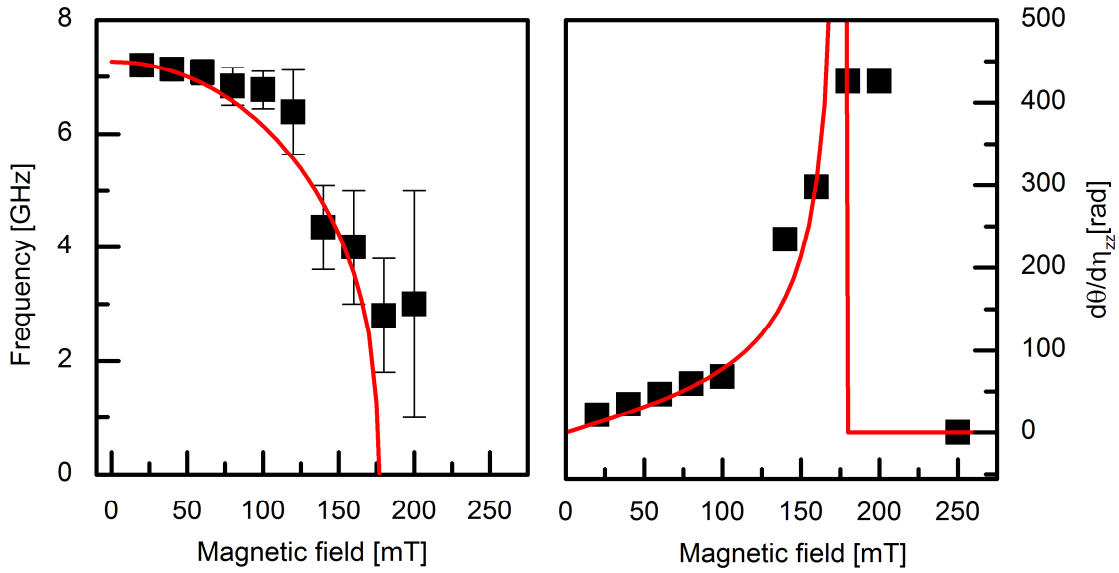

Figure 4.3-7: (left panel) Magnetic field dependence of the precession frequency based on the experimental data (black squares) and a fit of the field dependence (red line) according to equation (4.3.3) based on the MCA parameters derived for this sample. (right panel) The tilt efficiency for different magnetic fields derived from the experimental data (black squares) and a theoretical prediction (red line) based on the minimization of the free energy.

The experimental data shows a clear decrease in the precession frequency for increasing magnetic field (left panel of Figure 4.3-7). This dependence can be reproduced by minimizing the free energy at the given field orientation for the precession resonance

* To illustrate this process it is useful to think of an example of a more classic oscillator: the pendulum. In this analogy the magnetization direction itself is the mass of the pendulum and the magnetization equilibrium position is the suspension point. So the strain pulse is not driving the mass of the pendulum, but the suspension point and the magnetization starts to precess around this new suspension point.

field H_R according to Ref. [90] by equation (4.3.3) and the MCA parameters of the sample (see chapter 4.1). The magnetic field dependence of the tilt efficiency $\frac{d\theta}{d\eta_{zz}}$ (right panel of Figure 4.3-7) shows an increase for magnetic fields up to 200 mT, where it reaches its maximum, and then the tilt efficiency decreases rapidly for higher fields. Again an approach of minimizing the free energy leads to a theoretical curve that is fitted to the experimental data with a field independent value of $\frac{dH_{2\perp}}{d\eta_{zz}}$ as the only fitting parameter

$$\left(\frac{\omega}{\gamma}\right)^2 = \left\{ \begin{array}{l} H_R\cos\theta + \left(-4\pi M + H_{2\perp} - 2H_{4\|} - \frac{H_{2\|}}{2}\right)\cos^2\theta \\ +\left(H_{4\perp} + H_{4\perp}\right)\cos^4\theta + H_{4\|} \end{array} \right\} \times \left\{ \begin{array}{l} H_R\cos\theta + \left(-4\pi M + H_{2\perp} + \frac{H_{4\perp}}{2} - \frac{H_{4\|}}{2} - \frac{H_{2\|}}{2}\right)\cos 2\theta \\ +\left(\frac{H_{4\perp}}{2} + \frac{H_{4\|}}{2}\right)\cos 4\theta \end{array} \right\} - \left(\frac{H_{2\|}}{2}\right)^2\cos^2\theta \quad (4.3.3)$$

The experimental data is in excellent agreement with the theoretical model for a value of $\frac{dH_{2\perp}}{d\eta_{zz}} = 85$ T. This value is similar to data reported on comparable (Ga,Mn)As layers[65].

4.4. A posterior theoretical framework

The experimental results and the simple theoretical model presented in the previous section inspired the development of a more rigid theoretical framework by *Linnik et al.* that can be found in detail in ref [16]. A brief overview of this work is followed by a comparison to the experimental results presented in the previous section.

The theoretical description relies on the Landau-Lifshitz approach combining the externally applied magnetic field with the MCA of the structure to an effective field B_{eff}. The direction and value of the effective is determined by the magnetic free energy F of the system. The MCA parameters are derived from the microscopic model of *Dietl et al.*[71] for hole-mediated ferromagnetism in ferromagnetic semiconductors and the system is modelled according to the sample parameters described in chapter 4.1. The free energy of the system contains magneto-elastic terms that relate the strain introduced to the system

by the strain pulse to changes in the free energy. The formula is basically identical to formula (4.2.1), but the change of the static MCA parameters with the applied strain is incorporated leading to

$$\begin{aligned} F(\theta,\varphi) = & \left[B_d + \left(A_{2\eta} - 2A_{4\eta}\right)\left(\eta_{zz} - \eta_{xx}\right)\right]\cos^2\theta \\ & + \left[B_c + 2A_{4\eta}\left(\eta_{zz} - \eta_{xx}\right)\right]\cos^4\theta \\ & + \frac{1}{4}\left(3 + \cos 4\varphi\right)\left[B_c - A_{4\eta}\left(\eta_{zz} - \eta_{xx}\right)\right]\sin^4\theta \\ & + \frac{1}{2}A_{2xy}\eta_{xy}\sin^2\theta\sin 2\varphi - \mathrm{B}_x\sin\theta\cos\varphi \\ & - B_y\sin\theta\sin\varphi - B_z\cos\theta \end{aligned} \tag{4.4.1}$$

The demagnetization energy/shape anisotropy is of a thin magnetic film is described by B_d and B_x, B_y and B_z are the projections of the external magnetic field on the coordinate axes defined in Figure 4.1-1. The parameters $\left(A_{2\eta} - 2A_{4\eta}\right)\left(\eta_{zz} - \eta_{xx}\right)$, $B_c + 2A_{4\eta}\left(\eta_{zz} - \eta_{xx}\right)$, $B_c - A_{4\eta}\left(\eta_{zz} - \eta_{xx}\right)$ and $A_{2xy}\eta_{xy}$ are defined as the perpendicular uniaxial, perpendicular cubic, in-plane cubic and in-plane uniaxial anisotropy field, respectively. $A_{2\eta}$ and $A_{4\eta}$ are the magneto-elastic constants that relate the induced strain to a change in the MCA. This simplified form of the free energy is possible as the static growth induced strain is equal in the layer plane $\eta_{xx} = \eta_{yy}$.

In the Landau-Lifshitz approach the effective field is determined by the gradient of the magnetic free energy and no change in the overall magnetization by the strain is assumed. Furthermore, damping is neglected. With this formulation it is possible to define rates that describe how sensitive the tilt of the effective field by the strain pulse is in the different angles relative to an arbitrary equilibrium direction of the magnetization defined by the equilibrium angles θ_0 and φ_0. The tilt or precession rates can be thought of as torque acting on the magnetization. If the effective field is change in θ the resulting torque will drive the initial magnetization only in φ and vice versa for a tilt in φ that will drive the magnetization in θ. They are defined as

$$f_\varphi = -\gamma\cos\theta_0 \cdot \left(2A_{2\eta} + A_{4\eta}\sin^2\theta_0\left(\cos 4\varphi_0 - 1\right) + A_{4\eta}\cos^2\theta_0\right) \tag{4.4.2}$$

with the tilt rate in θ f_φ and

$$f_\theta = -\gamma A_{4\eta}\sin^3\theta_0\sin 4\varphi_0 \tag{4.4.3}$$

the tilt rate in φ f_θ. γ is the gyromagnetic ratio. The notation of the tilt rates is illustrated in Figure 4.4-1.

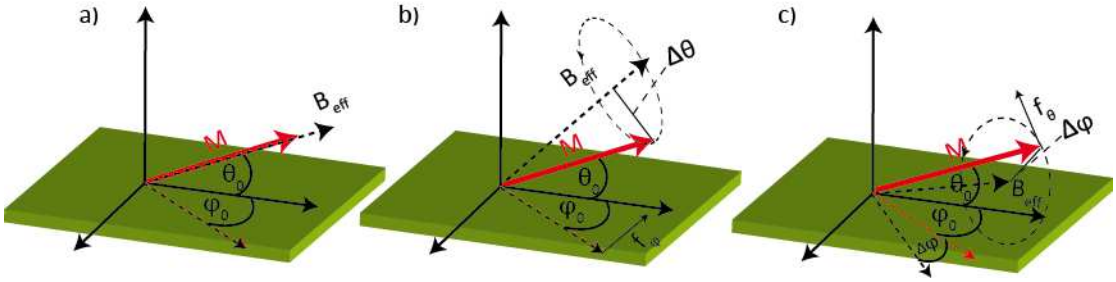

Figure 4.4-1: a) the orientation of the magnetization is determined by the angles θ_0 and φ_0 without a strain pulse. The effective field B_{eff} is tilted by the strain pulse either b) in θ or c) in φ. This leads to the effective precession rates f_φ and f_θ, respectively. The initial direction of precessing is in both cases shown by small solid arrows. The projections of the magnetization and the effective field direction on the layer plane are indicated by red and black dashed arrows, respectively.

This formulation of the tilt rates is possible under assumption of a single domain and only small angle changes induced by the strain pulse.[*] The rates in formula (4.4.2) and formula (4.4.3) therefore relate the response of B_{eff} on the strain pulse to the magnetization equilibrium direction[†].

Interpreting the tilt rates describe above with respect to the experimental conditions leads to the following conclusions. For zero external magnetic field in perpendicular magnetic field geometry ($\theta_0 = 90\,°$ and $\varphi_0 = 0\,°$) the strain pulse does not trigger magnetization precession. The effective field direction changes only in θ_0, but not in φ_0. Therefore, the tilt in the equilibrium direction is only in the angle θ as f_θ remains zero[‡]. It follows that f_φ increases almost linearly with increasing applied field till the switching field (Figure 4.4-2a), when the magnetization snaps to the hard axis at about 180 mT. This description by tilt rates therefore describes the same behavior as is done by the model in section 4.3 that includes only the change in a single anisotropy constant by the strain pulse. Furthermore the model confirms the assumption of a tilt of the effective field only in the angle θ. The rates described here give information only about the effectiveness of the tilt of the effective field, but not about the effectiveness of the tilt of

[*] Actually the aim of the experiments presented in this thesis is the realization of precessional switching of the magnetization by ps-strain pulses. This inherently means large precession angles and large tilt angles induced by the strain. Nevertheless this approximation proves valid for the small angles realized in chapter 4.3.

[†] In this formulation the effect of the uniaxial in-plane anisotropy of the layer is not incorporated. However this uniaxial in-plane anisotropy modelled by a weak shear strain has a significant effect that is described and utilized in the chapters that follow.

[‡] With the incorporation of the uniaxial in-plane anisotropy in the model, a small contribution for f_θ is present for all fields, including zero field, but the predicted effect is small.

the magnetization itself. The other important factor for the effectiveness of the tilt is the precession frequency of the magnetization around the tilted effective field. This function is decreasing with increasing field (Figure 4.4-2 b). The competition of the two effects* is shown in the calculated precession amplitude δm_z^{max} in Figure 4.4-2 c. The theoretical prediction of an optimum intermediate magnetic field for the maximum precession amplitude agrees well with the experimentally observed behavior shown in Figure 4.3-5.

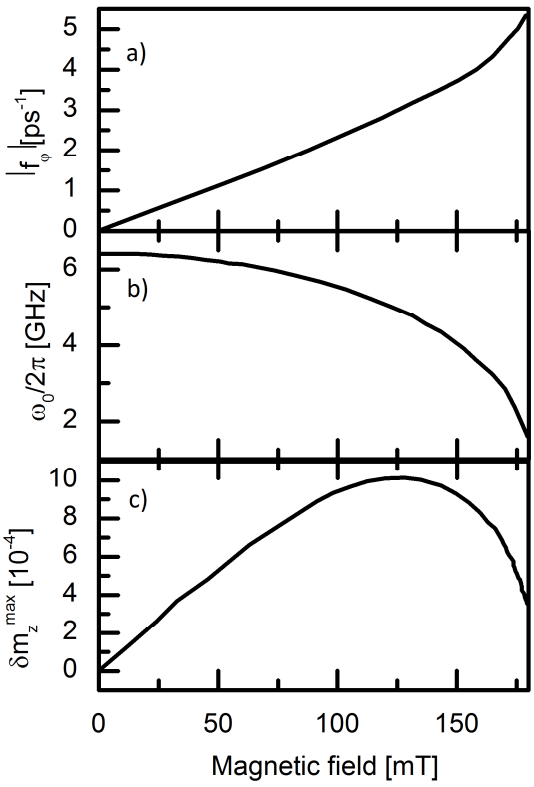

Figure 4.4-2: Magnetic field dependence in Faraday geometry calculated for a in-built strain of $\eta_{zz} = 2 \cdot 10^{-3}$ and a model magnetic layer according to the structure described in section 4.1 for (a) the tilt rate in the angle φ, (b) the precession frequency ω_0 of the magnetization and (c) the magnetization precession amplitude[16] δm_z^{max}.

The theory further predicts no change of the magnetization equilibrium direction, if the magnetization is parallel to the field applied perpendicular to the film as it is observed in the experiments. Furthermore, it is shown that the excitation of the magnetization is spatially non uniform due to the traveling of the strain pulse through the layer. The experiments shown in chapter 4.3 have no spatial resolution perpendicular to the layer plane, but an averaged magnetization is measured by the Kerr effect. However the lack of spatial uniform magnetization gives rise to an additional exchange term to describe the magnetization that lead to the expectation of an energy splitting between different magnetic excitations. In the experiments only a single frequency precession is observed.

* It is illustrative to think about the extreme case, when the precession frequency is much lower than the period the equilibrium orientation of the magnetization is change by the strain pulse. In this case no tilt of the magnetization is observed independent on the actual strength of the change of the equilibrium orientation of the magnetization.

Finally the theory predicts an elliptical precession with a main axis parallel to the layer plane and an ellipticity that depends on the magnetic field.

4.5. Conclusion

In conclusion, the manipulation of the magnetization of a thin ferromagnetic layer by a picosecond strain pulse has been demonstrated for the first time. An all-optical setup in perpendicular magnetic field geometry has been used to generate picosecond strain pulses. To detect the changes of the magnetization associated with the influence of the strain pulse on the magnetic layer advantage of the optical Kerr effect has been taken in a cryogenic environment. The approaching of the strain pulse to the magnetic film could be traced by the observation of Brillouin oscillations. A strong and fast response of the film has been observed during the transition time of the strain pulse inside the film. Finally, the unperturbed precession of the magnetization could be observed when the strain pulse has left the magnetic layer. A simple model describes the influence of the strain pulse on a single, homogenous magnetic domain and the resulting tilt of the equilibrium magnetization direction to the change of one component of the magneto-crystalline anisotropy by the strain pulse only. This is the basis for the theoretical explanation and modelling by an approach of minimizing the free energy of the system. This allows for the description of the observed field dependence of the precession frequency by the theoretical model based only on the parameters of the MCA derived from a hysteresis measurement without any fitting parameter. The tilt efficiency can be modeled in the same manner by the use of one fitting parameter that is in excellent agreement with literature values. A posterior theoretical description based on a more rigid theoretical treatment confirms the experimental findings and adds more detailed insight into the mechanisms that are relevant for strain induced precession of magnetization. Furthermore, it confirms the conclusions derived from the first very simple theoretical consideration.

This first demonstration is the starting point to a more sophisticated approach of applying in-plane magnetic fields for the excitation of more complex magnetic excitations than the precession of a single, homogenous domain around its equilibrium direction. These complex excitations, called spin waves, are the topic of the next chapter.

5. Selective spin wave excitation in (Ga,Mn)As by ultrafast acoustics

„If I had asked people what they wanted, they would have said faster horses."

Henry Ford

The approach of strain induced magnetization precession is further developed to reach for higher precession frequencies that allow for faster manipulation of the magnetization state of a material. This is demonstrated by the excitation of spin waves of higher order. In the quantum mechanical description of an interacting ensemble of spins this excitations are called magnons. As a potentially useful result for applications of spin waves in information processing[10,15,72], selective excitation of a single spin wave mode by picosecond acoustics can be realized by the appropriate choice of the applied magnetic field.

The chapter starts with the theoretically predicted possibility of the excitation of magnetization precession with an external magnetic field applied in the layer plane. In this case no tilt of the equilibrium magnetization direction out of the layer plane by an external magnetic field is needed. Furthermore, the topic of a spatial non-homogenous excitation of magnetization is covered. The next section gives a brief introduction in the nature of magnons and their properties in (Ga,Mn)As followed by the experimental demonstration of the strain induced magnetization precession for a magnetic field applied in the layer plane. The appropriate tuning of the external field allows selecting between a regime of multimode and single mode excitation of spin waves. Furthermore, strain induced magnetization precession is observed even without the application of an external magnetic field. The experimental findings are confirmed by a rigid theoretical model that relates the excitation efficiency for certain spin wave modes to the spatial overlap with the according phonon wavefunctions.

5.1. A priori theoretical motivation

The same theoretical framework by *Linnik et al.* that can be found in detail in Ref. [16] and partly described in section 4.4, is the starting point for the experiments as

well as the theoretical description presented in this chapter. The theoretical model describes, how a longitudinal strain pulse can excited magnetization precession in the case of applying an in-plane magnetic field.

For the in-plane application of an external magnetic field along certain high symmetry crystallographic directions both tilt rates f_φ and f_θ described in equation (4.4.2) are zero. In this case no excitation of the magnetization by a longitudinal strain pulse is possible. However excitation is possible, if there is uniaxial in-plane anisotropy that is modelled by a weak shear strain. The introduction of the uniaxial in-plane anisotropy leads to the breaking of the symmetry in the system, which allows for an interaction of the in-plane magnetization oriented along the high symmetry crystallographic directions with the longitudinal strain pulse. It is an experimental fact that there is a uniaxial in-plane anisotropy in the layer[74]. This anisotropy contribution turns the easy axis of magnetization towards the [1-10] direction. In this case f_φ remains zero but f_θ is not vanishing. It is expected that f_θ is two orders of magnitude smaller than f_φ for the case of perpendicular field, due to the significant difference in the magneto-elastic coefficients. Therefore, the tilt is expected to be much smaller. However, the tilt efficiency increases for increasing in-plane uniaxial anisotropy.

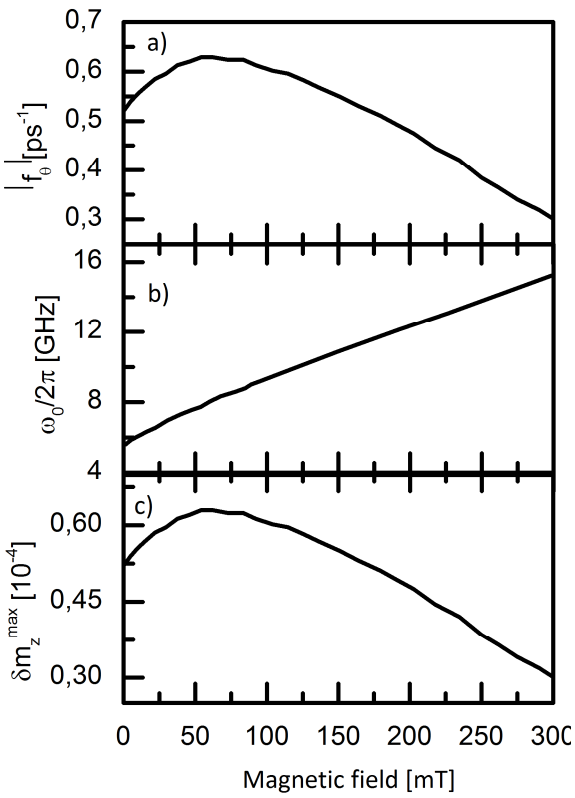

Figure 5.1-1 Magnetic field dependence of (a) the in-plane tilt efficiency f_θ, (b) the precession frequency ω_0 and (c) the expected maximum amplitude of magnetization precession δm_z^{max} induced by a strain pulse like in chapter 4.3. The magnetic field is applied along the [100]-direction.[16]

Furthermore, f_θ describes a tilt of the effective field by the strain pulse in the layer plane for an external field applied along the [100]-direction. On the one hand the in-plane

tilt efficiency is expected to decrease for increasing magnetic field (Figure 5.1-1a) unlike the tilt efficiency f_φ for the application of a field along the [001]-direction in the out of plane geometry presented in the last chapter. But on the other hand the precession frequency increases with increasing field for the in-plane geometry (Figure 5.1-1b), because of the increase of the effective magnetic field B_{eff} for this geometry. The combination of the two effects leads to a similar shape of the magnetic field dependence of the expected magnetization precession amplitude δm_z^{max} compared to the case of out-of-plane magnetic field, but with smaller amplitude. There is also an optimum excitation regime for magnetization precession at intermediate fields, but the amplitude does not drop to zero at a certain field, because of the continuous turn of the magnetization in the in-plane geometry and no snap to a new field direction like in the out-of-plane case.

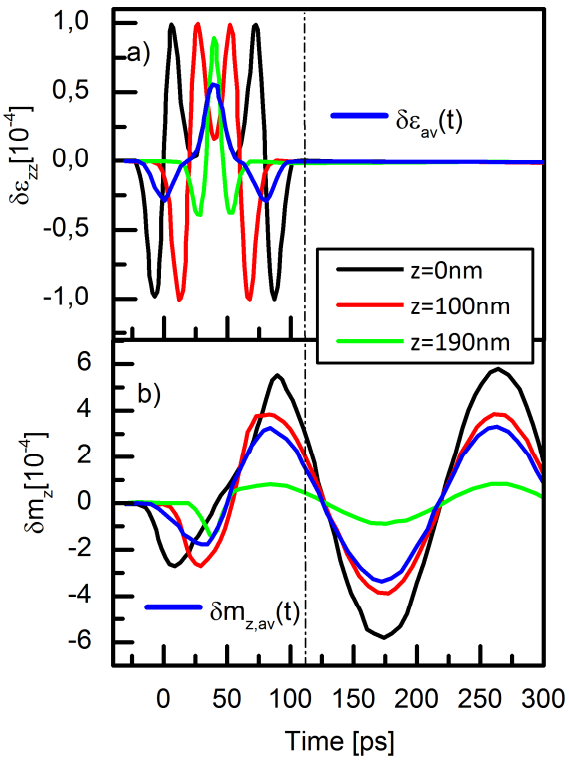

Figure 5.1-2: Temporal evolution at different coordinates z in the layer and the average above the film thickness of (a) the strain in the magnetic layer and (b) the z-component of the magnetization. The dash-dotted vertical line marks time, when the strain pulse leaves the layer. The applied magnetic field has a strength of 40 mT and is applied along the [001]-direction[16].

Furthermore, *Linnik et al.* took into account the intrinsic nature of the strain pulse excitation that results in the spatially non-uniform magnetization excitation. The strain pulse has a length comparable to the magnetic layer and therefore cannot be treated as homogenous distortion of the magnetic layer. The strain pulse introduces a local strain at different coordinates that varies throughout the magnetic layer (Figure 5.1-2a) and therefore the magnetization direction (Figure 5.1-2b) is changed differently at every point of the magnetic layer.

The excitation of the magnetization by the strain pulse can be described in the Landau-Lifshitz approach by an additional exchange term that couples the magnetization at different coordinates. A frequency splitting of the spin waves in the finite width film is the result of this exchange coupling that can manifest itself in a beating of different oscillation frequencies in the experimentally observed signal.

5.2. Magnetization precession in the magnon picture

The magnetization is treated as a single magnetic domain precessing in an effective field. Another formulation for this behavior is a collective mode of the spins of the magnetic layer precessing coherently and in phase around the effective magnetic field. This is the ground state of magnetization precession, where all spins precess as a whole[96] (Figure 5.2-1a). This is a spin wave with zero wave vector (k = 0). The question arises about the energetically favorable first excited state. It is intuitive to assume that the first excited mode is the flip of a single spin (Figure 5.2-1b). But due to the exchange coupling of the spins in a ferromagnet this spin flip requires a rather larger amount of energy*. It can be shown that it is energetically favorable not to flip a single spin completely, but to distribute the tilt of the spin over a long range with a small tilt angle[97] (Figure 5.2-1c). This is described by a wave-like motion called a spin wave (Figure 5.2-1d) or, in the particle picture, a magnon. The exchange coupling constant in a (Ga,Mn)As thin film is on the order of $J = 1$ meV[98]. The energy necessary for a single spin flip[41] in an ideal ferromagnet is $E = 8 \cdot J \cdot S^2$, where S is the spin state. This energy is much larger than $k_B T$ for the case of (Ga,Mn)As below the Curie temperature, so no thermal flip of a single spin is possible. In the following some characteristics of magnons are presented and a more detailed explanation of magnon physics is omitted as this is a very broad and a detailed description is beyond the scope of this thesis[99–101].

As the magnon is spread over many spins, a state of long-range-magnetic order is a key requirement for the existence. The magnon is a bosonic quasi-particle with spin 1 and is the result of the spontaneous symmetry breaking of a continuous symmetry according to the Goldstone theorem. As Goldstone particles, bulk magnons have a relatively small energy typically in the µeV region[41], a correspondingly low k-vector, and no rest mass. Magnon frequencies lay in the GHz up to THz regime, which makes them a prosper tool as the precession frequencies determine precessional switching rates for magnetic storage and data manipulation applications[100]. As magnons are bosonic particles Bose-Einstein-Condensation (BEC) of magnons could be demonstrated up to room temperature[102].

* Actually for the example of a Heisenberg ferromagnet the flip of a single spin is not even an eigenstate of the system.

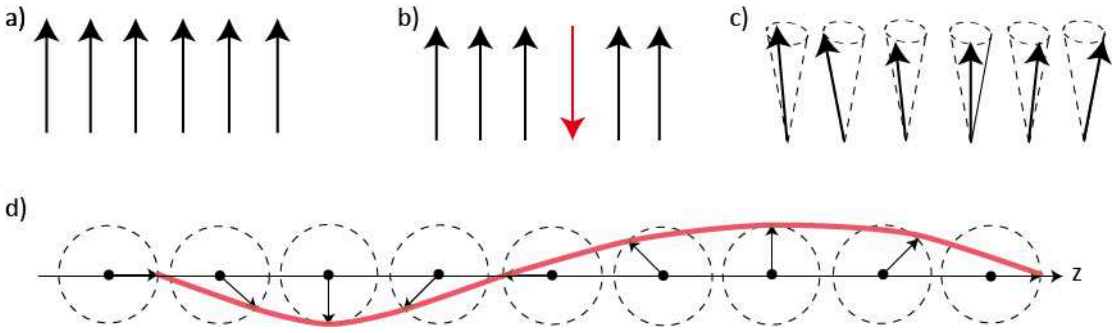

Figure 5.2-1: (a) Ground state of magnetization precession, (b) intuitive possibility of the first excited mode of magnetization precession by flipping of a single spin, (c) energetically favorable excitation of a spin wave spread over many lattice sites. And (d) the formation of a long wavelength magnetization excitation by the coherent precession of spins at different lattice sites from the view on the top of the precession cone[41].

The parallel alignment of all spins of an ideal ferromagnet at zero temperature can be thought of as a vacuum of magnons. Heating of the material leads to the excitation of magnons and therefore, to a reduction of the overall magnetization as a magnon represents the flip of a spin spread over many lattice sites. These non-coherent excitations are called thermal magnons. The other two types of coherent magnon excitations are standing and propagating magnons. The velocity of magnons is a few km/s, similar to the speed of sound, but the dispersion of magnons is parabolic[101] in contrast to the linear dispersion of sound waves.

For the case of thin films of (Ga,Mn)As some deviations, from the classically expected behavior of magnons are observed in the experiment. A few examples are that the classically expected magnon splitting is proportional to the square of the mode number n, but a linear dependence is observed for (Ga,Mn)As[98]. The splitting of the magnons of different mode number is expected to increase for smaller film thicknesses[96], but a constant mode splitting is observed[98]. Furthermore, the magnon splitting is reduced with increasing temperature.

5.3. Magnetization precession without external magnetic field

This section presents the experimental results for the case of in-plane application of an external magnetic field to the same sample as used in the experiments in the last chapter. For this purpose the setup is changed as shown in Figure 5.3-1.

The setup is almost identical to the scheme shown in the last chapter. One change is the magnetic field orientation. It is applied not perpendicular to the magnetic layer, but parallel to the magnetic layer in [100]-direction along the easy axis of magnetization. According to section 5.1, Figure 5.3-1 highlights the necessity of an in-plane uniaxial anisotropy to realize the excitation of magnetization by a strain pulse in this geometry. This

leads to a small angle φ_0 that describes the tilt of the magnetization equilibrium direction from the crystallographic high-symmetry axis. Furthermore, the near zero incident angle setup is modified by adding a non-polarizing beam splitter in front of the bath cryostat to ensure zero incidence angle for the probe beam that eases the mathematical description of the geometry*.

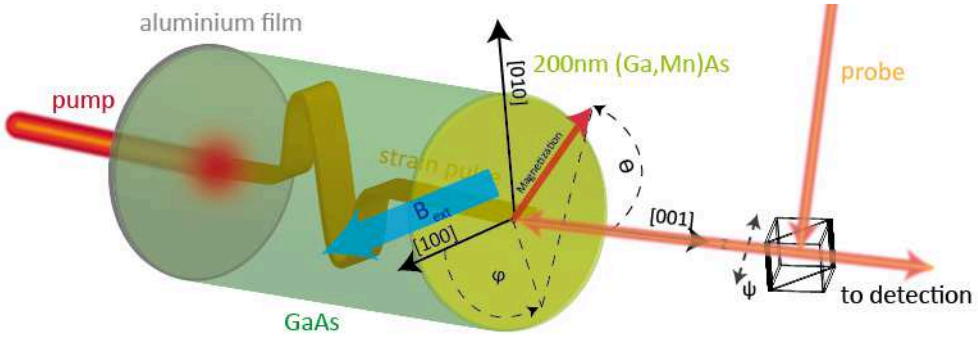

Figure 5.3-1: Experimental setup in Voigt geometry. The magnetic layer is oriented perpendicular to the [001]-crystallographic direction and the magnetic field is applied in the layer plane. The azimuthal angle φ and polar angle θ describe the orientation of the magnetization. Due to the in-plane uniaxial anisotropy the magnetization equilibrium direction is tilted by the angle φ_0 from the [100]-direction. The orientation of the incoming plane of light polarization relative to the [100]-direction is depicted by the angle ψ. The propagation direction of the longitudinal strain pulse is parallel to the [001]-direction.

Nevertheless the situation for the signal analysis is more complicated in this geometry as there is not only the z-component M_z responsible for the Kerr rotation signal, but also in-plane magnetic components and a photo-elastic contribution play a role. A beating of two frequencies is observed for a broad range of magnetic fields. But the most striking observation is the appearance of a single frequency oscillation in a small, but well determined range of magnetic fields. This experimental observation is accompanied by a theoretical description that describes the dynamic Kerr signal by the superposition of spin wave eigenmodes of different order. The appearance of a single precession frequency is attributed to the selective excitation of a single spin wave. At the same time all other mode amplitudes vanish.

For the experimental geometry sketched in Figure 5.3-1 the polarization rotation $\Delta\Phi(t)$ depends on the angle ψ between the probe polarization plane and the [100]-direction. For the experimentally realized situation, when the magnetization is close to the [100] direction, $\Delta\Phi(t)$ can be written as

* The use of the polarization insensitive beam splitter leads to losses of probe laser intensity due to the 50:50 splitting at each passing, but is otherwise not problematic or relevant. It is relevant however that the splitting ratio is not sensitive to the polarization of the beam as this would distort the polarization signal coming from the sample.

(5.3.1) $$\Delta\Phi(t) = a\bar{M}_z(t) + b\bar{M}_y(t)\cos 2\psi + c(t)\sin 2\psi \,.$$

The magnetization dynamics of the layer is covered by the first two terms of equation (5.3.1). The two constants a and b represent magneto-optic contributions to the observed rotation of the polarization plane and the values $\bar{M}_{z,y}(t)$ are averages determined by the spatial distribution of the magnetization in the layer on the one hand and the probe-light-field distribution in the layer on the other hand. The spatial averages of the magnetization probed by the light field can be described by

(5.3.2) $$\bar{M}_z(t) = \frac{1}{d}\int_0^d M_z(z,t)\cos\left[2k_{ph}(z-d)\right]dz$$
$$\bar{M}_y(t) = \frac{1}{d}\int_0^d M_y(z,t)\sin\left[2k_{ph}(z-d)\right]dz$$

with the photon wave vector in the layer k_{ph} and the location of the magnetic layer between 0 and d. This formulation of the averages of the magnetization describes a sensitivity function for the optical probing. The last term of equation (5.3.1) describes the dynamics induced by the strain pulse that are observable through the photo-elastic effect in a magnetic layer with static magneto-optical anisotropy through the static circular dichroism of the material[50]. The fact that not only the z but also the y component of magnetization contributes to the Kerr rotation signal is due to the magneto-optical anisotropy. The effect sensing the z-component is dominated by the circular dichroism[103] and sensitivity to the y component of magnetization is caused by the giant linear dichroism[104] in (Ga,Mn)As.

It is possible to extract the time evolution of $\bar{M}_y(t)$, $\bar{M}_z(t)$ and $c(t)$ utilizing equation (5.3.1) by measuring the dynamical Kerr rotation $\Delta\Phi(t)$ for three different probe polarizations $\vec{e}$ relative to the static magnetization M_0. This is done for $\vec{e} \perp \vec{M}_0(\psi = \pi/2)$, $\vec{e} \parallel \vec{M}_0(\psi = 0)$ and $\vec{e} \measuredangle \vec{M}_0(\psi = \pi/4)$. The three original polarization orientations as well as the processed separation of the three components $\bar{M}_y(t)$, $\bar{M}_z(t)$ and $c(t)$ are plotted in Figure 5.3-2 for an externally applied field of 100 mT.

Although slightly different in amplitude the original data for the three different polarizations (left panel) show a very similar behavior. In the time interval 0 ps < t < 125 ps, when the strain pulse is inside the magnetic layer (grey area in Figure 5.3-2), a rather sharp and non-periodic feature is observed.

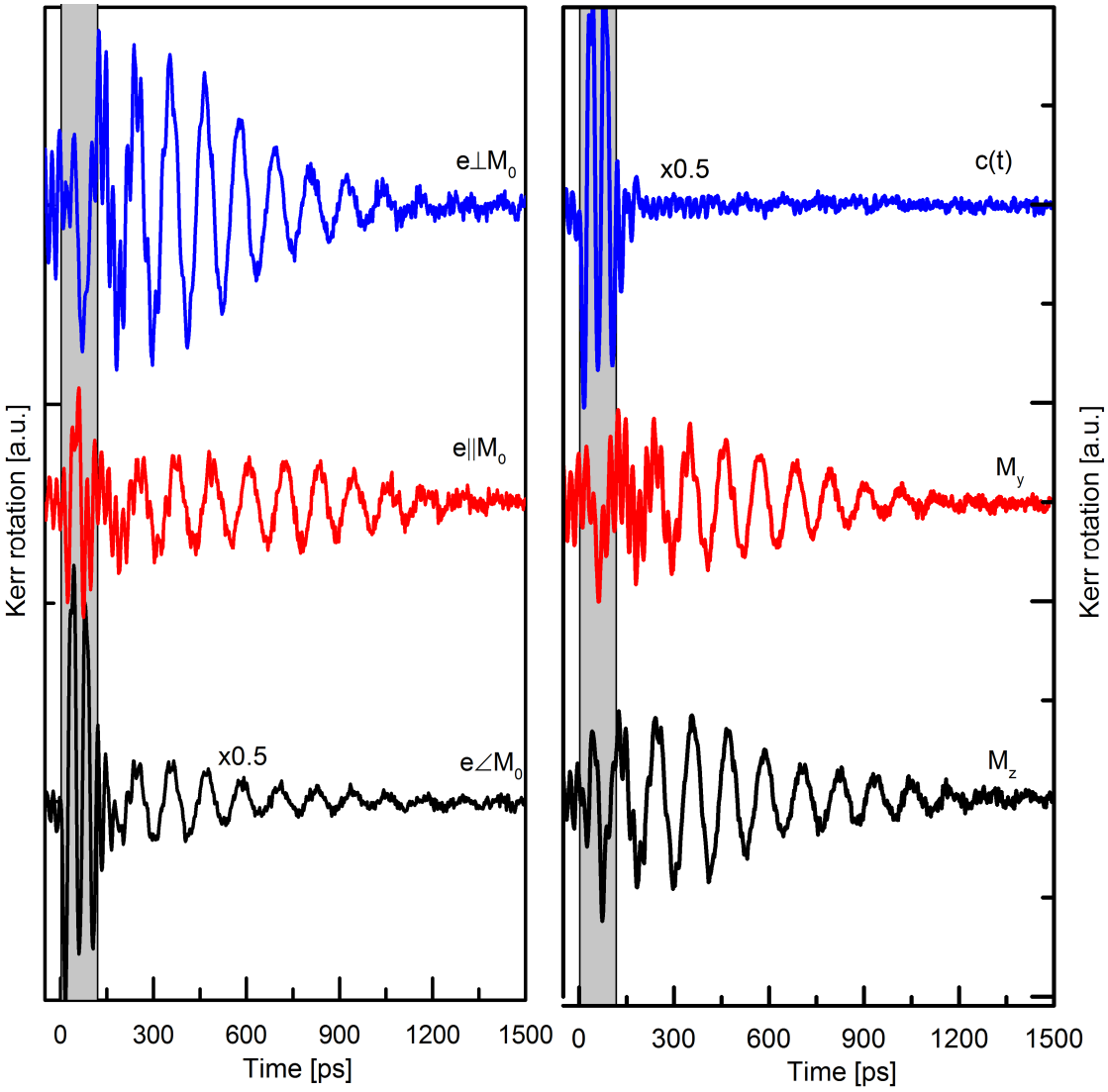

Figure 5.3-2: (Left panel) Unprocessed Kerr rotation data for 3 different orientations of the probe polarization $\vec{e}$ with respect to the equilibrium direction of magnetization $\vec{M}_0$ at a temperature of 6 K and a magnetic field of 100 mT. (Right panel) The same data processed according to equation (5.3.1) to separate the magnetization z- and y-components as well as the elasto-optic contribution *c(t)*. The grey areas indicate the time when the strain pulse is inside the magnetic layer.

When the strain pulse has left the layer in the time interval t > 125 ps, an oscillatory behavior in the frequency range of about 10 GHz is observed. The decay time of the oscillation is on the order of 1 ns. The processed data (left panel of Figure 5.3-2) indicates that the dynamics observed after the strain pulse has left the layer is indeed caused solely by the precession of magnetization. The elasto-optic contribution, which is associated with a direct influence of the strain pulse on the magnetic layer, is almost completely confined to the time interval t < 125ps.

Apart from this feature the temporal evolution again is a damped oscillation and the signals for the z- and y-components of the magnetization evolve in the same manner. If

the envelope is considered, it is obvious from Figure 5.3-2 that it is not just monotonically decreasing with time. The reason for the this behavior can be explained by having a look at the frequency content of the oscillations as is shown in Figure 5.3-3 for an external field strength of 20 mT.

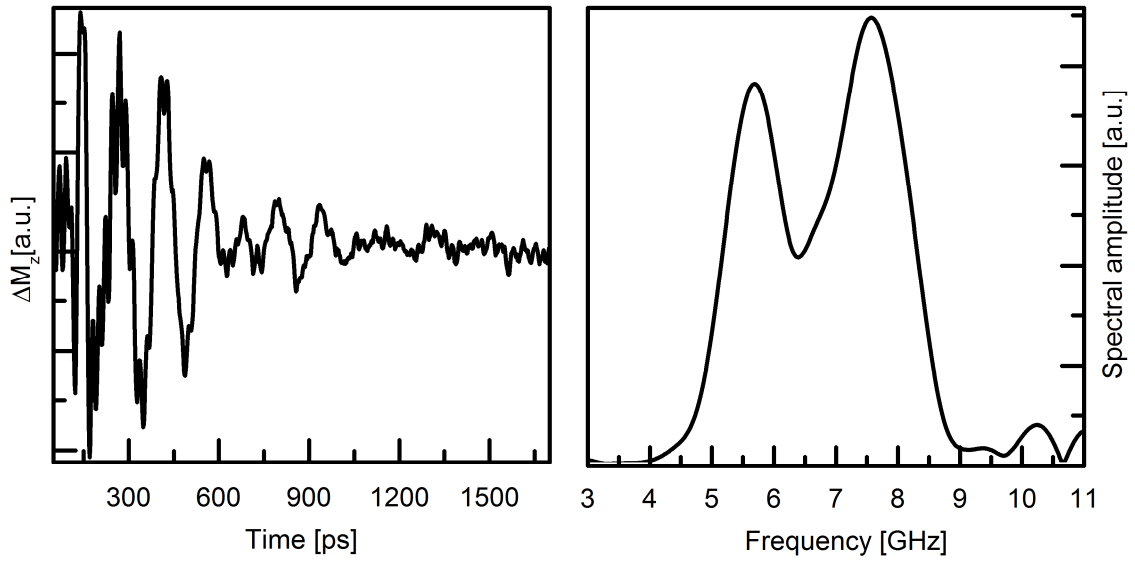

Figure 5.3-3: (left panel) Time evolution of the change in the z-component of magnetization for an external magnetic field of 20 mT at a temperature of 6 K. (right panel) A fast Fourier transform of the time evolution of M_z is shown in the right panel.

The time evolution of the z-component of the magnetization is shown in the left panel of Figure 5.3-3. The oscillation of the magnetization can be clearly observed and the non-monotonous decay of the precession amplitude is very striking at this field. The decay up to 700 ps is followed by a reoccurrence of the signal until it decays finally for larger times. This phenomenon can be ascribed to a beating of two precession frequencies in the time evolution as can be seen from the fast Fourier transform (FFT) of the signal (right panel of Figure 5.3-3). Two frequencies are observed in the Fourier spectrum at 5.5 GHz and 7.5 GHz with a splitting of about 2 GHz and almost equal amplitude. This fact is in good agreement to the observed signals. Similar results have been reported for optical excitation of magnetization precession in earlier works[105], where two spin wave modes of different order are excited.

The evolution of the involved precession frequencies for different magnetic fields is derived from the time domain data, and the corresponding FFT spectra are shown in Figure 5.3-4.

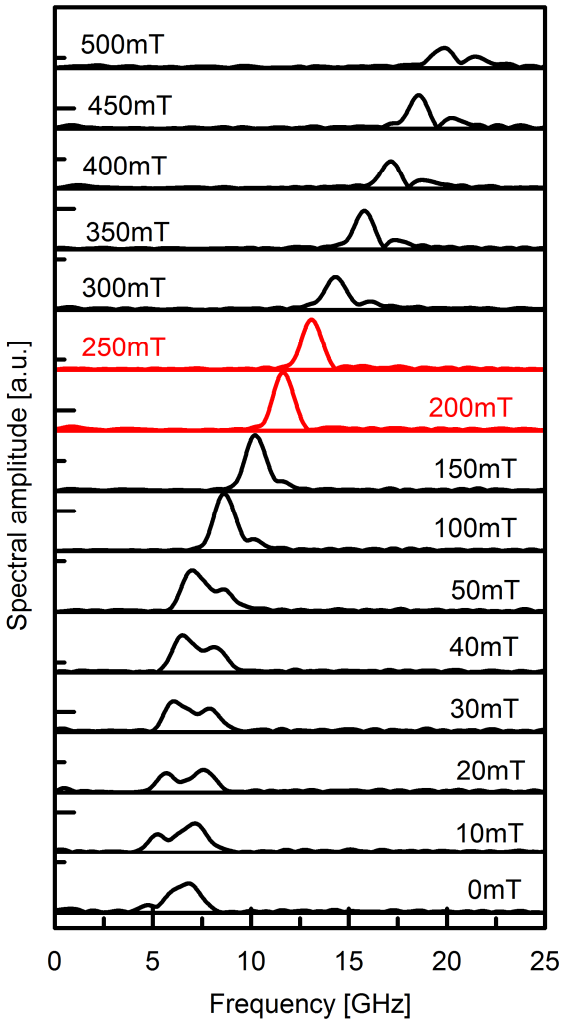

Figure 5.3-4: Fourier spectra processed from the dynamic Kerr signals recorded at different magnetic fields from 0 mT to 500 mT at a temperature of 6 K. The red curves show only a single mode in the Kerr spectrum.

For almost all fields, two precession frequencies are observed that shift to higher frequencies for higher magnetic fields while the splitting of 2 GHz between both frequencies remains constant. The most striking phenomenon is the disappearance of one mode in the magnetic field range $B_0 = 225\ \text{mT} \pm 25\ \text{mT}$. Only a single spectral line is observed. This behavior could not be observed in related experiments using optical excitation of magnetization precession, where the relative amplitude of precession modes is independent on the external magnetic field.[105].

Moreover a pronounced signal can be observed even without an applied external field in contrast to the experiments shown in the last chapter, where the magnetization precession is absent without externally applied field.

The increase of the precession frequency with increasing magnetic field is almost linear for the observed field range (left panel of Figure 5.3-5) for the lower frequency mode. Except for the vanishing of the higher frequency mode at magnetic fields close to B_0 the frequency increase for the higher mode is as well linear with the applied field.

The evolution of the mode amplitude with magnetic field (right panel of Figure 5.3-5) is non-monotonic for both modes. The high-frequency mode decays up to the single precession frequency regime around B_0, where it vanishes. For higher fields the high-frequency mode reappears and the amplitude is constant with about half the amplitude of the low-frequency mode above B_0. The low frequency mode amplitude increases rapidly up to 100 mT, remains constant up to B_0 and then slowly decays.

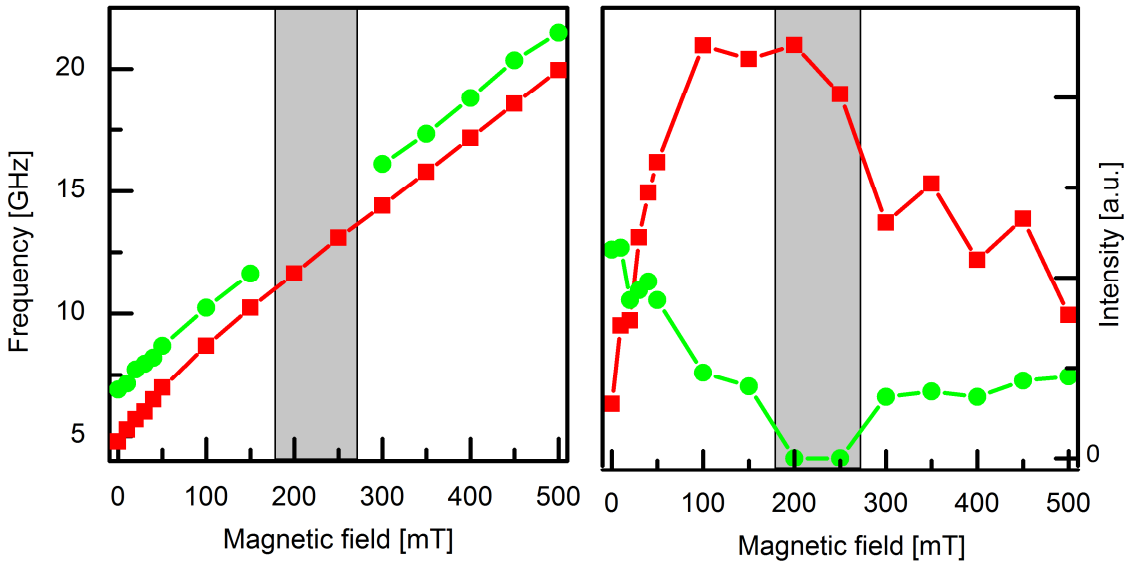

Figure 5.3-5: Magnetic field dependence of the precession frequency (left panel) as well as the mode amplitude (right panel) for the lower (red squares) and higher (green circles) precession modes obtained from the Fourier transformed signal. The grey area indicates the regime of single mode precession.

The magnetic field dependence of the Fourier spectrum that shows a single precession frequency regime is the main experimental result of this chapter. Previous works on optical excitation of magnetization precession do not show any magnetic field dependence of the relation of the precession amplitudes for different spin wave modes[105]. This indicates a significant difference in the excitation for optical and acoustical excitation of magnetization precession. The experimental findings can be interpreted as the excitation of spin wave modes of different order. Around B_0 a single spin mode is selectively excited by the broad acoustic pulse (Figure 2.1-7). In the following a theoretical description* is presented to explain the excitation of multiple spin wave modes by a broad acoustic pulse. Furthermore, a criterion for the selective excitation of a single magnon mode is derived.

The possibility of the excitation of spin waves by a picosecond strain pulse is based on the interaction of phonons with magnons[107]. The strong selection rules based on

* The theoretical model has been developed by Boris Glavin and is presented in the framework of the publication found in Ref. [106]

momentum and energy conservation in bulk materials are relaxed in the experimentally relevant case of thin magnetic films. Due to the breaking of the translational symmetry in thin films the momentum conservation is relaxed and a monochromatic plane acoustic wave can excite resonant standing spin waves independent from the wavelength[108]. In the experiments described above there is not an acoustic monochromatic wave involved, but an ultra-short acoustic pulse. Nevertheless, the theoretical description shows that a strain pulse can excite a number of spin wave modes and that the excitation efficiency depends on the spin wave frequency and therefore on the externally applied field.

As the considered excitation of magnetization is not homogenous, an exchange term has to be added to the Landau-Lifshitz equation[109]. Neglecting damping it follows from equation (4.2.4):

$$\frac{\partial \vec{M}}{\partial t} = -\gamma \vec{M} \cdot \left(-\nabla_{\vec{M}} F + \frac{D}{M_0} \nabla^2 \vec{M} \right) \tag{5.3.3}$$

with the magnetization magnitude described by M_0, and the exchange stiffness constant D. The influence of the strain pulse on the free energy density varying in time and space throughout the magnetic layer causes the complicated evolution of the magnetization direction, while the strain pulse is inside the layer. When the strain pulse has left the magnetic layer the magnetization precesses around its equilibrium position M_0. The deviation of the magnetization from its equilibrium position $\delta M_i(z,t)$ for each component can be expressed in linear approximation by the superposition of standing spin wave eigenmodes $S_i^{(n)}(z)$:

$$\delta M_i(z,t) = \sum_{n=0}^{\infty} C^{(n)} S_i^{(n)}(z) \cos\left(\omega_n t + \alpha_i^{(n)} \right) \tag{5.3.4}$$

with the stationary amplitude $C^{(n)}$ and the stationary phase $\alpha_i^{(n)}$ of the nth (n = 0, 1, 2, 3…) spin wave mode with the frequency ω_n. Obviously the mode amplitude $C^{(n)}$ excited by the strain pulse and the shape of the spin wave eigenmodes $S_i^{(n)}$ are the most important elements in this description. Calculation of the mode amplitudes* reveals that they are proportional to the following overlap integral

$$C^{(n)} \sim \int_0^d \eta^{(n)}(z) S_i^{(n)}(z) dz \,. \tag{5.3.5}$$

* Boris Glavin in Ref [106].

The variable $\eta^{(n)}(z)$ describes the spatial distribution of the strain pulse Fourier component, whose phonon frequency is identical to the frequency of the corresponding spin wave, ω_n, in the magnetic layer. Therefore the overlap integral (5.3.5) describes the spatial matching of the strain pulse and the spin wave eigenfunction. So the problem of investigating $C^{(n)}$ and $S_i^{(n)}(z)$ shifts to the determination of $S_i^{(n)}(z)$ and $\eta^{(n)}(z)$.

As $\eta^{(n)}(z)$ is solely related to the strain pulse propagation inside the layer, the description is not related to the spin waves. Therefore, this part cannot be influenced by the application of an external magnetic field.

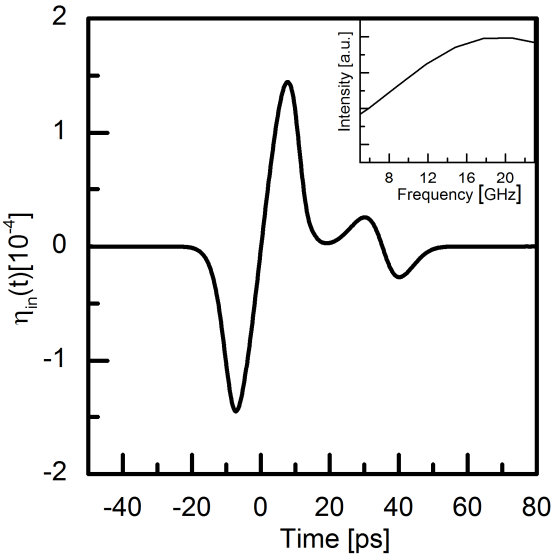

Figure 5.3-6. Time evolution of the initial strain pulse profile under the excitation conditions in the experiment. The inset shows the Fourier transform of the strain pulse in the frequency range from 5 - 25 GHz relevant for the observed magnon frequencies in the experiment.

As the strain pulse amplitude of 10^{-4} is sufficiently low and the temperatures in the experiment are cryogenic, damping and non-linear effects that change the strain pulse shape during propagation through the GaAs substrate are not significant[21,40]. Thus, the strain evolution at every coordinate is described by the initial strain pulse profile $\eta(z,t)=\eta_{in}(t-z/s)$ with the longitudinal speed of sound s. In the relevant frequency range for the observed magnon frequencies, the Fourier spectrum is a smooth function of frequency (inset of Figure 5.3-6). The most important factor that determines the distribution of the strain pulse Fourier components $\eta^{(n)}(z)$ inside the magnetic layer is the free surface of the layer at one side. This requires zero stress at the free surface at z=d. This boundary condition can be incorporated by superimposing of the incident and reflected waves. This leads to the formulation of strain, which satisfies the boundary conditions: $\eta(z,t)=\eta_{in}(t-z/s)-\eta_{in}(t+(z-2d)/s)$. Based on this strain formulation, it is possible to express the spatial distribution of the strain pulse Fourier components inside the magnetic layer by

(5.3.6) $$\eta^{(n)}(z) = 2ie^{(i\omega_n d/s)}\eta_{in}^{(\omega_n)} \sin\left[\omega_n (z-d)/s\right],$$

where $\eta_{in}^{(\omega_n)}$ is the spectral amplitude of the initial strain pulse at the frequency ω_n. The formulation (5.3.6) is independent of the actual strain pulse shape, except for the Fourier amplitude at a certain frequency. This means that a lot of different types of strain pulses generated in different ways and very different symmetries can be used to excite spin waves in thin films. The most important component of equation (5.3.6) is the factor $\sin\left[\omega_n (z-d)/s\right]$ as it carries the whole z-dependence and is therefore responsible for the determination of the coupling efficiency of the strain pulse to the spin wave according to the overlap integral formulation (5.3.5).

For the spin wave eigenmodes, the appropriate magnetic boundary conditions are essential for the correct description of the overlap integral (5.3.5). In the Landau-Lifshitz approach (5.3.3), on which the theory relies, the magnetic boundary conditions can be incorporated by the surface magnetic energy $F_{surf} = K_S \cos^2\theta$ with the angle θ between $\vec{M}$ and the surface normal $\vec{n}$. The orientation of the surface easy axis of magnetization determines the value of the surface magnetic energy parameter K_S. The easy axis may be oriented parallel ($K_S > 0$) or perpendicular to the surface ($K_S < 0$). The magnetic boundary conditions can be formulated according to $\vec{M}\times\left(D\frac{\partial\vec{M}}{\partial\vec{n}} + 2\vec{n}K_S\cos\theta\right) = 0$ in this case[101]. For (Ga,Mn)As the magnetic boundary conditions are not known beforehand. Different magnetic boundary conditions have been suggested and there are three extreme cases considered for (Ga,Mn)As with the magnetization equilibrium position close to the [100]-direction[105,110]: (i) The first is the assumption of a free surface with $K_S = 0$ and $\frac{\partial M_{z,y}}{\partial z} = 0$, (ii) the second is a very high surface energy with $K_S > 0$ that lead to the pinning of the spins at the interfaces and consequently $M_{z,y} = 0$ and the last assumption (iii) is a negative surface energy with $K_S < 0$ that leads to the coexistence of surface- and bulk-like modes in the spin wave spectrum. The best agreement between theory and experiment is achieved with the assumption of the pinning boundary condition and therefore the results of this model are explained in the following*.

The starting point is the assumption of pinning boundary conditions ($K_S > 0$). In this case the components of the spin wave eigenfunction have the well-known form described

* The spin wave eigenfunctions are calculated for all the three boundary conditions mentioned and the $C^{(n)}$ are calculated for all of the three cases and compared to the experimental observation of a single precession line in the framework of the publication found in [106].

by *C. Kittel* [96] $S_i^{(n)} \sim \sin\left[\pi(n+1)z/d\right]$. With this form of the spin wave and the distribution of the strain pulse Fourier component described by equation (5.3.6), it is possible to use equation (5.3.5) to obtain

$$C^{(n)} \sim \frac{(n+1)\sin[\omega_n d/s]}{(\omega_n d/\pi s)^2 - (n+1)^2}. \tag{5.3.7}$$

It is now assumend for simplicity that the frequency spacing between the different spin wave modes is much less than the fundamental frequency ω_0. In this case it can be proposed that the spatial distribution of the strain pulse Fourier component $\eta^{(n)}(z)$ is the same for all spin wave eigenmodes: $\eta^{(n)}(z) = \eta^{(0)}(z)$. The calculated spin wave eigenmodes and the efficiency of the excitation of the spin wave modes for different mode numbers n are shown in Figure 5.3-7 for these simplified assumptions. In the left panel, the eigenmodes of the spin waves $S_z^{(n)}$ are shown for the four lowest order modes. All modes show an oscillatory behavior with the number of oscillations increasing with mode number. The excitation efficiencies by the strain pulse for these lowest four modes are plotted in the right panel of Figure 5.3-7 in dependence of the dimensionless parameter $\omega d/\pi s$ that describes the precession frequency normalized to the travel time of the strain pulse through the magnetic layer. It is seen that all spin wave modes can be simultaneously excited by the strain pulse. The efficiency of the excitation depends on the matching of the strain pulse frequency and the spin wave frequency that can be tuned by the application of an external magnetic field. It turns out that for specific magnetic fields only a single mode can be excited, while the excitation efficiencies of all other modes vanish. Based on equation (5.3.7) it follows that if $\omega d/\pi s$ takes an integer value, the excitation of a single spin wave mode is realized, while all other modes have zero excitation efficiency. This leads to the condition of selective mode excitation in the case of the pinning boundary condition for a mode of number *n*:

$$\frac{\omega d}{\pi s} = n+1. \tag{5.3.8}$$

The spatial distribution of $\eta^{(0)}(z)$ is plotted as well in the left panel of Figure 5.3-7 for the case of selective excitation of the lowest order spin wave number $n = 0$. This situation is indicated in the right panel of Figure 5.3-7 by the dashed line. By comparison of $\varepsilon^{(0)}(z)$ and the spatial mode distribution $S_z^{(n)}$, it can be seen that only the lowest spin wave mode $S_z^{(0)}$ has a non-vanishing overlap integral with $\eta^{(0)}(z)$.

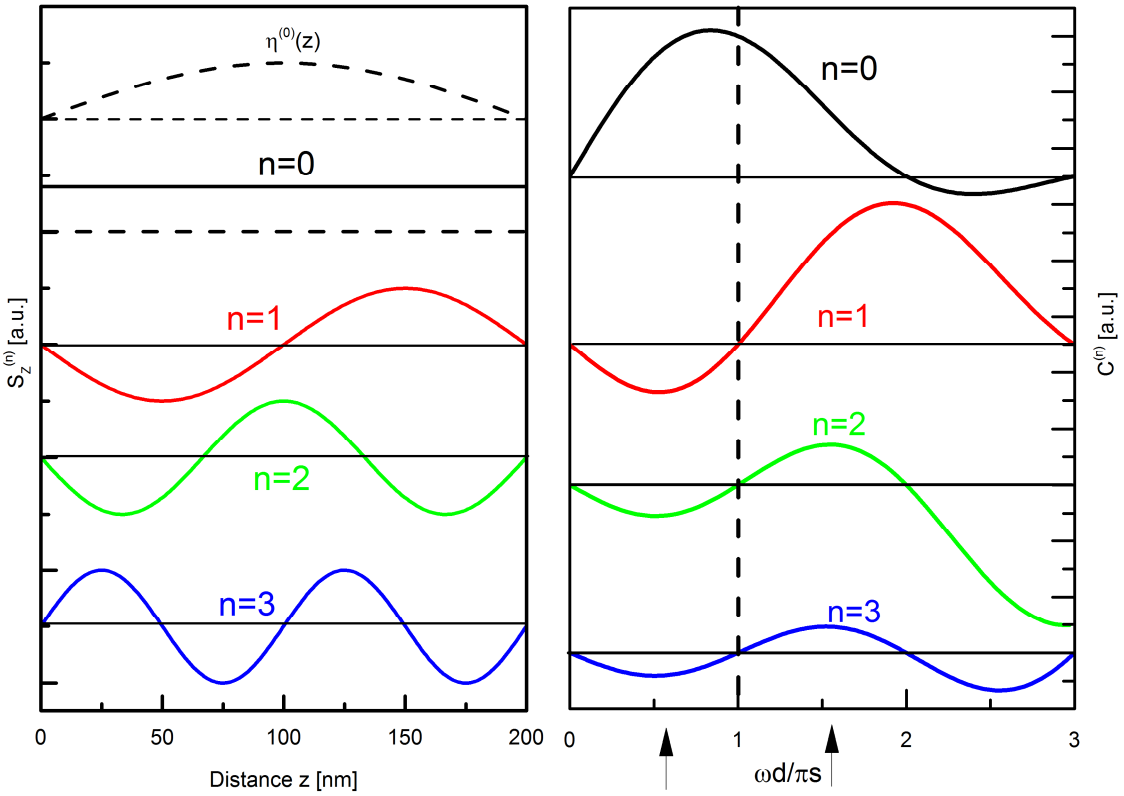

Figure 5.3-7: The left panel shows the four lowest spin wave modes in the 200 nm thick magnetic layer for the case of pinning boundary conditions. The dashed line shows the spatial distribution of the strain pulse Fourier component with a frequency ω_0 that corresponds to the condition $\omega_0 d/\pi s = 1$. The right panel shows the strength of the interaction of the strain pulse with spin wave for different mode orders depending on the dimensionless parameter $\omega d/\pi s$ that describes the precession frequency normalized to the travel time of the strain pulse through the thickness of the magnetic layer.

Comparing the theory to the experimental data the observed single frequency precession for a magnetic field $B_0 = 225$ mT and a frequency splitting of 2 GHz between the lower and higher precession frequency have to be explained.

It is possible indeed to get perfect agreement between the magnetic field dependencies of the spin wave amplitude observed in the experiment (Figure 5.3-5) and calculated for large values of $K_S > 0$[106]. The frequency for the lowest spin wave mode ($n = 0$) according to equation (5.3.8) corresponds to the 12 GHz mode observed in the experiment for a magnetic field of $B_0 = 225$ mT. Therefore, if the experimentally observed line in the case of single frequency precession is attributed to the spin wave with $n = 0$, perfect agreement between the experiment and theoretical description is achieved. But the frequency spacing has to be considered as well. It is not possible to find a reasonable

value for the spin stiffness constant $D^{[110]}$ that allows for a splitting of 2 GHz for the modes*.

Apparently the theoretical description cannot completely account for the experimental observations within one class of boundary conditions. The problem may be solved for more general assumptions on the boundary conditions[106]. The fact that the optical sensitivity of the spin wave detection could not be implemented due to the optical probing close to the fundamental absorption edge of GaAs may be another reason for the incomplete explanation of the experimental observation by the theoretical model. Also the theoretical picture does not include the dissipation of spin wave modes. Strong damping of the upper spin wave mode around B_0 due to a resonant interaction with a different quasi-particle (e.g. phonon) could be the reason for the observation of a single frequency precession at this magnetic field.

5.4. Conclusion and perspectives

In conclusion the excitation of magnetization precession by picosecond acoustic pulses is realized in the absence of an external magnetic field applied in the layer plane as predicted by the theory. Further experimental evidence is given that by the application of a suitable external magnetic field within the magnetic layer and parallel to the easy axis of magnetization, higher order spin wave modes can be simultaneously or selectively excited depending on the strength of the external field. The selective excitation of single spin wave modes is a remarkable result as the excitation spectrum of the initial strain pulse is very broad and thus far from being considered monochromatic. The excitation conditions for a single spin wave mode by an acoustic strain pulse are in strong contrast to optical experiments, where no magnetic field dependence of the spin wave excitation efficiency is observed[111]. The excitation of multiple spin waves stays further in contrast to the experiments in perpendicular magnetic field geometry shown in the previous chapter, where only a single precession frequency can be observed that can be attributed to the precession of a single domain in an external field. Additionally, the observed decay time is about a factor of two longer than for the case of perpendicular field and the frequency of the precession can be increased for higher fields. This shows that the in-plane geometry offers greater versatility and a more favorable behavior toward applications. The experimental findings are supported by a theoretical model based on the Landau-Lifshitz approach that describes the excitation of different spin wave modes to be determined by the spatial overlap of the spin wave mode and the strain pulse frequency distribution inside

* The pinning boundary condition is indeed the only way to realize the selective excitation of a single spin wave by the broad acoustic pulse. The other two boundary conditions are able to describe the frequency splitting, but no regime for selective spin wave mode excitation can be identified[106].

the magnetic layer. Although not perfectly addressing all phenomena that occur in the experimental data, the theoretical description shows that the selective excitation of spin waves is possible and may be used to tailor future sample characteristics for an improved matching of phonon and spin wave eigenfunctions that may finally lead to all-in-one chip solutions with the incorporation of hypersonic nanostructures like phonon cavities[112] or sasers[113] in combination with magneto-optical components. The ability to excite spin waves selectively may also be an interesting feature for novel concepts in magnetization control like the control of spin currents by spin waves that has been recently demonstrated[15].

6. High-amplitude magnetization precession induced by shear strain pulses in high-index (Ga,Mn)As

"To improve is to change; to be perfect is to change often."

Winston Churchill

Up to this point, it could be demonstrated that a picosecond strain pulse is indeed able to induce magnetization precession. This is possible without the need for an external magnetic field, but by the appropriate choice of the external field the precession frequency can be enhanced and a stable regime of single magnon excitation can be found. However, the precession amplitudes presented so far are well below 1 % of the saturation magnetization. This is insufficient for the realization of real magnetization control. It has been shown under static conditions[114] that shear strain has a big impact on the magnetization orientation and a theoretical model predicts stronger influence of a shear strain pulse on the MCA of a (Ga,Mn)As layer [16]. A new approach will be developed in this chapter to generate shear strain pulses and to utilize them to manipulate the state of magnetization. This approach allows for achieving precession amplitudes of more than 10 % of the saturation magnetization at a frequency of about 10 GHz. The approach is only limited technically by the available laser power to reach higher precession angles. Therefore, this approach seems feasible to achieve real coherent control of the magnetization state of a ferromagnetic material.

6.1. Generation and detection of longitudinal and shear strain pulses in high index GaAs

Up to this point, only longitudinal acoustic (LA) waves in high-symmetry substrates have been considered. But another type of acoustic waves exists that involves a shear motion of the medium. These are called transverse acoustic (TA) or shear waves. The difference is illustrated in Figure 6.1-1.

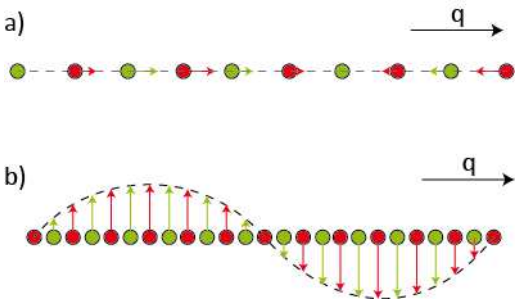

Figure 6.1-1: Illustration of the displacement for an acoustic wave with a) longitudinal and b) transversal character.

The displacement of the atoms in the case of a longitudinal wave is along the propagation direction and involves volume changes of the lattice. In the case of a transverse acoustic wave the displacement is perpendicular to the propagation direction and the material is sheared.

In general shear strain pulses have a shorter wavelength and a lower sound velocity than longitudinal pulses. This makes shear strain pulses even more suitable for the investigation of nm-sized objects than longitudinal strain pulses. To generate shear strain pulses the system has to have a broken symmetry. It is not possible to excite shear strain pulses under high-symmetry conditions. There are different techniques to generate acoustic shear pulses: The use of extremely small excitations spots[115], the use of a material with an anisotropic thermal expansion[116] or the reflection of a longitudinal strain pulse at an interface with an angle relative to the strain pulse propagation direction[23]. The technique used in this work is different and relies on a modification of the technique presented in chapter 2.1.2 to allow for the excitation of shear acoustic waves[116][117]. The scheme is depicted in Figure 6.1-2 together with the experimental geometry. The general concept stays the same: An ultrafast laser pulse heats a thin, near surface region of an acoustical isotropic metal film and thereby induces a longitudinal strain pulse in the metal film. This strain pulse travels through the metal film and hits an interface between the isotropic metal film and an acoustically anisotropic substrate. At this interface a mode conversion occurs and a LA as well as a TA mode is generated upon passing of the interface. This scheme is used to excite longitudinal and transverse strain pulses and to monitor them from the side of the metal transducer[117]. To use the shear strain pulses generated in this manner, they have to be detected on the opposite side of the substrate material. The experimental setup to realize this idea is shown in Figure 6.1-2.

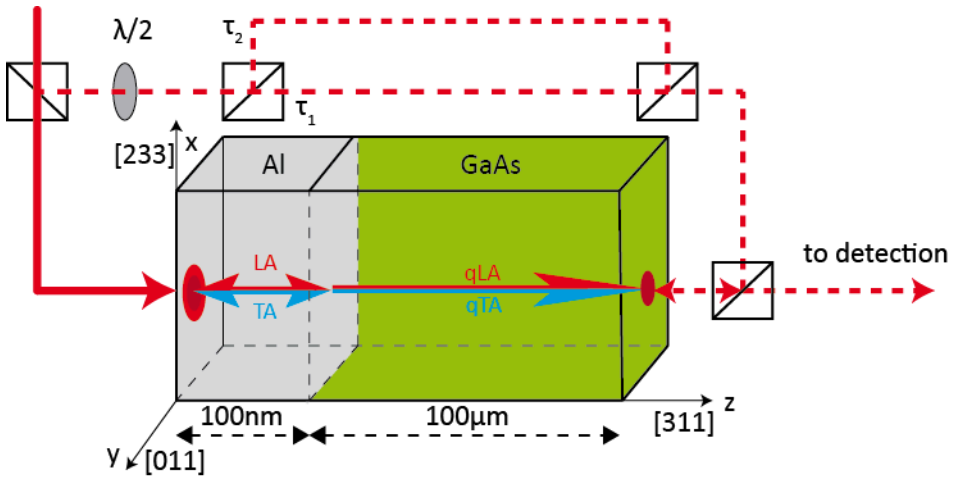

Figure 6.1-2: Illustration of the experimental setup and the sample. The pump beam passes a beam splitter and is focused on the back side of an aluminum film. The aluminum film is grown on [311]-oriented GaAs. The generated LA strain pulse reaches the interface and exhibits a mode conversion to a quasi-longitudinal (qLA) and a quasi-transverse (qTA) acoustic pulse. Both pulses travel with their specific sound velocity through the 100 µm GaAs substrate. A probe beam is split from the same laser. By using a polarization sensitive beam splitter, it is possible to select between different optical delays τ_1 and τ_2 that account for the different travel times of the qLA and qTA pulses through the GaAs substrate. The different optical path ways are combined in another beam splitter and focused onto the sample with zero incidence angle due to the use of a non-polarizing beam splitter. The reflected beam is then sent to an optical detection scheme as described in chapter 3.1. The sample is mounted in an optical bath cryostat in a He gas atmosphere at a temperature of 10 K.

An aluminum film was evaporated upon a GaAs substrate oriented along the [311]-direction. The pump beam passes a beam splitter and is focused to a round spot of 100 µm diameter (full width at half maximum) with an energy density of 4 mJ/cm^2 on the aluminum film. This generates a strain pulse in the near surface region of the aluminum that travels towards the interface. This assumption is valid, if the thermal diffusion is sub-sonical and thus the generation of the strain pulse and the traveling through the metal film can be threated independently. The strain pulse can be modelled* by the derivative of a Gaussian function (see equation (2.1.17)) and the initially generated strain pulse profile with $v_{LA,Al}$ = 6.4 km/s[119] is shown in Figure 4.3-2 b). Upon arrival of the initial purely longitudinal strain pulse at the aluminum/GaAs interface mode conversion occurs. There is no pure longitudinal mode allowed to propagate along the [311]-direction of GaAs. Instead three modes with different geometry exist: one quasi-LA (qLA), a quasi-TA (qTA) and a pure TA (pTA) mode. All of these modes are characterized by different sound velocities: v_{qTA} = 5.1 km/s, v_{qLA} = 2.9 km/s and v_{pTA} = 3.2 km/s[120]. The three possible acoustic modes have the following unit displacement vectors $\vec{e}^{qLA} = \left(u_0, 0, \sqrt{1-u_0^2}\right), \vec{e}^{qTA} = \left(\sqrt{1-u_0^2}, 0, -u_0\right), \vec{e}^{pTA} = (0,1,0)$, with u_0 = 0.165[120]. The qLA and qTA modes have a mixed character of LA and TA waves. This leads to the coupling of these

* The theoretical calculations have been performed by Tatyana Linnik and is presented in the framework of the publication found in Ref.[118].

modes to the initially longitudinal strain pulse at the interface. The pure TA mode cannot be excited in this way as there is no coupling of the pure TA wave allowed in the [311]-substrate to the pure longitudinal wave generated in the aluminum film. The shapes of the qLA and qTA strain pulses are shown in Figure 6.1-3 b) and c).

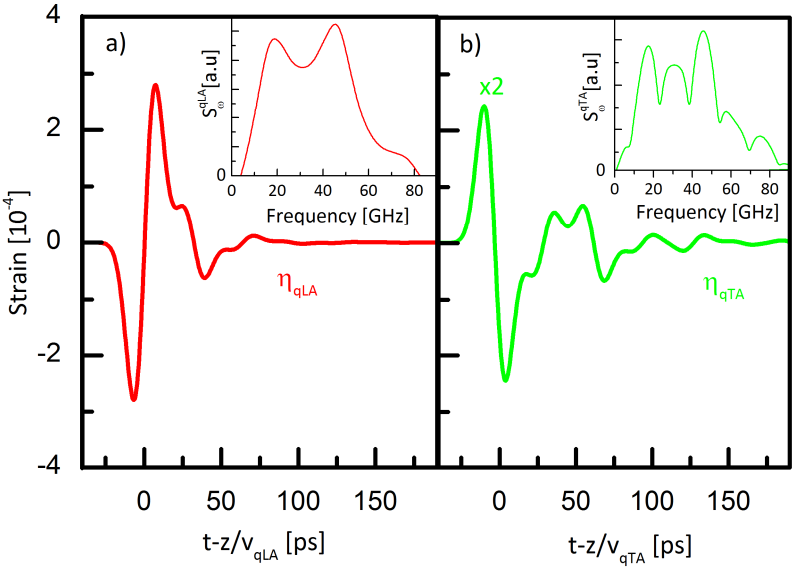

Figure 6.1-3: Calculation of a) the qLA strain pulse η_{qLA} traveling in the substrate after mode conversion at the interface for an excitation density of 4 mJ/cm^2 and b) the qTA pulse η_{qTA}. The insets of a) and b) show the acoustic spectrum of the qLA and qTA pulse, respectively.

The strain components of the transmitted pulse are related to the strain amplitude of the initial strain pulse by: $\eta_{zz}^{qLA} = 0.918\eta_0, \eta_{xz}^{qLA} = 0.077\eta_0, \eta_{zz}^{qTA} = 0.067\eta_0, \eta_{xz}^{qTA} = -0.2\eta_0$. This indicates that the qLA pulse is almost purely longitudinal, while the qTA pulse has stronger mixed character. Upon mode conversion at the interface not only strain pulses are transmitted into the substrate, but also reflected back into the aluminum film. This statement holds not only for longitudinal, but also for transversal modes. Therefore, multiple reflections inside the aluminum layer have to be taken into account to correctly predict the form of the strain pulses that travel through the substrate. These multiple reflections are the reason for the pronounced ringing for later times shown in Figure 6.1-3 b) and especially c). The amplitude of the longitudinal component of the qLA pulse is $2.8 \cdot 10^{-4}$ for a pump fluence of 4 mJ/cm^2. The qTA pulse is weak compared to the qLA pulse and its amplitude reaches only $\eta_{xz}^{qTA} = 0.6 \cdot 10^{-4}$.

Due to the different sound velocities of the qLA and qTA pulses the initially simultaneously generated pulses separate in time upon the travel through the 100 µm GaAs substrate. The pulses are detected optically by a pump-probe scheme as shown in Figure 6.1-2. To account for the different transition times of the qLA and qTA strain pulses a new approach is implemented. The time of flight for the probe beam can be adjusted by

the rotation of a half-wave plate in front of a polarization sensitive beam splitter. In this way additional delay can be included for the longer transition time of the qTA pulse. The beams are recombined in another polarization sensitive beam splitter and therefore it is possible to switch the delay without the need of readjusting the setup. For the transit of the strain pulses through the substrate no damping is expected as the sample is mounted inside a He bath cryostat at a temperature of 10 K[40]. The probe is linearly polarized and is focused to a spot of 50 µm diameter. It is incident under zero incident angle and has an energy density at least 100 times lower than the pump.

The strain pulses can be detected by the observation of changes in the reflected intensity caused by the strain pulses (see chapter 3.2). The measured trace* is shown in Figure 6.1-4. The t = 0 time is set to the generation of the strain pulses in the aluminum film. Figure 6.1-4 a) shows very pronounced Brillouin oscillations with an exponential envelope function centered around t = 19.6 ns. This time corresponds to the transition time for the qLA pulse travelling through the 100 µm [311]-GaAs substrate. The inset shows the corresponding Fourier spectrum† with a frequency of 46 GHz matching perfectly the theoretically predicted frequency of Brillouin scattering of the qLA pulse with a probe wavelength of 800 nm and a refractive index of GaAs of n = 3.6[121] at this wavelength. Figure 6.1-4 c) shows the theoretical predicted trace for the qLA strain pulse based on the solution of Maxwell's equations in the linear-strain approximation‡. The excellent agreement between theory and experimental data fortifies the conclusion that the trace in Figure 6.1-4 a) is related to the travelling qLA pulse. For the expected arrival time of the pure transverse mode, no signal is observed in the experimental data. This is expected from the symmetry considerations upon generation of the pulses explained in details above. Figure 6.1-4 b) shows Brillouin oscillations with an exponential envelope function centered around t = 34.5 ns. This time corresponds to the transition time for the qTA pulse travelling through the 100 µm GaAs substrate. Although the signal is not as perfect as in the qLA case the oscillations are clearly visible. The inset shows the corresponding Fourier spectrum with a frequency of 27 GHz matching perfectly the theoretically predicted frequency of Brillouin scattering of the qTA pulse. Figure 6.1-4 d) shows the theoretical predicted trace for the qTA strain pulse. Again the traces of the experimental and theoretical data show a very similar behavior. This leads to the conclusion that the experimental data indeed indicates the successful generation and the subsequent detection of a shear strain pulse after propagation through a substrate for the first time.

* A more broad experimental investigation of the generated qLA and qTA acoustic pulses is expected to be presented in the dissertation of J. Jäger.

† The Fourier spectrum is computed in the time interval t > 19.6 ns after the phase inversion of the strain pulse to avoid an interference effect due to the phase inversion in the Fourier spectrum.

‡ The details of the theoretical model to calculate the Brillouin signal in the pump-probe experiment can be found in Ref.[118].

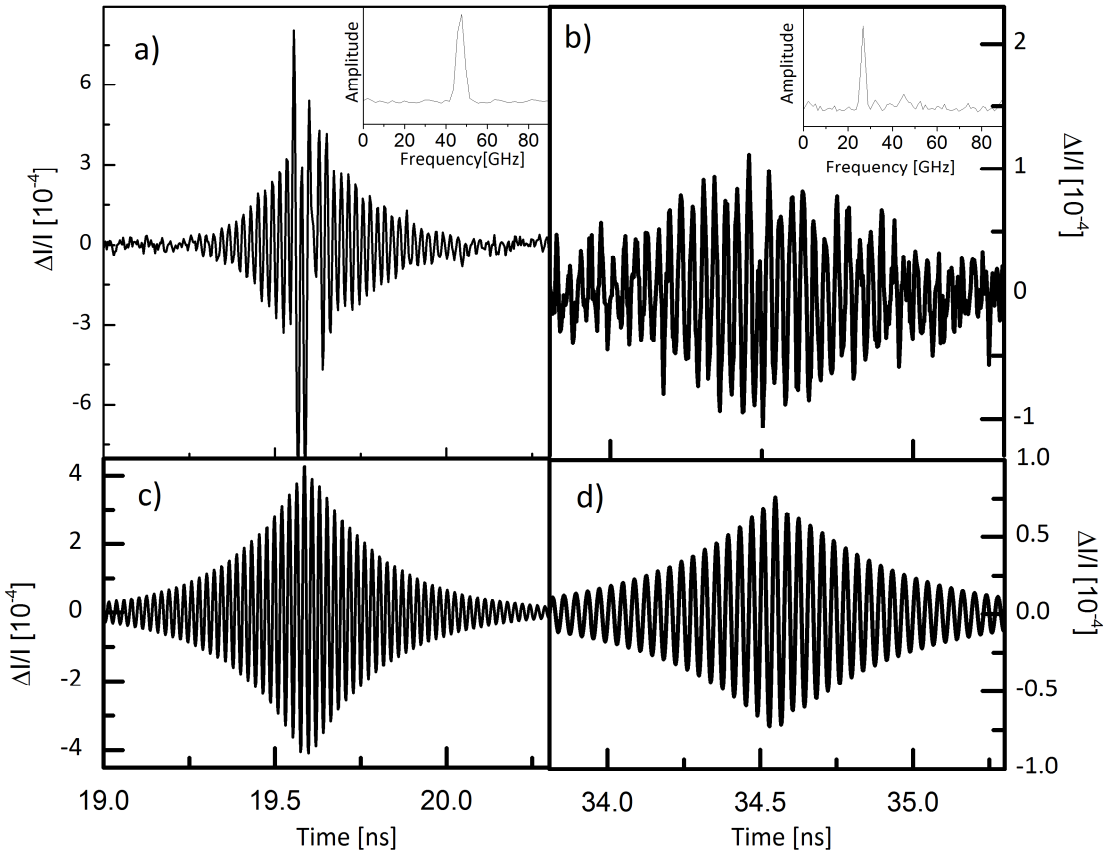

Figure 6.1-4: The change of intensity ΔI/I of the probe induced by the moving acoustic strain pulse is monitored by the pump-probe setup for a) the longitudinal strain pulse and b) the shear strain pulse. The insets in a) and b) show the Fourier spectra obtained by FFT of the time traces. The theoretically predicted traces are shown in c) for the longitudinal pulse and d) for the shear strain pulse. The t = 0 time is set to the generation of the strain pulses at the aluminum film on the side opposite of the substrate.

The method demonstrated in this section to excite shear strain pulses and the fact that they are able to pass a 100 µm GaAs substrate are used in the next section to apply these shear strain pulses to a ferromagnetic film of (Ga,Mn)As.

6.2. Efficient induction of magnetization precession by quasi-transverse acoustic pulses

This section deals with the experimental observation of the interaction of quasi-transverse acoustic waves and the magnetization of a ferromagnetic (Ga,Mn)As film grown on a [311]-oriented GaAs substrate.

The observed amplitudes of the magnetization dynamics shown in the previous chapters do not exceed 1 %. Based on the experimentally demonstrated strong influence of shear strain under static conditions[114] on the magnetization state of (Ga,Mn)As and the theoretical prediction of a stronger magneto-elastic coupling between shear strain pulses and the magnetization in (Ga,Mn)As[16], the methods to generate picosecond shear strain

pulses introduced in the last section are applied to a (Ga,Mn)As film. The experimental scheme is shown in Figure 6.2-1.

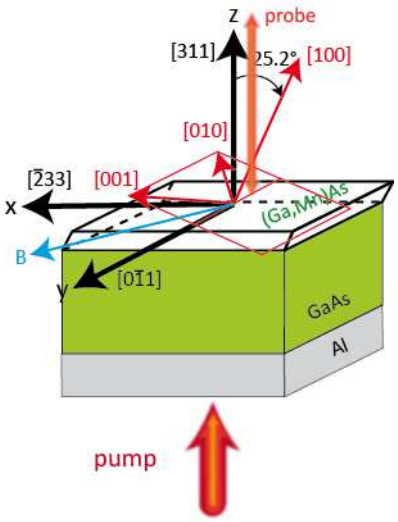

Figure 6.2-1: The experimental setup for a (Ga,Mn)As film grown on a [311]-oriented GaAs substrate. An aluminum film is deposited on the back side of the sample acting as a thermo-elastic transducer for the generation of picosecond strain pulses. The magnetic field is applied in the (311)-plane. The change of the magnetization is probed with a probe beam incident under an angle of zero degree. The sample is mounted in a He bath cryostat at a temperature of 6 K.

A (Ga,Mn)As film was grown by LT-MBE by the group of J. Furdyna from the university of Notre Dame on top of a [311]-oriented and 100 µm tick GaAs substrate. The sample has the identification number *50927 B*. Due to the lattice matched low temperature MBE growth the (Ga,Mn)As film is oriented along the [311]-crystallographic direction as well. The film has a thickness of 85 nm and a Mn content of x = 3.5 %. Due to the lattice matched growth the (Ga,Mn)As film exhibits a static strain in the order of 10^{-3}. The saturation magnetization is $\mu_0 M = 30$ mT* with a Curie Temperature of 60 K. The sample is strain free mounted in a He bath cryostat at a temperature of 6 K. The easy axis of magnetization of the sample lies along the [001]-direction, which does not lay in the layer plane, but has a small angle relative to the [$\bar{2}$33] -direction[123]. The hard axis lies along the [100]-direction which has an angle of about 25° with respect to the [311]-direction. The steady state magnetization curve is shown in Figure 6.2-2. A clear hysteresis loop is observed as the magnetic field is applied along the [311]-direction, close to the hard axis of the magnetization. The hysteresis loop does not show a rectangular shape indicating a single shift between two states of the system, but shows a figure-eight-shape. This figure-eight- shape indicates the switching of the magnetization direction to different intermediate states of the system. This observation is typical for a magnetization curve recorded with an applied field close to the hard axis of [311]-oriented (Ga,Mn)As[123]. The multi-step behavior occurs in the case of (Ga,Mn)As due to the subsequent jumping of the magnetization between different easy axes of magnetization as these easy axes are not energetically equal. This inequality arises from the application of an external field under an angle with respect to the plane spanned by the easy axes of magnetization[123].

* This value is determined by the theoretical fitting of experimental dependences[122].

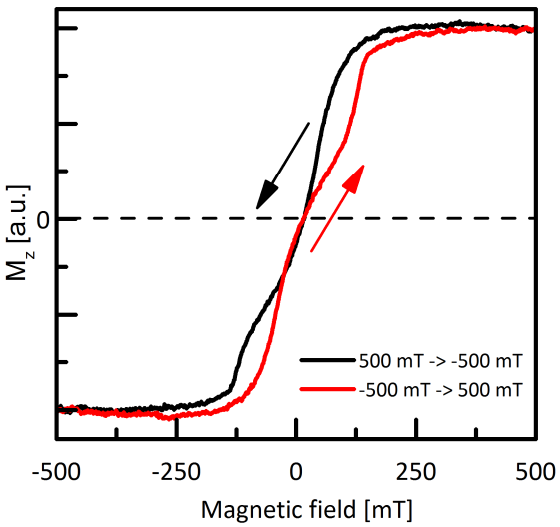

Figure 6.2-2: Steady-state magnetization curve measured in Faraday geometry. The red curve shows the field ramping from negative to positive fields and the black curve shows the other sweep direction of the magnetic field.

The pump beam generates the qTA and qLA strain pules upon mode conversion at the interface. As they travel through the substrate they segregate into separated pulses due to their different sound velocities. At the arrival they independently influence the magnetization of the (Ga,Mn)As layer. The influence of the strain pulse on the magnetization is monitored by the probe beam that is reflected under zero incidence angle from the (Ga,Mn)As layer. The different arrival times of the strain pulses is considered by two different delays of the probe beam.

Upon arrival of the qLA and qTA pulses the strain induced change in the magnetic anisotropy is expected to induce magnetization dynamics. The dynamic signals induced by the qLA and qTA pulses for an excitation density of W = 4 mJ/cm^2 and a temperature of 6 K are shown in Figure 6.2-3. The strain pulses have shapes similar to the ones shown in Figure 6.1-3. The magnetic field is applied along the $[\bar{2}33]$-direction with a strength of 500 mT. For the qLA pulse, the strain hits the magnetic layer after a transition time of t = 19.6 ns (indicated by the dashed line). Before the arrival of the strain pulse, Brillouin oscillations are clearly visible, but they are small in amplitude compared to the strong oscillations with a frequency of about 13 GHz that follow. By application of a Fourier band block filter it is possible to eliminate the Brillouin contribution from the signal (red line) to improve the clarity of the magnetization dynamics. The magnetization dynamics decay in about 400 ps.

In the case of the qTA pulse the strain hits the magnetic layer after a travel time through the GaAs substrate of a little bit less than 34.5 ns (indicated by the dashed line in Figure 6.2-3) after excitation in the aluminum film. Before the arrival of the strain pulse at the magnetic layer, Brillouin oscillations are also observed, but with much less amplitude compared to the qLA signal. This is also seen in the Fourier spectrum, where the frequency

line around 27 GHz is almost invisible. Therefore, no further signal processing is required. The high-amplitude oscillations that follow the arrival of the strain pulse have also a frequency of 13 GHz as in the case of the qLA signal. The observed signal vanishes in about 400 ps.

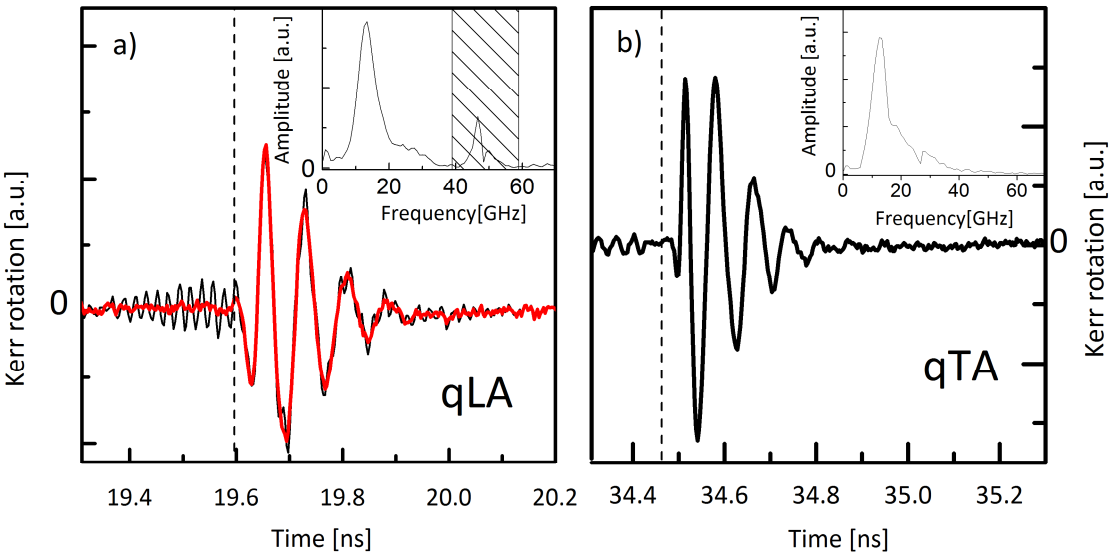

Figure 6.2-3: Dynamic Kerr rotation signal for a) the qLA strain pulse and b) the qTA strain pulse with an applied magnetic field of 500 mT and at a temperature of 6 K. The insets show the FFT spectra of the time traces. The contribution of Brillouin oscillations in the qLA signal can be filtered out by a FFT band block filter (marked area in the inset of a)) and the resulting curve is shown in red in panel a). The vertical dashed lines indicate the arrival times of the strain pulses.

In this geometry the Kerr rotation is sensitive to the z-component M_z of the overall magnetization only. When the magnetization lies inside the layer plane, the contribution from magnetic circular dichroism is weak[50]. This is realized for fields applied along the $[\bar{2}33]$-direction above 250 mT. Furthermore, by rotating the plane of the incident linear polarization of the probe beam relative to the crystallographic axes, the contribution of linear dichroism can be investigated and is found to be negligable[104]. Thus, the Kerr rotation is a direct measure of M_z. The relation of the Kerr rotation $\Delta\psi(t)$ to M_z can be described by

$$M_z = K \cdot \Delta\psi(t). \qquad (6.2.1)$$

The coefficient $K = 140\ \mathrm{rad}^{-1}$ can be determined from the measurement of the steady-state curve with an magnetic field applied along the [311]-direction as a calibration.

The magnetic field dependence of the amplitude of the induced oscillations M_z^{max} and the frequency of the oscillations is shown in Figure 6.2-4 for a weak pump fluence of $W = 3\ \mathrm{mJ/cm^2}$. The magnetic field applied is parallel to the $[\bar{2}33]$-direction.

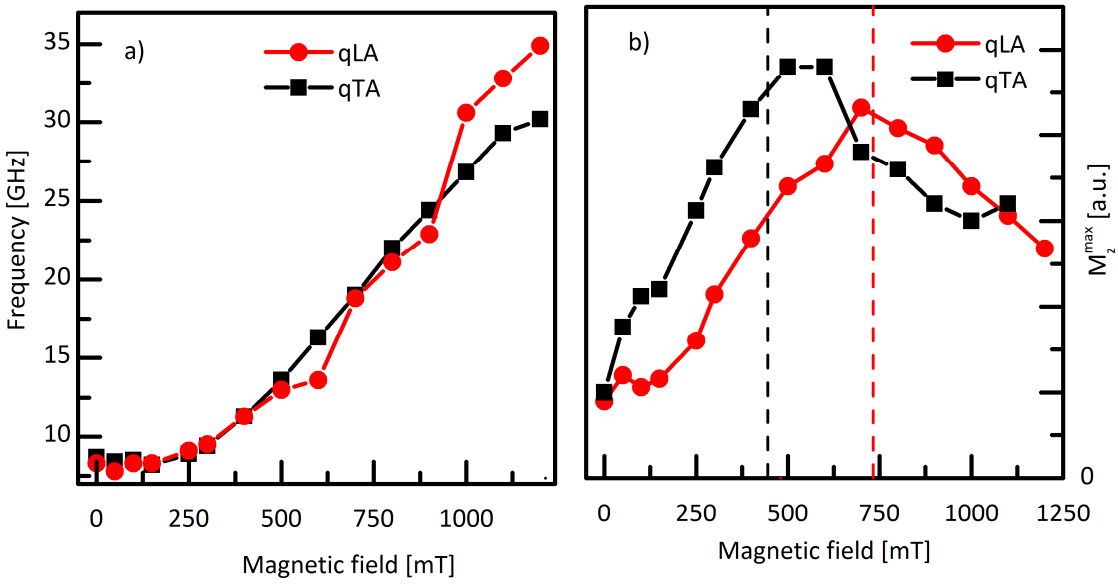

Figure 6.2-4: a) Magnetic field dependence of the amplitudes of the Kerr rotation signals induced by the qTA and qLA strain pulses. The magnetic fields at which the synchronization condition is fulfilled are indicated for the qTA (black dashed line) and the qLA (red dashed line) excitation.

The amplitude of the magnetization precession (Figure 6.2-4 a)) shows a broad maximum for both the qLA as well as the qTA case. The maximum of magnetization precession occurs at around 500 mT for the qTA case, whereas the maximum for the qLA case is centered around 750 mT.

The magnetic field dependence of the observed precession frequency (Figure 6.2-4 b)) shows a monotonous increase for increasing magnetic field. The frequency for the qLA and qTA induced oscillations are almost identical for all magnetic fields observed.

The observed strain induced magnetization precession by the shear acoustic pulse is the main experimental result of this chapter. A theoretical description is presented in the following*.

The theoretical approach is similar to the one presented in chapter 4.4. The most important differences are related to the low symmetry of the system in contrast to the high-symmetry case presented above. The important contributions to the free energy of the low-symmetry system under strain formulated in the coordinate frame, shown in Figure 6.2-1, are

* The theoretical framework has been developed by Tatyana Linnik in the context of the publication found in Ref.[122].

$$F(m_i,\eta_{ij}) = K_{c1}\left[m_x^4 + m_y^4 + m_z^4\right] + A_{2\eta}\left[\eta_{xx}m_x^2 + \eta_{yy}m_y^2 + \eta_{zz}m_z^2\right] + A_{2xy}\left[\eta_{xy}m_x m_y + \eta_{xz}m_x m_z + \eta_{yz}m_y m_z\right] + \frac{1}{2}\mu_0 M_0 m_z^2 - \left(\vec{m}\cdot\mu_0\vec{B}\right). \quad (6.2.2)$$

The first three terms are determined by the MCA with the cubic anisotropy parameter K_{c1} and the strain dependent uniaxial anisotropy parameters $A_{2\eta}$ and A_{2xy}[16]. The last two terms describe the shape anisotropy and the Zeeman energy with the magnetization projections along the crystallographic axes m_i. The anisotropy parameters can be determined by fitting the experimental data to obtain K_{c1} = -50 mT, $A_{2\eta}$ = 20 T and A_{2xy} = 100 T.

Three main factors determine the excitation of magnetization precession by picosecond strain pulses in ferromagnetic layers[16]. At first it is the spectral content of the strain pulse that needs to contain acoustic frequencies that are resonant to the magnetic modes that exist in the ferromagnetic layer. From the Fourier spectra of the qLA and qTA pulses shown in the insets of Figure 6.1-3 it is clearly seen that for both cases of qLA and qTA excitation the strain pulses contain there main spectral components between 10 GHz and 60 GHz. These are the frequencies that are relevant for the magnetic excitations as can be seen by the magnetic field dependence of the precession frequencies observed for qLA and qTA excitation in Figure 6.2-4 b).

The second factor, called the synchronization condition, involves the spatial matching of the magnetization precession and the interference of the incident part of the strain pulse traveling to the (Ga,Mn)As/He interface and the part reflected from this interface. By the knowledge of this fact, it is possible to engineer the film thickness to match the acoustic excitation to the magnetization precession. The factor is proportional to $x^{-1}\sin^2 x$ with $x = \pi f d / s_{qLA/qTA}$, where the speed of sound for the qLA and qTA case is denoted by $s_{qLA/qTA}$, the film thickness by *d* and the magnetic precession frequency by *f*. The factor has a maximum for *x = 1.16* and as the frequency is tuned by the external magnetic field the synchronization condition is fulfilled for B = 800 mT in the case of qLA excitation. For the excitation of magnetization precession by qTA phonons the maximum is at a field of B = 450 mT. This predicted behavior is in very good agreement to the experimentally observed magnetic field dependence of the magnetization precession amplitude shown in Figure 6.2-4 a).

The third factor is determined by the tilt angle of the equilibrium direction of the effective field induced by the strain pulse as described in section 4.4.

For sufficiently high magnetic fields, as is the case for an applied field of 250 mT in the experiment, the change of the effective field direction induced by the strain pulse is mainly in vertical direction* and the perturbation angle can be described by a linear combination of the strain components

(6.2.3) $$\Delta\theta = A\eta_{zz} + B\eta_{xz}\,.$$

The coefficients A and B are determined by the magnetic anisotropy and the equilibrium direction of the effective magnetic field. Typical values are a few ten radiant.

When the first two factors are close to their optimum values the third factor determines the excitation efficiency most strongly. Only in this case the maximum precession amplitude

(6.2.4) $$\Delta M_z(t) \sim M_0 \Delta\theta$$

occurs. All these factors play a major role for the trajectory of $\vec{M}(t)$ described by the Landau-Lifshitz equation. A comparison of the experimental data and the theoretical predictions is shown in Figure 6.2-5.

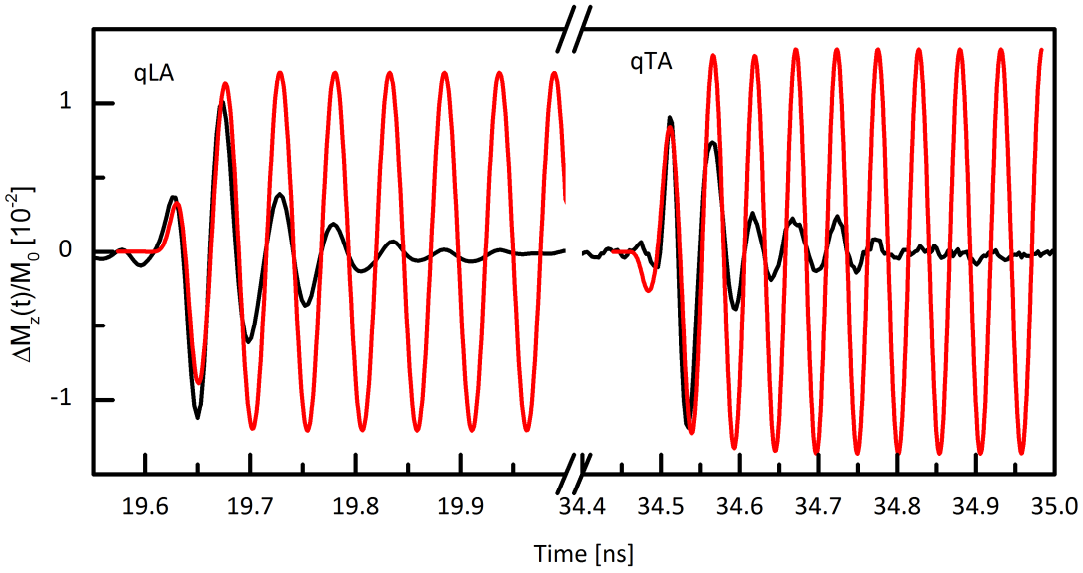

Figure 6.2-5: Strain induced magnetization precession by qTA and qLA phonons at a magnetic field of 700 mT. The measured traces (black solid lines) are compared with the theoretical model calculations (red solid lines).

* A detailed theoretical description can be found in the supplementary online material of the publication found in Ref. [122].

The numerical calculations are in perfect agreement to the observed experimental traces especially for early times and the built up process of the magnetization precession. There is no damping included in the theoretical model and therefore the amplitude of the calculated precession stays constant, whereas the experimental amplitude decays. Nevertheless, the predicted positions of the oscillations are in perfect agreement with the experimental data. As there is no damping included in the theory, the averaging of M_z over a certain time window is used to make statements regarding the amplitude of magnetization excitation to be compared to the experiments.

The observed oscillations induced by the qTA pulse for a magnetic field of 500 mT applied along the $[\bar{2}33]$-direction and along the $[0\bar{1}1]$-direction are shown in Figure 6.2-6 for a high-excitation density of W = 12 mJ/cm^2.

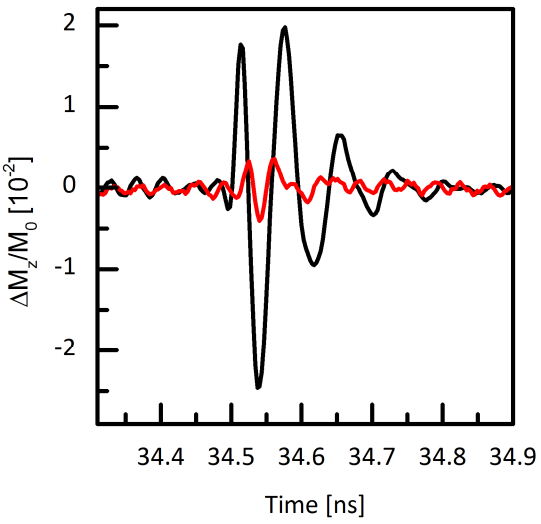

Figure 6.2-6: Comparison of the qTA induced magnetization oscillations for an external field of 500 mT applied along the $[\bar{2}33]$-direction (black curve) and along the $[0\bar{1}1]$-direction (red curve). The excitation density is W = 12 mJ/cm^2.

The difference in the observed signals for the application of the magnetic field along the two perpendicular orientated crystallographic axes is striking. The signal is maximum for the magnetic field applied along the $[\bar{2}33]$-direction and minimum along the $[0\bar{1}1]$-direction. This behavior can be explained by considering different directions of magnetic field in in the formulation of the free energy in Eqs. (6.2.2). The average magnetization precession induced by the qTA and qLA pulses, as expected from the theory for different magnetic field directions and different field strength, are shown as a color-coded contour plot in Figure 6.2-7.

A strong dependence of the precession amplitude on the direction of the magnetic field can be observed in the experiments. For a magnetic field along the $[\bar{2}33]$-direction the precession amplitude is at maximum, whereas it is minimal along the $[0\bar{1}1]$-direction. Considering the free energy in equation (6.2.2) the suppression along the $[0\bar{1}1]$-direction occurs because the free energy is not changed by the strain in this direction and therefore

the strain pulse cannot change the orientation of the effective magnetic field. There are certain directions where this situation is the same and the sensitivity of the free energy to the strain is related to the structural symmetry of the layer[16].

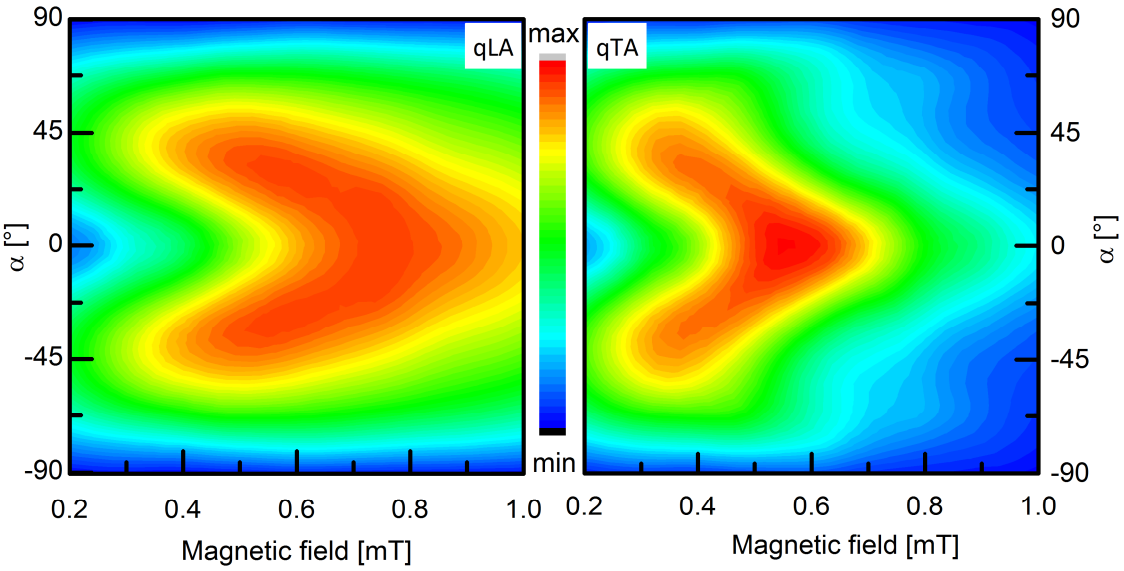

Figure 6.2-7: Color-coded contour plots for the average magnetization precession amplitude $\overline{m}_z$ for different magnetic field orientations in the layer plane with an angle α relative to the $[\overline{2}33]$-direction for the excitation by qLA and qTA strain pulses.

Up to this point, only very moderate excitation densities have been applied to the aluminum film leading to magnetization precession angles of about 1 % of the saturation magnetization M_0. As the goal is to realize magnetization switching, one has to reach for higher precession amplitudes. This can be achieved in the experimental scheme presented in this chapter by an increase of the excitation density of the pump laser to excite strain pulses with higher amplitude in the aluminum film. A pump power series for the qTA and qLA strain pulses acting on the magnetization of the layer is shown in Figure 6.2-8. It is possible to increase the excitation density up to 52 mJ/cm^2.

The qTA and qLA induced magnetization precessions for high excitation densities differ significantly from each other. In the case of the qLA induced signals the influence of the strain pulse on the magnetic layer starts about 130 ps earlier than for the lowest excitation density shown in Figure 6.2-8. The observed maximum amplitude of the magnetization precession is about 1.6 %. And it is not just the same signal like in the case of low excitation density shifted in time, but the signal is changed in shape especially for the time when the strain pulse is inside the magnetic layer. This strongly indicates a pronounced non-linear strain pulse propagation regime.

For the highest density of 52 mJ/cm^2 a huge dynamical strain of $5.2 \cdot 10^{-3}$ can be estimated based on equation (3.1.1). The excitation density applied here is tremendous

and significantly higher than typical damage thresholds observed for aluminum transducers. Nevertheless this is the actual value and the supreme performance of the aluminum films seems to be related to an optimized aluminum film deposition process[124].

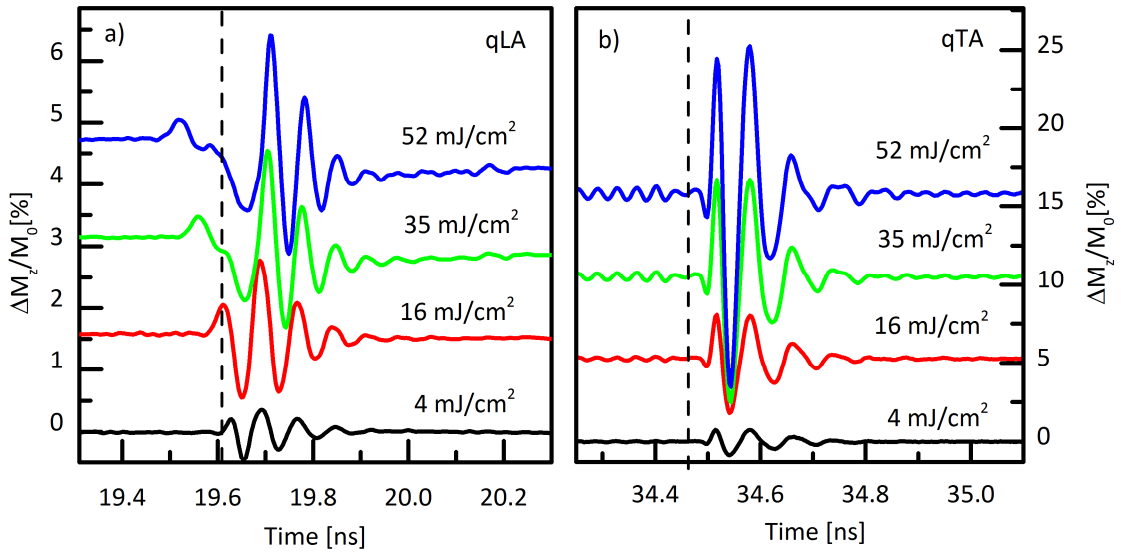

Figure 6.2-8: Waterfall plot of the pump power dependence of the strain induced magnetization precession at a magnetic field of 500 mT for the a) qLA and b) qTA strain pulses. The dashed black lines indicate the arrival time of the strain pulse at the magnetic layer for the lowest excitation density.

The early arrival of the signal indicates supersonic travel of the strain pulse indicating the formation of solitons (see chapter 2.1.3) that travel faster than the usual speed of sound. Based on the soliton speed described by equation (2.1.22) the speed up of 130 ps traversing 100 µm GaAs indicates again the huge strain applied to the magnetic layer.

The situation is particularly different for the signal induced by the qTA strain pulse. The signal starts at the same time for every excitation density and the shape is preserved. The amplitude of the magnetization precession reaches a value above 10 %. No indication of non-linear propagation is observed in the case of the qTA strain pulses. To compare the efficiency of strain induced magnetization precession between the qLA and qTA excitation, the signal at the weakest excitation density is scaled to the one with the highest excitation density by the ratio of the excitation densities. This is shown in Figure 6.2-9.

Whereas the scaled weak signal perfectly fits the observed oscillation amplitude for high excitation density in the case of the qTA strain pulse, the highest amplitude qLA pulse cannot reach the linearly scaled weak signal. This means that the induction of magnetization precession by high amplitude longitudinal strain pulses is performing sub linear. Therefore the excitation is more efficient for low excitation densities comparing the initial strain pulse amplitude and the amplitude of the magnetization precession. The

situation is different in the case of the qTA signal. The up scaled weak signal fits the high excitation density signal and therefore the excitation efficiency is not changed upon increasing the excitation density. The excitation density dependence magnetization precession amplitude is shown in Figure 6.2-10. A perfectly linear behavior is observed. Unlike the saturating behavior of the qLA pulse induced magnetization precession that saturates around 2% of the saturation magnetization, the qTA excitation can be scaled to high excitation densities without the loss of efficiency.

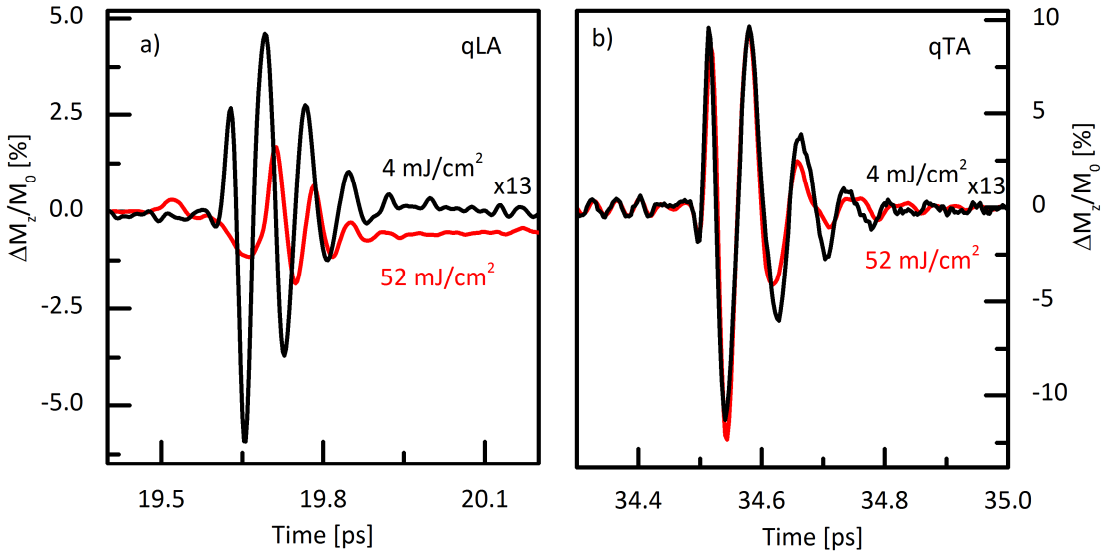

Figure 6.2-9: Scaling behavior of the magnetization precession with respect to the excitation density for the a) qLA and b) qTA signals.

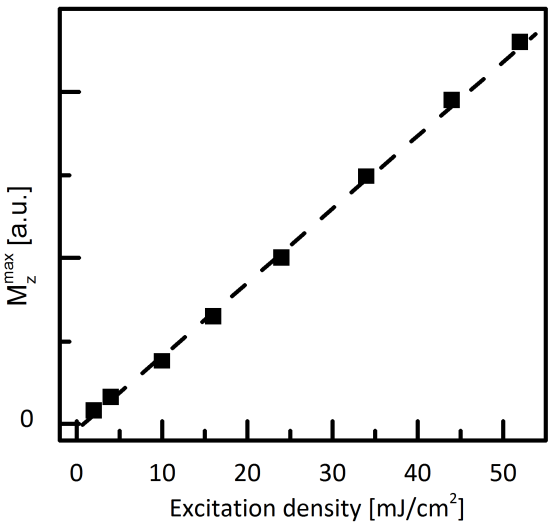

Figure 6.2-10: Excitation density dependence of the magnetization precession amplitude M_z^{max} induced by the qTA pulses.

The amplitude of the qTA induced magnetization precession is limited by the acoustic energy funneled into the qTA mode. Only about 6 % of the initially generated elastic energy goes into the qTA mode. Nevertheless the magnetization precession induced

by this relatively weak shear strain pulse is already five times higher than in the case of longitudinal excitation. This indicates the significant advantage of the use of shear strain to induce magnetization precession.

The signal observed by increasing the magnetic field up to the limit, where the effective field stays sensitive to the strain is shown in Figure 6.2-11.

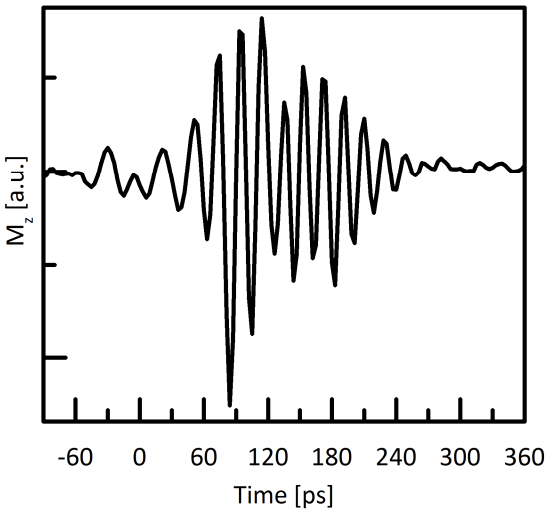

Figure 6.2-11: Magnetization precession induced by a qTA strain pulse at a magnetic field of 2000 mT. The t = 0 time is set to the time when the qTA pulse reaches the magnetic layer.

Going to this high magnetic field limit increases the precession frequency above 50 GHz. This is another remarkable feature as this precession frequency is exceeding conventional techniques like SAW[87] by one order of magnitude. Further increasing the external magnetic field above 2000 mT leads to a significantly drop of the amplitude of the signal indicating the loss of sensitivity of the effective field direction to the strain pulse.

6.3. Conclusion

In conclusion this section demonstrates the application of shear strain pulses as well as longitudinal pulses to a thin layer of the ferromagnetic semiconductor (Ga,Mn)As. The standard techniques of picosecond acoustics is modified and extended to generate not only longitudinal, but shear acoustic pulses as well as utilizing the intrinsically broken symmetry of a semiconductor grown along a high index crystallographic direction. The transition of the pulses through a substrate material under cryogenic conditions can be observed and the influence of longitudinal as well as shear strain pulses on the magnetization of a ferromagnetic layer can be monitored and significant differences are found. The longitudinal strain pulse exhibits strong perturbation due to non-linear propagation that leads to a saturation behavior regarding the magnetization precession amplitude achievable. For the shear acoustic pulse a linear dependence between the excitation density of the strain pulse and the magnetization amplitude is observed even for

the highest excitation densities. This is also in strong contrast to conventional techniques like optical induction of magnetization precession that saturate at relatively low magnetization precession amplitudes[125]. Although only 6 % of the initial elastic energy is funneled in the shear mode, a magnetization precession amplitude of more than 10 % is achieved. The only limiting factor in this experiment is the available laser power for the shear strain pulse excitation. As this is only a technical limit, the presented technique is suitable to realize conditions for magnetization switching. Furthermore precession frequencies up to 50 GHz can be achieved by the application of high magnetic fields inside the layer plane. This remarkable high frequencies exceed by far conventional techniques like the manipulation of magnetization by surface acoustic waves[87].

So the approach presented here shows the capability to realize high-amplitude magnetization precession and high precession frequencies that are needed for fast switching of magnetization, although fast magnetization switching could not be demonstrated due to technical limits that are not hard to overcome with an improved experimental setup.

7. Summary & Outlook

„Success is not final, failure is not fatal: it is the courage to continue that counts"

Winston Churchill

This work presents the successful demonstration of combining the fields of magnetic semiconductors and picosecond acoustics to a new technique for the manipulation of magnetic excitations on ultra-short time scales. The starting point is the technique of picosecond acoustics that allows generating high amplitude strain pulses with picosecond duration. The sensitivity of the ferromagnetic semiconductor on the static strain conditions has motivated the search for controlling the magnetization direction dynamically by application of picosecond strain pulses. The approach is proven to be realizable by applying magnetic fields along the hard axis of magnetization and a possible heat induced magnetization manipulation can be excluded. The whole approach relies on the strong influence of the strain pulse on the magneto-crystalline anisotropy of (Ga,Mn)As.

By applying magnetic fields close to the easy axis of magnetization high precession frequencies can be reached. Furthermore, the observed dependence of spin wave excitation efficiency on the external magnetic field allows for identifying a regime of single spin wave excitation. And even without the use of an external magnetic field strain induced magnetization precession can be observed.

Finally the extension of the standard techniques of picosecond acoustics to generate longitudinal acoustic pulses is extended to the generation of picosecond shear acoustic pulses. This is done by the use of the broken symmetry intrinsic to semiconductors grown along high-index crystallographic directions. The shear strain pulses can be separated from the longitudinal strain pulses by traversing a semiconductor substrate material at cryogenic temperatures due to the different sound velocities for shear and longitudinal acoustic waves.

Having the access to shear and longitudinal pulses generated in the same structure, it is possible to investigate the different effects on the magnetization of a (Ga,Mn)As grown on top of the high-index substrate material. While saturation behavior is observed for high-strain excitation conditions for longitudinal acoustic pulses, a perfectly linear dependence on the amplitude of the shear strain induced magnetization precession is observed. The amplitude realized with shear acoustic pulses is already five times higher than in the case

of longitudinal excitation, although the strain amplitude of the shear strain pulses is almost one order of magnitude smaller. This indicates the increase in efficiency using shear acoustic pulses. Furthermore precession frequencies up to 50 GHz can be observed for sufficiently high magnetic fields that allow for fast magnetization control. Although magnetic switching behavior cannot be observed with the experimentally used devices accessible, the realization of magnetization switching by the proposed method is only a matter of higher shear strain amplitudes and therefore higher laser intensities available. Therefore, the demonstrated method is indeed capable to realize magnetization control on ultra-short time scales.

In conclusion the technique of strain induced magnetization precession yields some bright effects that are hard or even impossible to get by standard techniques used for magnetization manipulation already. This includes a fast impact on the magnetization, no direct heating of the magnetic material, no change of optical or electrical properties due to the introduction of high carrier concentrations, there is no long aftermath of the strain pulse on the magnetic system and due to the strong spatial localization of the strain pulse very small magnetic structures can be modified. Nevertheless, there is still plenty of room for improvements.

The approach presented above is realized under cryogenic temperatures. For applications it is desirable to work at room temperature. This may either be reached by improvements of the Curie temperature of (Ga,Mn)As or by the use of a different material that has a high sensitivity to the strain conditions and a Curie temperature above room temperature.

Another point to consider is the fact that real control of the magnetization state of (Ga,Mn)As has not been demonstrated yet. One may think of using a material like Galfenol[126] or Terfenol-D with room temperature ferromagnetism and a high sensitivity to strain so that the small strains generated already are suitable for magnetization control. On the one hand, by using plasmonic structures unipolar strain pulses of huge amplitudes have been realized[127] that may be sufficient to realize magnetic switching in (Ga,Mn)As on its own. On the other hand, a model for switching between the two easy axes of magnetization has been proposed that may be realized with relatively low shear strain amplitudes[52].

8. Acknowledgement

First of all I want to thank all the people without whom this thesis would not have been possible at all.

I want to thank especially Prof. Dr. Manfred Bayer and Prof. Dr. Dmitri Yakovlev for giving me the opportunity to work in a very professional environment with high class equipment to perform all the experiments presented in this thesis. There has been outstanding administrative and technical guidance by Michaela Wäscher, Klaus Wiegers, Thomas Stöhr and Lars Wieschollek.

I thank Dr. Alexey Salasyuk, Dr. Alexey Scherbakov, Dr. Christian Brüggemann and Dr. Tillmann Godde for the great time in the lab and office, inspiring conversations and the time without physics.

I want to thank Jasmin Jäger, Anna Lusiewicz, Thomas Czerniuk, Dr. Alexey Salasyuk, Dr. Alexey Scherbakov and Dr. Jörg Debus for proof reading some chapters of this thesis.

I thank all members of E2 for the nice atmosphere, a lot of fun and a lot of soccer matches played and watched.

A special thanks to Prof. Dr. Hans-Jürgen Weber for his time for fruitful discussion about physics, politics and bicycles.

For the right balance of work and free time I want to thank all my friends and especially the members of my handball teams and the *Turbo +10 Kampfbahn* members.

Last but not least I want to thank my whole family for their support and patience.

9. Bibliography

1. Lu B, Weller D, Sunder A, Ju G, Wu X, Brockie R, u. a. *High anisotropy CoCrPt(B) media for perpendicular magnetic recording*. Journal of Applied Physics. (2003);93(10):6751–3.

2. Thompson D., Best JS. *The future of magnetic data storage techology*. IBM Journal of Research and Development. (2000);44(3):311–22.

3. Stöhr J, Siegmann HC. *Magnetism: From Fundamentals to Nanoscale Dynamics*. Springer Science & Business Media; 2007. 827 p.

4. Hancock CP, O'Grady K, El-Hilo M. *High-speed switching in particulate magnetic recording media*. J Phys D: Appl Phys. (1996);29(9):2343.

5. Thomsen C, Strait J, Vardeny Z, Maris HJ, Tauc J, Hauser JJ. *Coherent Phonon Generation and Detection by Picosecond Light Pulses*. Phys Rev Lett. (1984);53(10):989–92.

6. Muskens OL, Dijkhuis JI. *High Amplitude, Ultrashort, Longitudinal Strain Solitons in Sapphire*. Phys Rev Lett. (2002);89(28):285504.

7. Hao H-Y, Maris HJ. *Phonon dispersion and solitons in crystalline solids*. Physica B: Condensed Matter. (1999);263–264:670–3.

8. *Semiconductor Nanostructures* [Internet]. [zitiert 2. September 2014]. Verfügbar unter: http://www.springer.com/materials/nanotechnology/book/978-3-540-77898-1

9. Agostini G, Lamberti C. *Characterization of Semiconductor Heterostructures and Nanostructures*. Newnes; 2013. 829 p.

10. Awschalom DD, Flatté ME. *Challenges for semiconductor spintronics*. Nat Phys. (2007);3(3):153–9.

11. MacDonald AH, Schiffer P, Samarth N. *Ferromagnetic semiconductors: moving beyond (Ga,Mn)As*. Nat Mater. (2005);4(3):195–202.

12. Zemen J, Kučera J, Olejník K, Jungwirth T. *Magnetocrystalline anisotropies in (Ga,Mn)As: Systematic theoretical study and comparison with experiment*. Phys Rev B. (2009);80(15):155203.

13. Jr. LLB, Keizer EO. *Magnetic recording system* [Internet]. US2915594 (A), 1959 [zitiert 2. September 2014]. Verfügbar unter: http://worldwide.espacenet.com/publicationDetails/biblio;jsessionid=03E91ABE210CD345227B2E330D907BA4.espacenet_levelx_prod_0?FT=D&date=19591201&DB=&locale=en_EP&CC=US&NR=2915594A&KC=A&ND=1

14. Casiraghi A, Walker P, Akimov AV, Edmonds KW, Rushforth AW, De Ranieri E, u. a. *Fast switching of magnetization in the ferromagnetic semiconductor (Ga,Mn)(As,P) using nonequilibrium phonon pulses*. Applied Physics Letters. (2011);99(26):262503–262503 – 3.

15. Kurebayashi H, Dzyapko O, Demidov VE, Fang D, Ferguson AJ, Demokritov SO. *Controlled enhancement of spin-current emission by three-magnon splitting*. Nature Materials. (2011);10(9):660–4.

16. Linnik TL, Scherbakov AV, Yakovlev DR, Liu X, Furdyna JK, Bayer M. *Theory of magnetization precession induced by a picosecond strain pulse in ferromagnetic semiconductor (Ga,Mn)As*. Phys Rev B. (2011);84(21):214432.

17. *DIN 1320:1997-06, Norm - Beuth.de* [Internet]. [zitiert 11. August 2014]. Verfügbar unter: http://www.beuth.de/de/norm/din-1320/2964935

18. Raichel DR. *The Science and Applications of Acoustics*. Springer Science & Business Media; 2006. 664 p.

19. Vives AA. *Piezoelectric Transducers and Applications*. Springer Science & Business Media; 2008. 549 p.

20. Every AG. *Ballistic phonons and the shape of the ray surface in cubic crystals*. Phys Rev B. (1981);24(6):3456–67.

21. Hao H-Y, Maris HJ. *Experiments with acoustic solitons in crystalline solids*. Phys Rev B. (2001);64(6):064302.

22. Hao H-Y, Maris HJ. *Dispersion of the long-wavelength phonons in Ge, Si, GaAs, quartz, and sapphire*. Phys Rev B. (2001);63(22):224301.

23. Pezeril T, Ruello P, Gougeon S, Chigarev N, Mounier D, Breteau J-M, u. a. *Generation and detection of plane coherent shear picosecond acoustic pulses by lasers: Experiment and theory*. Phys Rev B. (2007);75(17):174307.

24. Perrin B, Péronne E, Belliard L. *Generation and detection of incoherent phonons in picosecond ultrasonics*. Ultrasonics. (2006);44, Supplement:e1277–81.

25. Baryshev AV, Kosobukin VA, Samusev KB, Usvyat DE, Limonov MF. *Light diffraction from opal-based photonic crystals with growth-induced disorder: Experiment and theory*. Phys Rev B. (2006);73(20):205118.

26. Kushwaha MS, Halevi P, Martínez G, Dobrzynski L, Djafari-Rouhani B. *Theory of acoustic band structure of periodic elastic composites*. Phys Rev B. (1994);49(4):2313–22.

27. Landau LD, Lifshitz EM. *Theory of Elasticity*. Elsevier; 1986. 200 p.

28. Reismann H. *Elasticity: theory and applications*. New York [u.a.]: Wiley; 1980. XIII, 425 S. : Ill., graph. Darst. p.

29. Nye JF. *Physical properties of crystals: their representation by tensors and matrices*. Clarendon Press; 1972. 354 p.

30. Haussühl S. *Kristallphysik*. Physik-Verlag; 1983. 434 p.

31. Walker PM, Kent AJ, Henini M, Glavin BA, Kochelap VA, Linnik TL. *Terahertz acoustic oscillations by stimulated phonon emission in an optically pumped superlattice*. Phys Rev B. (2009);79(24):245313.

32. Dharamsi AN, Hassam AB. *Cold shock waves in semiconductors and insulators*. Journal of Applied Physics. (1989);65(8):2998–3005.

33. Thomsen C, Grahn HT, Maris HJ, Tauc J. *Surface generation and detection of phonons by picosecond light pulses*. Phys Rev B. (1986);34(6):4129–38.

34. Kolsky H. *Stress Waves in Solids*. Courier Dover Publications; 2003. 236 p.

35. Tas G, Maris HJ. *Electron diffusion in metals studied by picosecond ultrasonics*. Phys Rev B. (1994);49(21):15046–54.

36. Fann WS, Storz R, Tom HWK, Bokor J. *Electron thermalization in gold*. Phys Rev B. (1992);46(20):13592–5.

37. Gusev VE, Wright OB. *Ultrafast nonequilibrium dynamics of electrons in metals*. Phys Rev B. (1998);57(5):2878–88.

38. Akimov AV, Scherbakov AV, Yakovlev DR, Foxon CT, Bayer M. *Ultrafast Band-Gap Shift Induced by a Strain Pulse in Semiconductor Heterostructures*. Phys Rev Lett. (2006);97(3):037401.

39. Tas G, Loomis JJ, Maris HJ, Iii AAB, Seiberling LE. *Picosecond ultrasonics study of the modification of interfacial bonding by ion implantation*. Applied Physics Letters. (1998);72(18):2235–7.

40. Chen W, Maris HJ, Wasilewski ZR, Tamura S-I. *Attenuation and velocity of 56 GHz longitudinal phonons in gallium arsenide from 50 to 300 K*. Philosophical Magazine Part B. (1994);70(3):687–98.

41. Kittel C. *Einführung in die Festkörperphysik*. Oldenbourg Verlag; 2006. 790 p.

42. Fu YB, Ogden RW. *Nonlinear Elasticity: Theory and Applications*. Cambridge University Press; 2001. 541 p.

43. Seitz F. *Solid State Physics*. Academic Press; 1970. 442 p.

44. Singhsomroje W, Maris HJ. *Generating and detecting phonon solitons in MgO using picosecond ultrasonics*. Phys Rev B. (2004);69(17):174303.

45. Akimov AV, Scherbakov AV, Capel PJS van, Dijkhuis JI, Berstermann T, Yakovlev DR, u. a. *Acoustic solitons in semiconductor nanostructures*. J Phys: Conf Ser. (2007);92(1):012002.

46. Jackiw R, Pi S-Y. *Soliton solutions to the gauged nonlinear Schrödinger equation on the plane*. Phys Rev Lett. (1990);64(25):2969–72.

47. Pelinovsky E. *Hydrodynamics of Tsunami Waves*. In: Grue J, Trulsen K, Herausgeber. Waves in Geophysical Fluids [Internet]. Springer Vienna; 2006 [zitiert 8. September 2014]. S. 1–48. Verfügbar unter: http://link.springer.com/chapter/10.1007/978-3-211-69356-8_1

48. Knox FM, Forysiak W, Doran NJ. *10-Gbt/s soliton communication systems over standard fiber at 1.55 mu;m and the use of dispersion compensation*. Journal of Lightwave Technology. (1995);13(10):1955–62.

49. Armstrong MR, Reed EJ, Kim K-Y, Glownia JH, Howard WM, Piner EL, u. a. *Observation of terahertz radiation coherently generated by acoustic waves*. Nature Physics. (2009);5(4):285–8.

50. Thevenard L, Peronne E, Gourdon C, Testelin C, Cubukcu M, Charron E, u. a. *Effect of picosecond strain pulses on thin layers of the ferromagnetic semiconductor (Ga,Mn)(As,P)*. Phys Rev B. (2010);82(10):104422.

51. Chand N. *MBE growth of high-quality GaAs*. Journal of Crystal Growth. (1989);97(2):415–29.

52. Balestriere P, Devolder T, Wunderlich J, Chappert C. *Electric field induced anisotropy modification in (Ga,Mn)As: A strategy for the precessional switching of the magnetization*. Applied Physics Letters. (2010);96(14):142504.

53. Ohno H, Chiba D, Matsukura F, Omiya T, Abe E, Dietl T, u. a. *Electric-field control of ferromagnetism*. Nature. (2000);408(6815):944–6.

54. Maekawa S. *Concepts in Spin Electronics*. OUP Oxford; 2006. 414 p.

55. *Semiconductor Science and Technology, Volume 17, Number 4, April 2002 - IOPscience* [Internet]. [zitiert 8. September 2014]. Verfügbar unter: http://iopscience.iop.org/0268-1242/17/4

56. Jonker BT, Park YD, Bennett BR, Cheong HD, Kioseoglou G, Petrou A. *Robust electrical spin injection into a semiconductor heterostructure*. Phys Rev B. (2000);62(12):8180–3.

57. Ohno H. *Making Nonmagnetic Semiconductors Ferromagnetic*. Science. (1998);281(5379):951–6.

58. Liu X, Furdyna JK. *Ferromagnetic resonance in Ga1−xMnxAs dilute magnetic semiconductors*. J Phys: Condens Matter. (2006);18(13):R245.

59. Ohno H, Munekata H, Penney T, von Molnár S, Chang LL. *Magnetotransport properties of p-type (In,Mn)As diluted magnetic III-V semiconductors*. Phys Rev Lett. (1992);68(17):2664–7.

60. Ohno H, Shen A, Matsukura F, Oiwa A, Endo A, Katsumoto S, u. a. *(Ga,Mn)As: A new diluted magnetic semiconductor based on GaAs*. Applied Physics Letters. (1996);69(3):363–5.

61. Hayashi T, Hashimoto Y, Katsumoto S, Iye Y. *Effect of low-temperature annealing on transport and magnetism of diluted magnetic semiconductor (Ga, Mn)As*. Applied Physics Letters. (2001);78(12):1691–3.

62. Ohno H. *Properties of ferromagnetic III–V semiconductors*. Journal of Magnetism and Magnetic Materials. (1999);200(1–3):110–29.

63. Zunger A, Lany S, Raebiger H. *The quest for dilute ferromagnetism in semiconductors: Guides and misguides by theory*. Physics. (2010);3:53.

64. Welp U, Vlasko-Vlasov VK, Liu X, Furdyna JK, Wojtowicz T. *Magnetic Domain Structure and Magnetic Anisotropy in Ga1-xMnxAs*. Phys Rev Lett. (2003);90(16):167206.

65. Glunk M, Daeubler J, Dreher L, Schwaiger S, Schoch W, Sauer R, u. a. *Magnetic anisotropy in (Ga,Mn)As: Influence of epitaxial strain and hole concentration*. Phys Rev B. (2009);79(19):195206.

66. Lang R, Winter A, Pascher H, Krenn H, Liu X, Furdyna JK. *Polar Kerr effect studies of Ga_{1−x}Mn_{x}As epitaxial films*. Phys Rev B. (2005);72(2):024430.

67. Mattis DC. *Theory of Magnetism Made Simple*. Hackensack, NJ: World Scientific Publishing UK; 2006. 565 p.

68. Chen L, Yan S, Xu PF, Lu J, Wang WZ, Deng JJ, u. a. *Low-temperature magnetotransport behaviors of heavily Mn-doped (Ga,Mn)As films with high ferromagnetic transition temperature*. Applied Physics Letters. (2009);95(18):182505.

69. Kuroda S, Nishizawa N, Takita K, Mitome M, Bando Y, Osuch K, u. a. *Origin and control of high-temperature ferromagnetism in semiconductors*. Nat Mater. (2007);6(6):440–6.

70. Parashar ND, Rangaraju N, Lazarov VK, Xie S, Wessels BW. *High-temperature ferromagnetism in epitaxial (In,Mn)Sb films*. Phys Rev B. (2010);81(11):115321.

71. Dietl T, Ohno H, Matsukura F. *Hole-mediated ferromagnetism in tetrahedrally coordinated semiconductors*. Phys Rev B. (2001);63(19):195205.

72. Dietl T, Ohno H, Matsukura F. *Ferromagnetic Semiconductor Heterostructures for Spintronics*. IEEE Transactions on Electron Devices. (2007);54(5):945–54.

73. Farle M. *Ferromagnetic resonance of ultrathin metallic layers*. Rep Prog Phys. (1998);61(7):755.

74. Jungwirth T, Sinova J, Mašek J, Kučera J, MacDonald AH. *Theory of ferromagnetic (III,Mn)V semiconductors*. Rev Mod Phys. (2006);78(3):809–64.

75. Landau LD, Lifšic EM. *Elektrodynamik der Kontinua*. Akademie Verlag; 1990. 588 p.

76. Spaldin NA. *Magnetic Materials: Fundamentals and Applications*. Cambridge University Press; 2010. 289 p.

77. Shono T, Hasegawa T, Fukumura T, Matsukura F, Ohno H. *Observation of magnetic domain structure in a ferromagnetic semiconductor (Ga, Mn)As with a scanning Hall probe microscope*. Applied Physics Letters. (2000);77(9):1363–5.

78. König J, Schliemann J, Jungwirth T, MacDonald AH. *Ferromagnetism in (III,Mn)V Semiconductors*. arXiv:cond-mat/0111314 [Internet]. (2001) [zitiert 8. September 2014]; Verfügbar unter: http://arxiv.org/abs/cond-mat/0111314

79. Dreher L, Donhauser D, Daeubler J, Glunk M, Rapp C, Schoch W, u. a. *Strain, magnetic anisotropy, and anisotropic magnetoresistance in (Ga,Mn)As on high-index substrates: Application to (113)A-oriented layers*. Phys Rev B. (2010);81(24):245202.

80. Scherbakov AV, van Capel PJS, Akimov AV, Dijkhuis JI, Yakovlev DR, Berstermann T, u. a. *Chirping of an Optical Transition by an Ultrafast Acoustic Soliton Train in a Semiconductor Quantum Well*. Phys Rev Lett. (2007);99(5):057402.

81. Jha AK. *A Textbook Of Applied Physics*. I. K. International Pvt Ltd; 2009. 398 p.

82. Babilotte P, Ruello P, Mounier D, Pezeril T, Vaudel G, Edely M, u. a. *Femtosecond laser generation and detection of high-frequency acoustic phonons in GaAs semiconductors*. Phys Rev B. (2010);81(24):245207.

83. Thomsen C, Grahn HT, Maris HJ, Tauc J. *Picosecond interferometric technique for study of phonons in the brillouin frequency range*. Optics Communications. (1986);60(1–2):55–8.

84. JONES RC. *A New Calculus for the Treatment of Optical Systems. VII. Properties of the N-Matrices*. J Opt Soc Am. (1948);38(8):671–83.

85. Zvezdin AK, Kotov VA. *Modern Magnetooptics and Magnetooptical Materials*. CRC Press; 2010. 414 p.

86. Oppeneer, Peter. *Lecture_Oppeneer_Schwerte.ppt - lecture_oppeneer_schwerte.pdf* [Internet]. [zitiert 29. April 2014]. Verfügbar unter: http://www.ep4.ruhr-uni-bochum.de/imperia/md/content/sfb/summerschool2007/lecture_oppeneer_schwerte.pdf

87. Davis S, Baruth A, Adenwalla S. *Magnetization dynamics triggered by surface acoustic waves*. Applied Physics Letters. (2010);97(23):232507–232507 – 3.

88. Hunklinger S. *Festkörperphysik*. Oldenbourg Verlag; 2007. 614 p.

89. Moore GP, Ferré J, Mougin A, Moreno M, Däweritz L. *Magnetic anisotropy and switching process in diluted Ga1−xMnxAs magnetic semiconductor films*. Journal of Applied Physics. (2003);94(7):4530–4.

90. Liu X, Lim WL, Titova LV, Dobrowolska M, Furdyna JK, Kutrowski M, u. a. *Perpendicular magnetization reversal, magnetic anisotropy, multistep spin switching, and domain nucleation and expansion in Ga1−xMnxAs films*. Journal of Applied Physics. (2005);98(6):063904–063904 – 11.

91. Scherbakov AV, Salasyuk AS, Akimov AV, Liu X, Bombeck M, Brüggemann C, u. a. *Coherent Magnetization Precession in Ferromagnetic (Ga,Mn)As Induced by Picosecond Acoustic Pulses*. Phys Rev Lett. (2010);105(11):117204.

92. Bihler C, Althammer M, Brandlmaier A, Geprägs S, Weiler M, Opel M, u. a. *Ga1−xMnxAs/piezoelectric actuator hybrids: A model system for magnetoelastic magnetization manipulation*. Phys Rev B. (2008);78(4):045203.

93. Liu X, Sasaki Y, Furdyna JK. *Ferromagnetic resonance in Ga_{1-x}Mn_{x}As: Effects of magnetic anisotropy*. Phys Rev B. (2003);67(20):205204.

94. Northrop GA, Hebboul SE, Wolfe JP. *Lattice dynamics from phonon imaging*. Phys Rev Lett. (1985);55(1):95–8.

95. Wolfe JP. *Imaging Phonons: Acoustic Wave Propagation in Solids*. Cambridge University Press; 2005. 431 p.

96. Kittel C. *Excitation of Spin Waves in a Ferromagnet by a Uniform rf Field*. Phys Rev. (1958);110(6):1295–7.

97. Bloch F. *Zur Theorie des Ferromagnetismus*. Z Physik. (1930);61(3-4):206–19.

98. Goennenwein STB, Graf T, Wassner T, Brandt MS, Stutzmann M, Philipp JB, u. a. *Spin wave resonance in Ga1−xMnxAs*. Applied Physics Letters. (2003);82(5):730–2.

99. VAN KRANENDONK J, VAN VLECK JH. *Spin Waves*. Rev Mod Phys. (1958);30(1):1–23.

100. Kruglyak VV, Demokritov SO, Grundler D. *Magnonics*. J Phys D: Appl Phys. (2010);43(26):264001.

101. Ph.D AGG, Melkov AGGGA. *Magnetization Oscillations and Waves*. CRC PressINC; 1996. 460 p.

102. Demokritov SO, Demidov VE, Dzyapko O, Melkov GA, Serga AA, Hillebrands B, u. a. *Bose–Einstein condensation of quasi-equilibrium magnons at room temperature under pumping*. Nature. (2006);443(7110):430–3.

103. Beschoten B, Crowell PA, Malajovich I, Awschalom DD, Matsukura F, Shen A, u. a. *Magnetic Circular Dichroism Studies of Carrier-Induced Ferromagnetism in (Ga_{1-x}Mn_{x})As*. Phys Rev Lett. (1999);83(15):3073–6.

104. Kimel AV, Astakhov GV, Kirilyuk A, Schott GM, Karczewski G, Ossau W, u. a. *Observation of Giant Magnetic Linear Dichroism in (Ga,Mn)As*. Phys Rev Lett. (2005);94(22):227203.

105. Wang DM, Ren YH, Liu X, Furdyna JK, Grimsditch M, Merlin R. *Light-induced magnetic precession in (Ga,Mn)As slabs: Hybrid standing-wave Damon-Eshbach modes*. Phys Rev B. (2007);75(23):233308.

106. Bombeck M, Salasyuk AS, Glavin BA, Scherbakov AV, Brüggemann C, Yakovlev DR, u. a. *Excitation of spin waves in ferromagnetic (Ga,Mn)As layers by picosecond strain pulses*. Phys Rev B. (2012);85(19):195324.

107. Tucker JW, Rampton VW. *Microwave Ultrasonics in Solid State Physics*. Amsterdam: Elsevier Science Publishing Co Inc.,U.S; 1972.

108. Pomerantz M. *Excitation of Spin-Wave Resonance by Microwave Phonons*. Phys Rev Lett. (1961);7(8):312–3.

109. Landau LD, Lifshitz EM, Pitaevskii LP. *Statistical Physics, Part 2 : Volume 9*. Butterworth-Heinemann; 1980. 404 p.

110. Liu X, Zhou YY, Furdyna JK. *Angular dependence of spin-wave resonances and surface spin pinning in ferromagnetic (Ga,Mn) As films*. Phys Rev B. (2007);75(19):195220.

111. Qi J, Xu Y, Tolk NH, Liu X, Furdyna JK, Perakis IE. *Coherent magnetization precession in GaMnAs induced by ultrafast optical excitation*. Applied Physics Letters. (2007);91(11):112506–112506 – 3.

112. Pascual Winter MF, Rozas G, Fainstein A, Jusserand B, Perrin B, Huynh A, u. a. *Selective Optical Generation of Coherent Acoustic Nanocavity Modes*. Phys Rev Lett. (2007);98(26):265501.

113. Beardsley RP, Akimov AV, Henini M, Kent AJ. *Coherent Terahertz Sound Amplification and Spectral Line Narrowing in a Stark Ladder Superlattice*. Phys Rev Lett. (2010);104(8):085501.

114. Rushforth AW, De Ranieri E, Zemen J, Wunderlich J, Edmonds KW, King CS, u. a. *Voltage control of magnetocrystalline anisotropy in ferromagnetic-semiconductor-piezoelectric hybrid structures*. Phys Rev B. (2008);78(8):085314.

115. Rossignol C, Rampnoux JM, Perton M, Audoin B, Dilhaire S. *Generation and Detection of Shear Acoustic Waves in Metal Submicrometric Films with Ultrashort Laser Pulses*. Phys Rev Lett. (2005);94(16):166106.

116. Matsuda O, Wright OB, Hurley DH, Gusev VE, Shimizu K. *Coherent Shear Phonon Generation and Detection with Ultrashort Optical Pulses*. Phys Rev Lett. (2004);93(9):095501.

117. Hurley DH, Wright OB, Matsuda O, Gusev VE, Kolosov OV. *Laser picosecond acoustics in isotropic and anisotropic materials*. Ultrasonics. (2000);38(1–8):470–4.

118. Scherbakov AV, Bombeck M, Jäger JV, Salasyuk AS, Linnik TL, Gusev VE, u. a. *The QLA and QTA strain Picosecond opto-acoustic interferometry and polarimetry in high-index GaAs*. Opt Express. (2013);21(14):16473–85.

119. Lide DR. *CRC Handbook of Chemistry and Physics, 85th Edition*. CRC Press; 2004. 2718 p.

120. Popovic´ ZV, Spitzer J, Ruf T, Cardona M, Nötzel R, Ploog K. *Folded acoustic phonons in GaAs/AlAs corrugated superlattices grown along the [311] direction*. Phys Rev B. (1993);48(3):1659–64.

121. Aspnes DE, Studna AA. *Dielectric functions and optical parameters of Si, Ge, GaP, GaAs, GaSb, InP, InAs, and InSb from 1.5 to 6.0 eV*. Phys Rev B. (1983);27(2):985–1009.

122. Bombeck M, Jäger JV, Scherbakov AV, Linnik T, Yakovlev DR, Liu X, u. a. *Magnetization precession induced by quasitransverse picosecond strain pulses in (311) ferromagnetic (Ga,Mn)As*. Phys Rev B. (2013);87(6):060302.

123. Liu X, Furdyna JK, Dobrowolska M, Lim WL, Xie C, Cho YJ. *Unique properties of magnetotransport in GaMnAs films grown on vicinal and high-index planes*. Journal of Physics: Condensed Matter. (2007);19(16):165205.

124. Berstermann T, Brüggemann C, Akimov AV, Bombeck M, Yakovlev DR, Gippius NA, u. a. *Destruction and recurrence of excitons by acoustic shock waves on picosecond time scales*. Phys Rev B. (2012);86(19):195306.

125. Hashimoto Y, Kobayashi S, Munekata H. *Photoinduced Precession of Magnetization in Ferromagnetic (Ga,Mn)As*. Phys Rev Lett. (2008);100(6):067202.

126. Jäger JV, Scherbakov AV, Linnik TL, Yakovlev DR, Wang M, Wadley P, u. a. *Picosecond inverse magnetostriction in galfenol thin films*. Applied Physics Letters. (2013);103(3):032409.

127. Temnov VV, Klieber C, Nelson KA, Thomay T, Knittel V, Leitenstorfer A, u. a. *Femtosecond nonlinear ultrasonics in gold probed with ultrashort surface plasmons*. Nat Commun. (2013);4:1468.

10. Publication list

P1: Scherbakov AV, Salasyuk AS, Akimov AV, Liu X, **Bombeck M**, Brüggemann C, u. a. *Coherent Magnetization Precession in Ferromagnetic (Ga,Mn)As Induced by Picosecond Acoustic Pulses*. Phys Rev Lett. (2010);105(11):117204.

P2: Berstermann T, Brüggemann C, **Bombeck M**, Akimov AV, Yakovlev DR, Kruse C, u. a. *Optical bandpass switching by modulating a microcavity using ultrafast acoustics*. Phys Rev B. (2010);81(8):085316.

P3: Salasyuk AS, Scherbakov AV, Yakovlev DR, Akimov AV, Kaplyanskii AA, **Bombeck M**, u. a. *Filtering of Elastic Waves by Opal-Based Hypersonic Crystal*. Nano Lett. (2010);10(4):1319–23.

P4: Pawlis A, Berstermann T, Brüggemann C**, Bombeck M**, Dunker D, Yakovlev DR, u. a. *Exciton states in shallow ZnSe/(Zn,Mg)Se quantum wells: Interaction of confined and continuum electron and hole states*. Phys Rev B. (2011);83(11):115302.

P5: Salasyuk, A.S., Yakovlev, D.R., Akimov, A.V., Kaplyanskii, A.A., Kaplan, S.F., **Bombeck, M**., u. a. *Long-living GHz Vibrations in Opal-based Hypersonic Crystals*. Chinese Journal of Physics. (2011) 49:56–62.

P6: Brüggemann C, Akimov AV, Scherbakov AV, **Bombeck M**, Schneider C, Höfling S, u. a. *Laser mode feeding by shaking quantum dots in a planar microcavity*. Nat Photon. (2012);6(1):30–4.

P7: **Bombeck M**, Salasyuk AS, Glavin BA, Scherbakov AV, Brüggemann C, Yakovlev DR, u. a. *Excitation of spin waves in ferromagnetic (Ga,Mn)As layers by picosecond strain pulses*. Phys Rev B. (2012);85(19):195324.

P8: Berstermann T, Brüggemann C, Akimov AV, **Bombeck M**, Yakovlev DR, Gippius NA, u. a. *Destruction and recurrence of excitons by acoustic shock waves on picosecond time scales*. Phys Rev B. (2012);86(19):195306.

P9: Akimov IA, Belotelov VI, Scherbakov AV, Pohl M, Kalish AN, **Bombeck M**, u. a. *Hybrid structures of magnetic semiconductors and plasmonic crystals: a novel concept for magneto-optical devices [Invited]*. J Opt Soc Am B. (2012);29(2):A103–18.

P10: Scherbakov AV, **Bombeck M**, Jäger JV, Salasyuk AS, Linnik TL, Gusev VE, u. a. *The QLA and QTA strain Picosecond opto-acoustic interferometry and polarimetry in high-index GaAs*. Opt Express. (2013);21(14):16473–85.

P11: **Bombeck M**, Jäger JV, Scherbakov AV, Linnik T, Yakovlev DR, Liu X, u. a. *Magnetization precession induced by quasitransverse picosecond strain pulses in (311) ferromagnetic (Ga,Mn)As*. Phys Rev B. (2013);87(6):060302.

P12: Rice WD, Ambwani P, **Bombeck M**, Thompson JD, Haugstad G, Leighton C, u. a. *Persistent optically induced magnetism in oxygen-deficient strontium titanate*. Nat Mater. (2014);13(5):481–7.

P13: Tiemeyer S, **Bombeck M**, Paulus M, Sternemann C, Nase J, Göhring H, Wirkert FJ, Möller J, Büning T, Seeck TH, Reuter D, Wieck AD, Bayer M, and Tolan M *Polaron-induced lattice distortion of (In,Ga)As quantum dots by optically excited carriers.* arXiv:14067676 [cond-mat] [Internet]. (2014) [cited 27. Oktober 2014]; available at: http://arxiv.org/abs/1406.7676